The University of Adelaide

School of Chemical Engineering

Cooperative Research Centre for Clean Power from Lignite

Physical Modelling of Mixing Between Rectangular Jets Present in Tangentially Fired Brown Coal Boilers

Ph.D. Thesis

Alessio Angelo Scarsella

Chapter 6

6 Transverse Imaging of Multiple Rectangular Jets

6.1 Introduction

The low aspect ratio of the primary jet (AR=1.2) implies that it has similarities to a square jet. As described in Section 2.4.3 the main transient structure is a vortex ring, which initially fits the general contour of a square or rectangular profile before being contorted further downstream.

Upon exiting a square nozzle, the high curvature of the velocity exit profile in proximity to the corners causes the corners of the ring to move ahead of the rest of the ring, slightly angling corners of the ring towards the jets axis as illustrated in Figure 6.1. Further downstream the ring recovers shape and switches axis by 45 degrees (Husain, 1988). The rolling of the vortex rings and subsequent deformation causes braid vortices to form between the rings, as can be seen in Figure 6.1. These braids curve outwards into the shear layer of the jet and their counter rotating motion causes smaller ‘rib’ vortices to form. The work of Grinstein (1993) reported that similar structures dominate the flow in a rectangular jet with an aspect ratio of 2:1. The main difference being that the minor axis side of the rings move ahead of those on the major axis side. This implies that there is a faster growth on the side of the minor axis. As the vortex ring progresses downstream, the braid vortices curl around the vortex ring’s corners, causing further distortion. The ring’s corners move into the shear layer where smaller ‘break-away’ eddies are formed, engulfing the surrounding fluid and entraining it back into the bulk fluid flow.

Hart (2001) used large eddy simulation to predict velocities and visualise coherent structures in a similar rectangular jet configuration to Figure 3.4 with a full secondary jet and of a one-half primary jet (this was done to reduce convergence times) operating at λ=1. He found that, although the primary jet is of an aspect ratio close that of a square jet (AR =1.2) the braids on the side of the major axis appear to be longer than those on the side of the minor axis. Hart’s observations of the secondary jet revealed that an increase in aspect ratio to 2.2 caused the sides of the vortex ring parallel to the minor axis to be dragged ahead of the sides parallel to the major axis.

The nature of the vortex rings in the secondary jet caused the braids adjacent to the corners of the ring on the minor axis side to be drawn into other structures, implying that only four braids exist rather than the eight observed for the primary jet, and thus retarding the point at which axis switching occurs.

The 'rings' are the largest structures in rectangular, square and elliptical jets (Gutmark and Grinstein, 1999) and have the greatest role in transporting momentum (Hart, 2001). When two rectangular jets are located in close proximity to one another, the rings tend to merge to eventually form a single entity. This phenomenon was observed by Nathan *et al*., (2006) who observed that an oscillating forced refinery flare issuing from a pipe perturbed by an array of fuel distribution spokes had a single dominant coherent motion. According to Hart (2001) the two rings came into contact, the sub-atmospheric region between them caused both rings to lag in development. The primary jet's larger cross section implies that the primary vortex ring has greater momentum than the secondary, causing the latter to disintegrate (based on the assumption that the velocities are equal).

To understand the mechanisms at play between multiple rectangular jets, an in-depth quantitative analysis of the transverse motions of the jet structure was performed which includes quantitative time-averaged information. The temporal resolution is insufficient to resolve the full instantaneous concentration. The transverse analysis facilitates three dimensional modelling of the jet mixture fraction as a function of velocity ratio. From the qualitative analysis in Chapter 4 it is apparent that a transition region in the primary jet occurs at $2<x/D<4$, and that the extent of this region increases with the velocity ratio. A transverse flow analysis was undertaken to deliver more insight into the physical mechanisms at play.

NOTE: This figure is included on page 166 of the print copy of the thesis held in the University of Adelaide Library.

Figure 6.1: Vortices formed in free rectangular pipe jet (Gutmark and Grinstein, 1999).

6.2 Experimental Design and Conditions

The experimental equipment, procedures and methods are described in Chapters 3 and 5. For the transverse imaging, the, laser sheet was orientated perpendicular to the flow. Either the primary or secondary jets were seeded with sodium fluorescein. The secondary to primary jet velocity ratios to be investigated were λ = 0, 0.55, 1.4, 2.8, 3.6 and ∞, and the axial stations to be imaged were *x/D* = 0.1, 0.2, 0.5, 1, 2, 4, 6 and 8. Table 6.1 presents the calculated secondary to primary jet momentum and momentum flux ratios for the experimental conditions with the corresponding velocity ratios.

Re, Secondary	**velocity ratio, λ**	**momentum flux ratio, γ**	**momentum ratio, κ**
	0	0	0
3,720	0.55	0.3	0.18
9,712	1.4	1.96	1.18
19,430	2.8	7.84	4.7
24,928	3.6	12.96	7.78
10,000	∞	∞	∞

Table 6.1: Secondary to primary jet momentum flux and momentum ratios with corresponding velocity ratio to be investigated with the transverse imaging.

6.3 Quantitative Analysis

6.3.1 Primary Jet

6.3.1.1 Planar Data

Figures 6.2 to 6.9 plots the time-averaged normalised concentration of the primary jet at the axial stations *x/D* =0.1, 0.2, 0.5, 1, 2, 4, 6 and 8 for λ=0, 0.55, 1.4, 2.8 and 3.6. At *x/D*=0.1 an increase in the velocity ratio causes the distortion of the jet in the corners, with the presence of small secondary structures. These structures increase in size with higher velocity ratios in Figure 6.2 and shown schematically in Figure 6.12. The presence of the corner structure visibly alters the shape of the primary jet structure as the velocity ratio is increased from 0.55 to 3.6 at axial stations of *x/D* =0.2, 0.5 and 1 (Figures 6.3, 6.4 and 6.5 respectively).

Studies on the vortex dynamics of square jets by Grinstein *et al*., (1995) and rectangular jets by Grinstein (2001) and Miller *et al*., (1995) illustrate by means of vorticity that counter rotating vortices or 'braids' exist at each corner of a square-rectangular jet. Vorticity is either a vectorial or scalar quantity of the measure of velocity gradient, which is the driving force of vortices. For a three dimensional system the vorticity vector and magnitude is defined as;

$$\Omega = \left(\frac{\partial u}{\partial y} - \frac{\partial v}{\partial z}\right) i + \left(\frac{\partial u}{\partial z} - \frac{\partial w}{\partial x}\right) j + \left(\frac{\partial v}{\partial x} - \frac{\partial u}{\partial y}\right) k$$

Equation 6.1

where *u*, *v* and *w* are the *x*, *y* and *z* directional components of velocity and, *i, j* and *k* are the normal tensors in the *x*, *y* and *z* directions. The magnitude of the vorticity is then defined as;

$$|\Omega| = \sqrt{\left(\frac{\partial u}{\partial y} - \frac{\partial v}{\partial z}\right)^2 + \left(\frac{\partial u}{\partial z} - \frac{\partial w}{\partial x}\right)^2 + \left(\frac{\partial v}{\partial x} - \frac{\partial u}{\partial y}\right)^2}$$

Equation 6.2

The actual driving force in vortex formation is the difference in velocity gradient, i.e. $\frac{\partial u}{\partial y} - \frac{\partial v}{\partial z}$ and $\frac{\partial u}{\partial z} - \frac{\partial w}{\partial x}$. Figures 6.10 and 6.11 are diagrams of the transverse velocity gradients of the primary jet at λ=0 and the primary and secondary jet at λ>0. Regardless of the velocity ratio the presence of the secondary jet will affect the velocity gradients of the primary jet. However, it is the velocity ratio that is responsible for the degree of change. A plausible mechanism for the change in shape of the primary jet with an increase in velocity ratio is that the velocity gradient is altered to a point where it is affecting the nature of the counter rotating vortices. In Figure 6.12 (*x/D* =0.1) an increase in velocity ratio causes each vortex adjacent to the sides of the major axis to possibly increase in size and strength, thus deforming the time-averaged structure of the primary jet fluid in the corners. The schematic diagrams in Figures 6.13 and 6.14, at *x/D* =0.5 and 1 show that the vortices adjacent to the major axis side of the primary jet have increased in size, and consequently in strength, with an increase in λ, thus causing the primary jet to significantly deform in shape leading to the situation in Figure 6.15, where the primary jet at *x/D*=2 and λ=2.8-3.6 no longer resembles the original rectangular form which is still preserved at λ=0 at this axial position.

This "phenomenon" of the corner vortices of the primary jet altering the flow with downstream distance plays an important role at λ=2.8 and 3.6 and has only mild effects at λ=0.55 and 1.4. The contractions of the primary jet observed in Section 4.4.3 through Plane A and C between 1<*x/D*< 6 (λ =2.8 and 3.6) are a direct result of this.

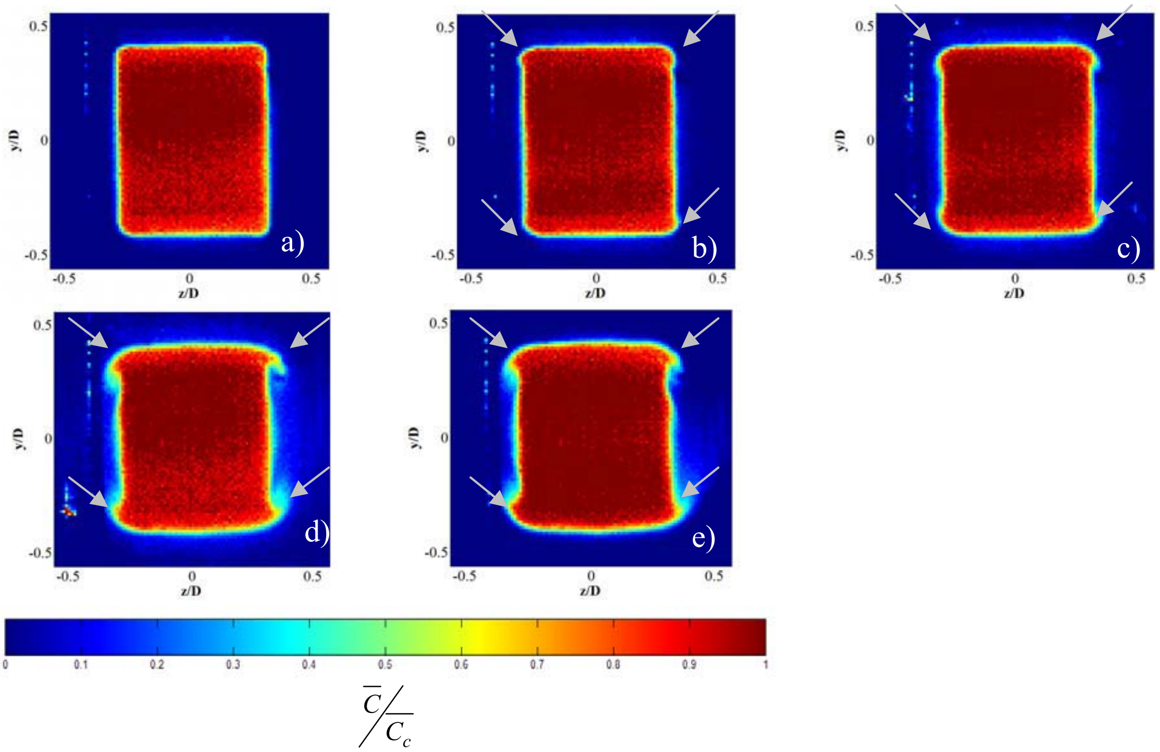

Figure 6.2: Time averaged normalised concentration of the primary jet at *x/D* =0.1, for a) λ=0, b) λ=0.55, c) λ=1.4, d) λ=2.8, e) λ=3.6. The white arrows highlight the coherent vortices on corners of the primary jet.

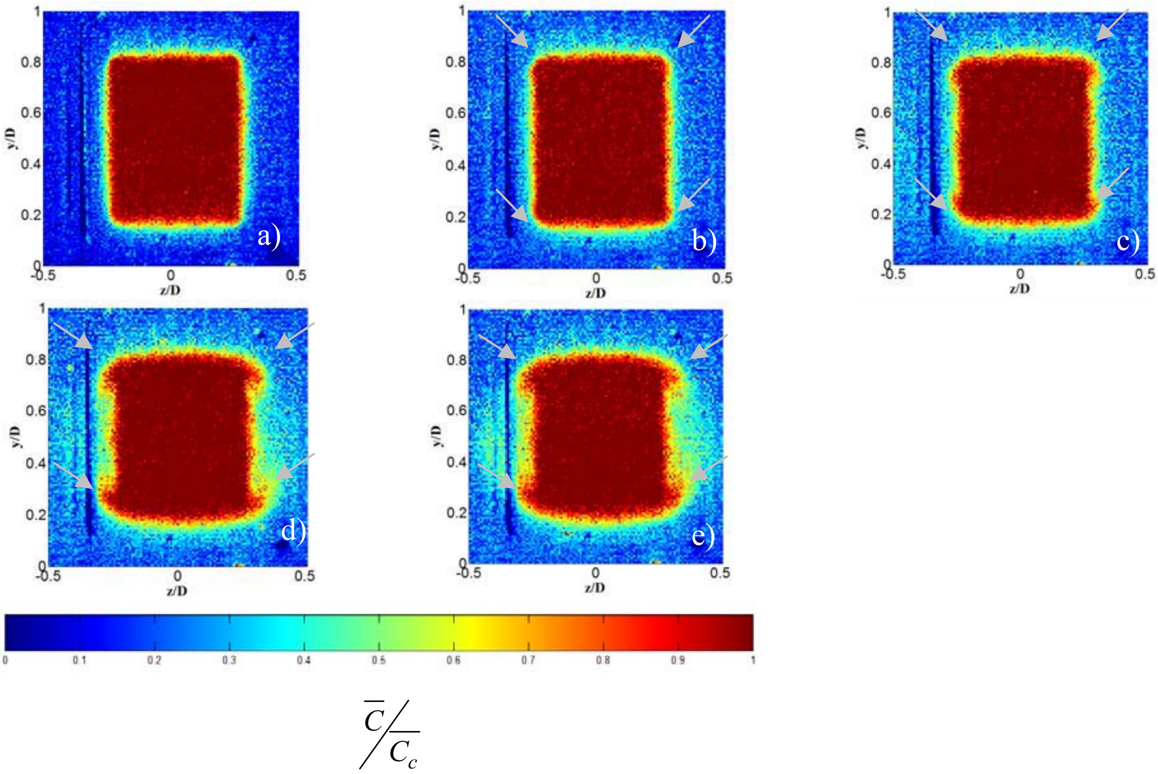

Figure 6.3: Time averaged normalised concentration of the primary jet at *x/D* =0.2, for a) λ=0, b) λ=0.55, c) λ=1.4, d) λ=2.8, e) λ=3.6. The white arrows highlight the change in jet structure at the corners of the primary jet.

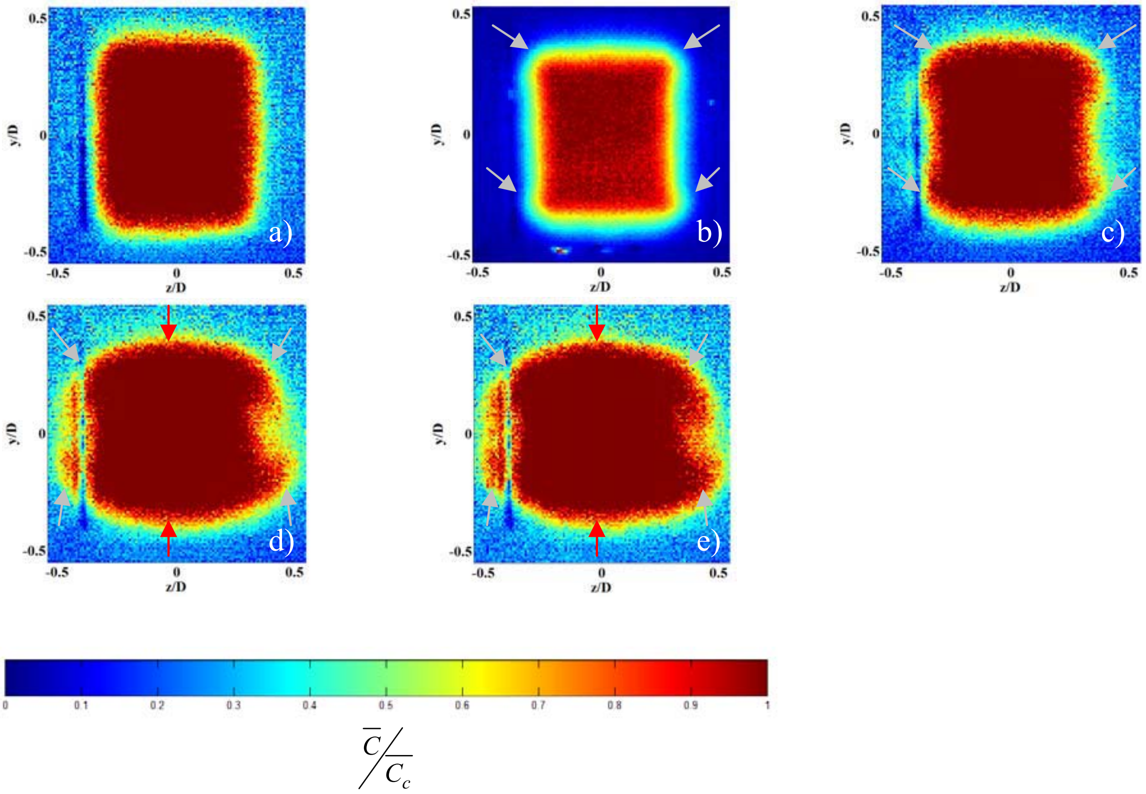

Figure 6.4: Time averaged normalised concentration of the primary jet at *x/D* =0.5, for a) λ=0, b) λ=0.55, c) λ=1.4, d) λ=2.8, e) λ=3.6. The white arrows highlight the change in jet structure vortices at the corners of the primary jet. The red arrows outline the shortening of the primary jet in the *y*-direction.

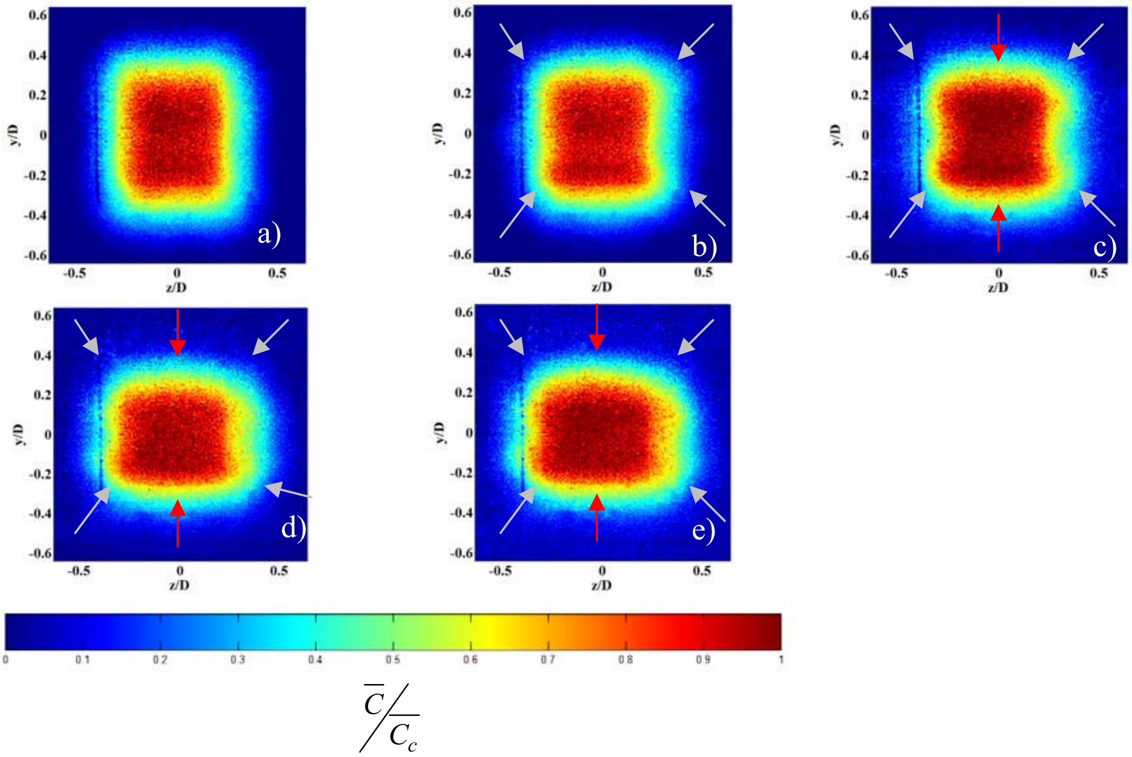

Figure 6.5: Time averaged normalised concentration of the primary jet at *x/D* =1, for a) λ=0, b) λ=0.55, c) λ=1.4, d) λ=2.8, e) λ=3.6. The white arrows highlight the change in jet structure at the corners of the primary jet. The red arrows outline the contraction of the primary jet in the *y*-direction.

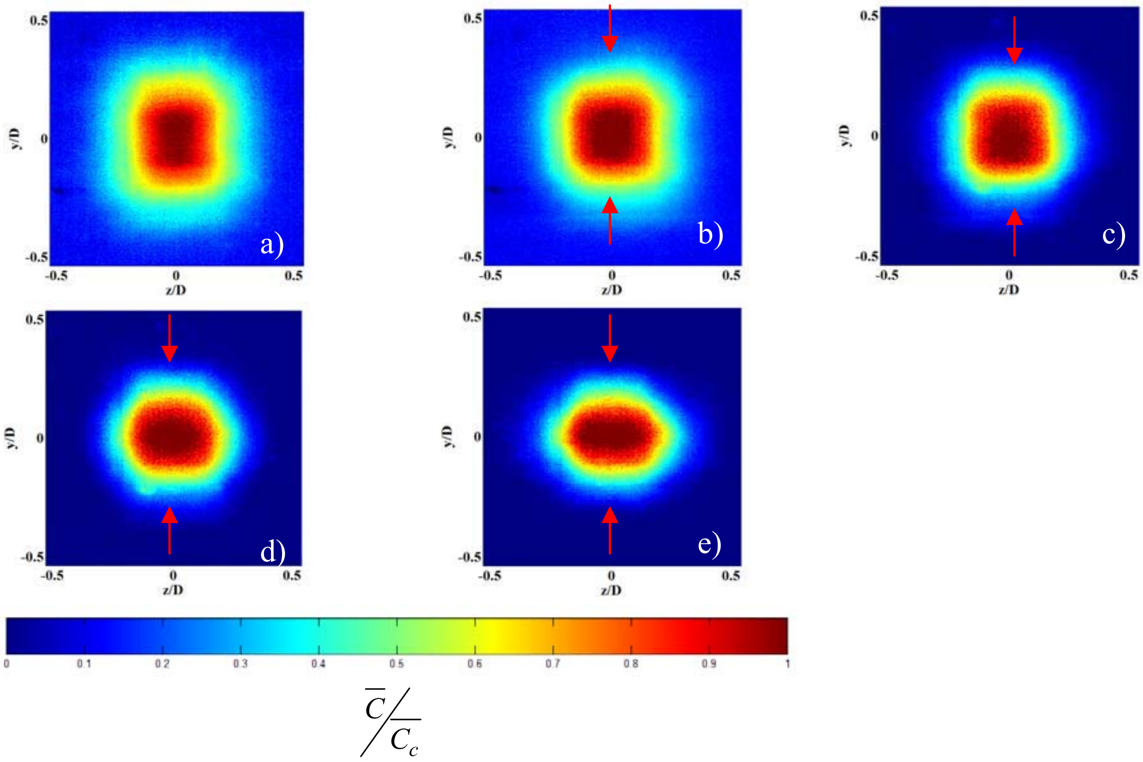

Figure 6.6: Time averaged normalised concentration of the primary jet at *x/D* =2, for a) λ=0, b) λ=0.55, c) λ=1.4, d) λ=2.8, e) λ=3.6. The red arrows outline the contraction of the primary jet in the *y*-direction.

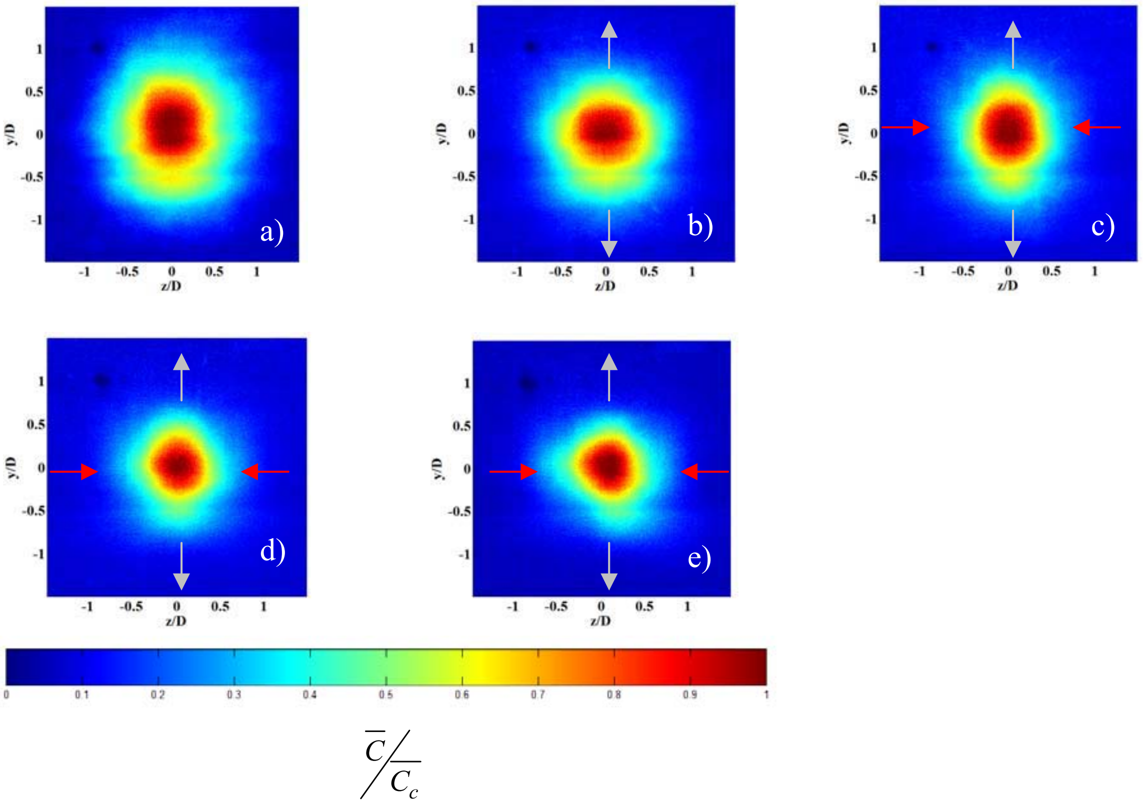

Figure 6.7: Time averaged normalised concentration of the primary jet at *x/D* =4, for a) λ=0, b) λ=0.55, c) λ=1.4, d) λ=2.8, e) λ=3.6. The white arrows highlight the expansion with respect to *x/D* =2 (Figure 6.6) in the *y*-direction, the red arrows outline the contraction of the primary jet in the *z*-direction.

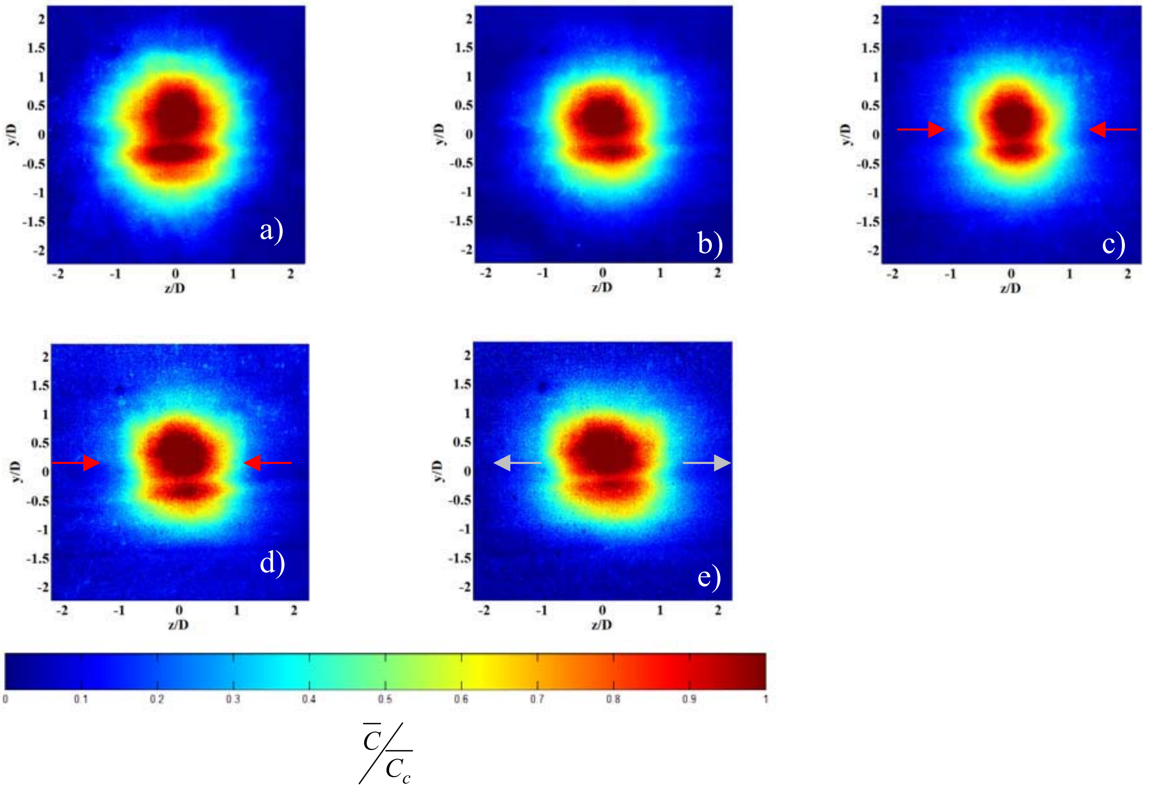

Figure 6.8: Time averaged normalised concentration of the primary jet at x/D =6, for a) λ=0, b) λ=0.55, c) λ=1.4, d) λ=2.8, e) λ=3.6. The red arrows outline the contraction of the primary jet in the y-direction. The white arrows highlight the progressive expansion of the primary jet in the z-direction with respect to x/D =4, λ=3.6 (Figure 6.7 e).

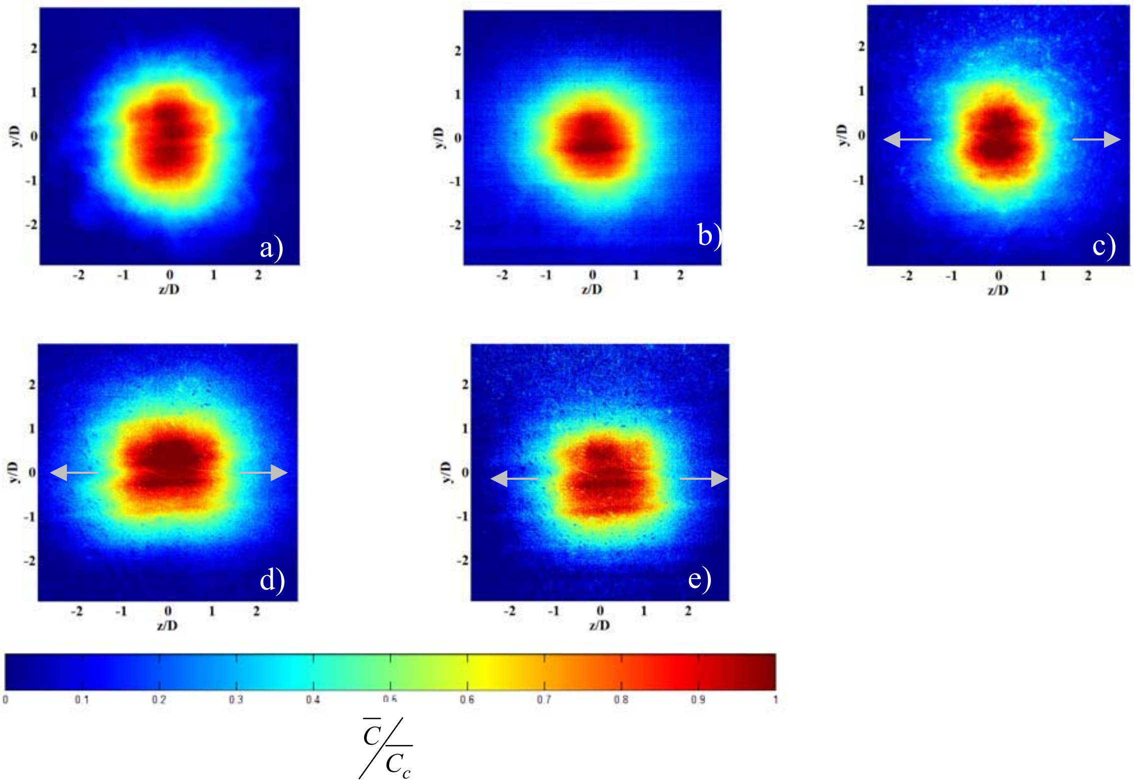

Figure 6.9: Time averaged normalised concentration of the primary jet at x/D =8, for a) λ=0, b) λ=0.55, c) λ=1.4, d) λ=2.8, e) λ=3.6. The white arrows highlight the progressive expansion of the primary jet in the z-direction with respect to x/D =4, λ=1.4, 2.8 and 3.6 (Figures 6.7 c, d and e).

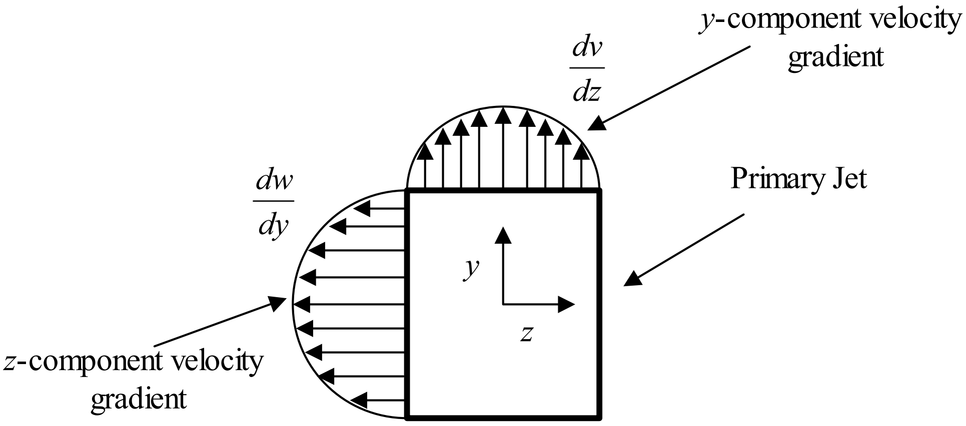

Figure 6.10: y and z-direction velocity gradients of the primary jet alone

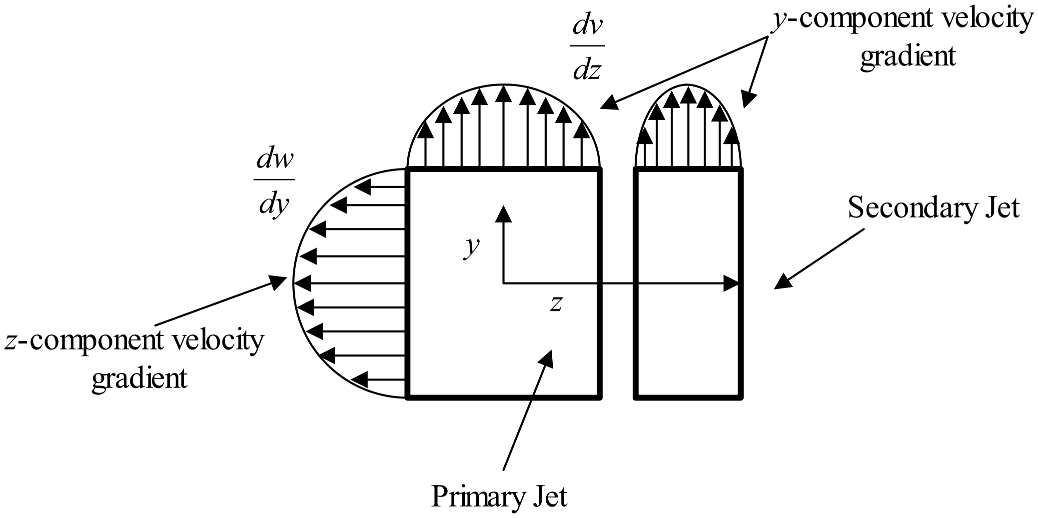

Figure 6.11: y and z-direction velocity gradients of the primary and secondary jets.

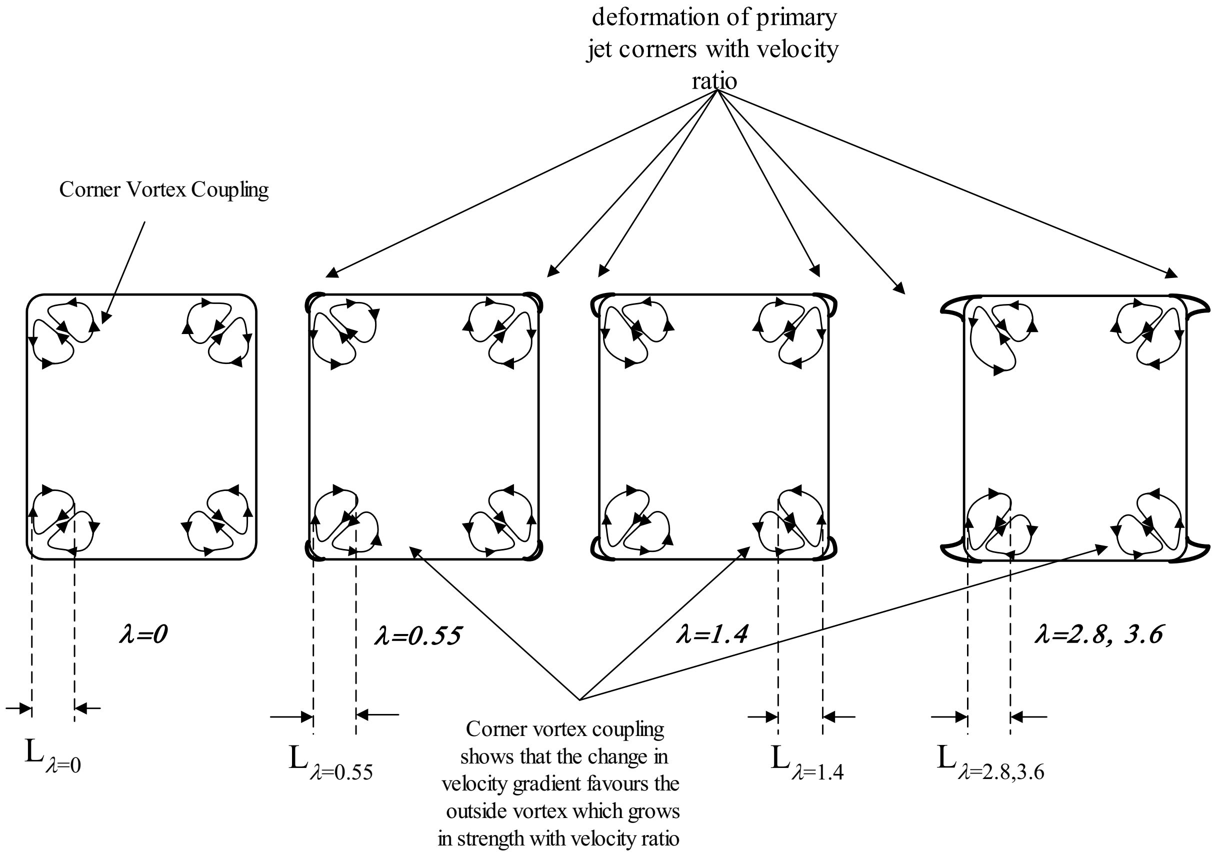

Figure 6.12: Sketch of the progressive formation of the coherent corner vortices on the primary jet for λ=0, 0.55, 1.4, 2.8 and 3.6, x/D=0.1.

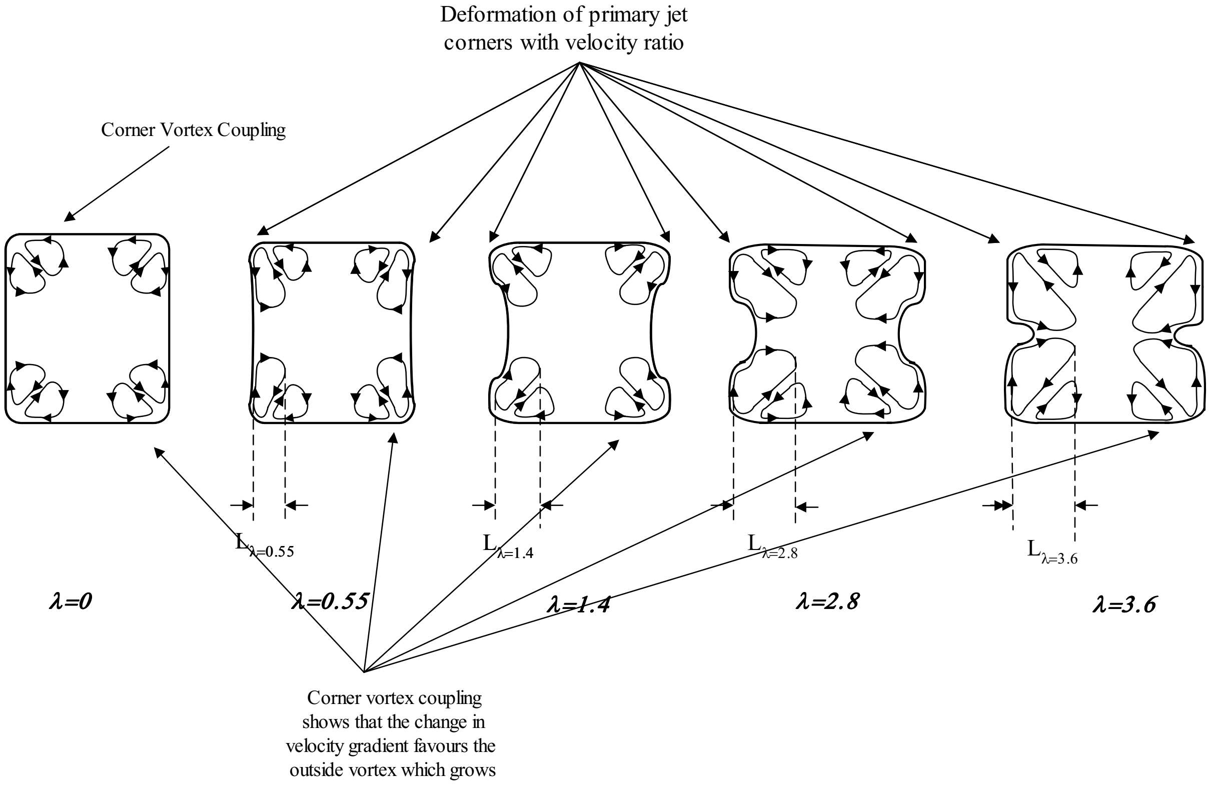

Figure 6.13: Sketch of the progressive development of the coherent corner vortices on the primary jet for λ=0, 0.55, 1.4, 2.8 and 3.6, x/D=0.5. The terms $L_{\lambda=0.55}$, $L_{\lambda=1.4}$ $L_{\lambda=2.8}$ $L_{\lambda=3.6}$ are the length scales of the corner vortices.

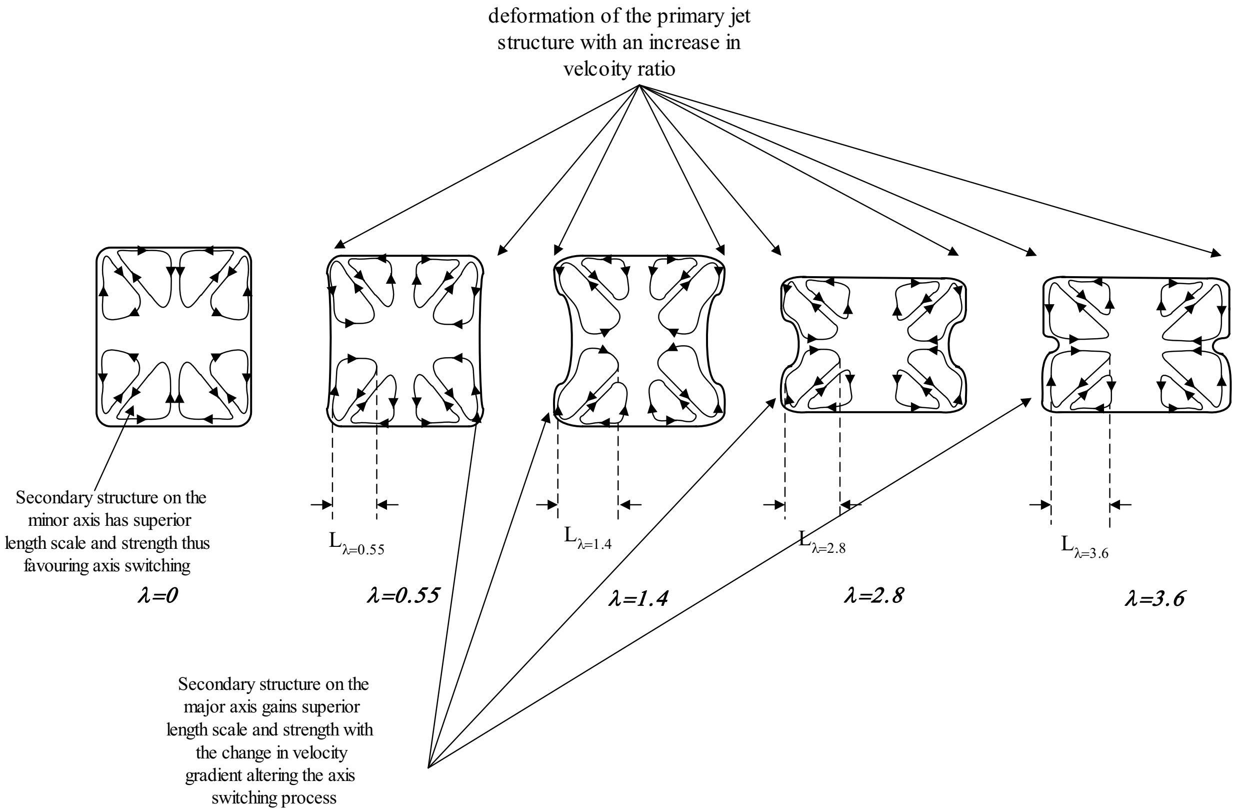

Figure 6.14: Sketch of the progressive development with λ of the coherent corner vortices on the primary jet for λ=0, 0.55, 1.4, 2.8 and 3.6, x/D=1. The terms $L_{\lambda=0.55}$, $L_{\lambda=1.4}$ $L_{\lambda=2.8}$ $L_{\lambda=3.6}$ are the length scales of the corner vortices.

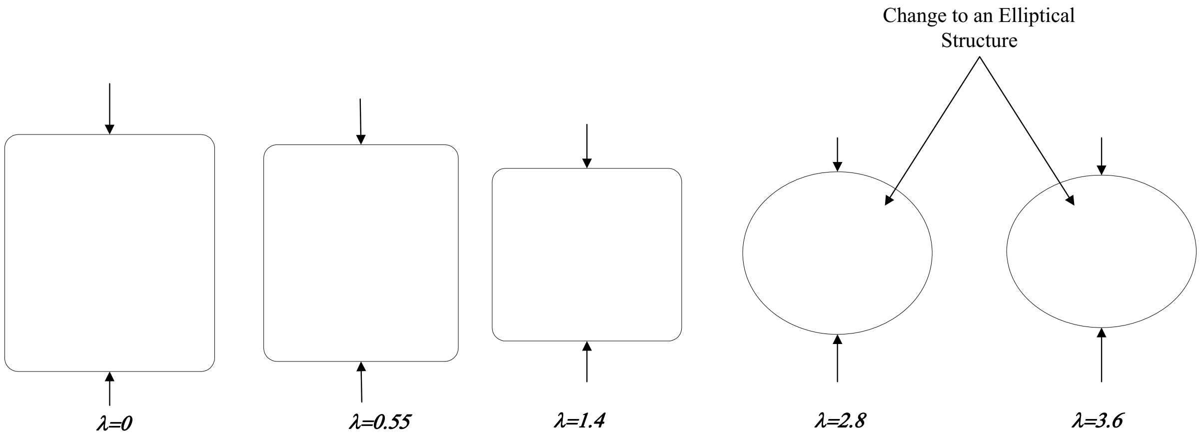

Figure 6.15: Sketch of the progressive development of the primary jet for a progressive increase in velocity ratio from λ=0 to 3.6 at x/D =2.

6.3.1.2 Primary Fluid Mixture Fraction on the Jet Axis

The inverse concentration of primary fluid on the jet axis is plotted for λ=0, 0.55, 1.4, 2.8 and 3.6 in Figure 6.16. The results are compared with the free round jet results obtained during the validation in Section 5.5 and with those of Parham (2000). A feature of the primary jet data is that it is linear for x/D >4, suggesting self-similarity in the near field for each λ. The gradient of the inverse mixture fraction in the self-similar region increases with λ. A steep gradient indicates high rates of dilution. For λ=3.6, the linear region gradient is within x/D =2 and x/D=4. Using the inverse mixture fraction decay law in Equation 2.23, the values of the first order decay constant and first order virtual origin were fitted to the self similar regions and are tabulated in Table 6.2.

For λ=0.55 and 1.4 the values of K_1 are broadly comparable with the round pipe jet (Section 5.5.4) and the results of Parham (2000). It is noted that K_1 is less at λ=0.55 than at λ=1.4. The greater dilution of the primary jet under higher co-flowing conditions is also observed when plotting K_1 versus λ in Figure 6.17. The correlation between K_1 and λ shows that it does significantly decrease with λ. Higher values of K_1 causes the centerline mixture fraction to decrease, implying higher rates of dilution on the centerline.

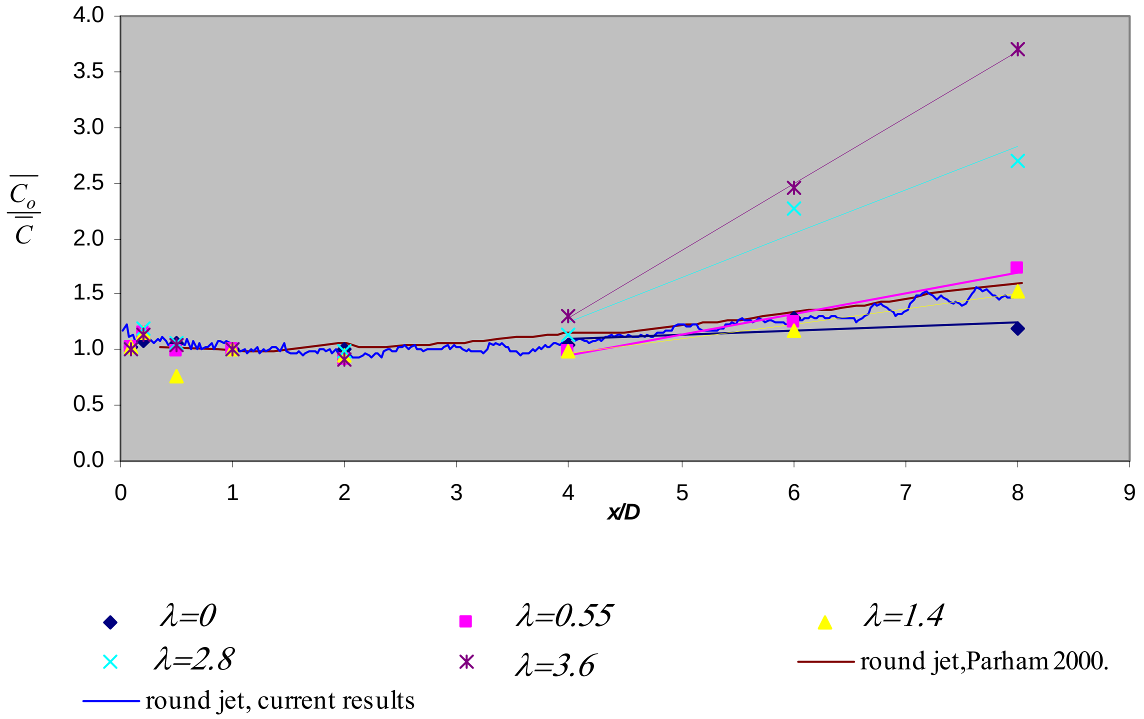

Figure 6.16 Inverse centreline mixture fraction versus dimensionless axial distance for the primary jet at velocity ratios of λ=0, 0.55, 1.4, 2.8 and 3.6 compared with round pipe jet data (Current results, Section 5.5.4 and Parham, 2000). The straight line represents the linear fits in the self-similar region.

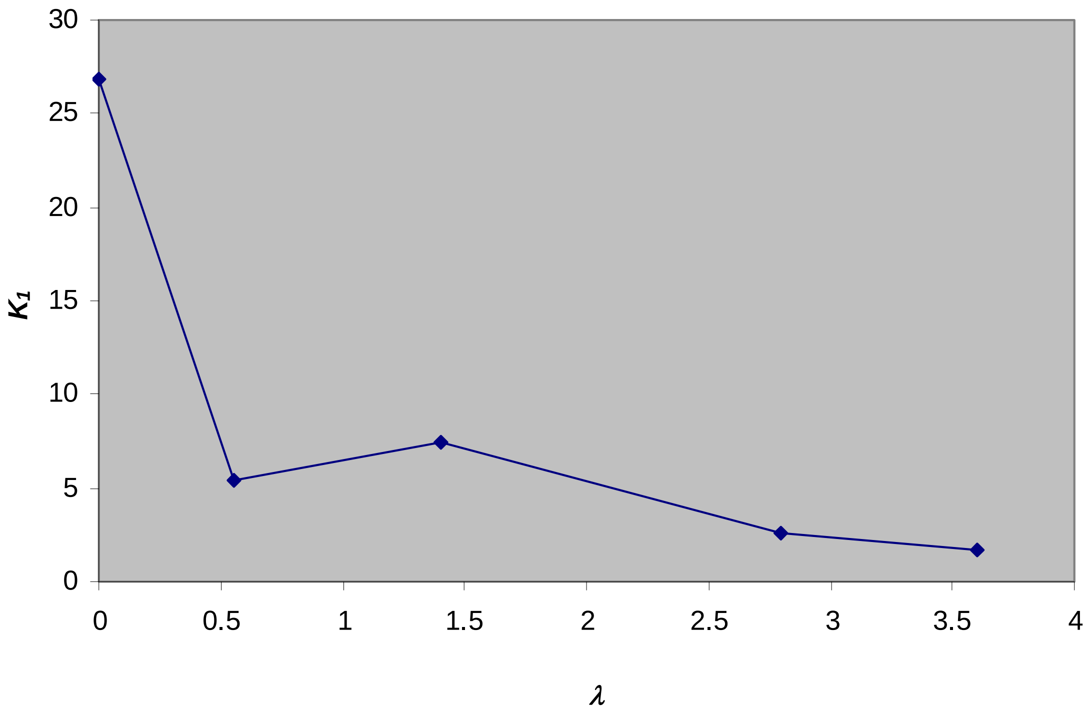

Figure 6.17 Correlation between K_1 of the primary and the secondary to primary velocity ratio.

λ	K_1	x_{01}/D
0	26.88	25.27
0.55	5.41	1.09
1.4	7.41	3.10
2.8	2.56	-0.79
3.6	1.66	-1.86

Table 6.2: Measured values of the Centreline decay constant K_1 and the primary virtual origin of the primary jet as a function of velocity ratio obtained between $4<x/D<8$.

6.3.1.3 Primary Jet Cross Stream Mixture Fraction

The radial distribution of time-averaged normalised concentrations of the primary jet at various cross stream planes are shown in Figures 6.18–6.23 for the axial stations of x/D =0.1, 0.2, 0.5, 1, 2 and 4, through different planes of z/D. Figures 6.25-6.27 at x/D =1, 2 and 4, through different planes of y/D. A complete set of the cross-stream normalised concentration profiles in the y and z direction for the primary and secondary jet at all experimental velocity ratios are provided in Appendix B.

Figure 6.18 shows the variation in normalised concentration with y/D at various z/D near to the nozzle exit plane (x/D =0.1). The normalised concentration exhibits a sharp concentration gradient in the far shear layer at the edge of the jet for all λ. This concentration profile approximates a top hat profile. However, near to the corners (z/D~0.35, y/D ~ 0.37) sharp peaks in the mean concentration are found at λ =1.4, 2.8 and 3.6. This is further evidence of change of the coherent corner vortices. These peaks are also present at x/D =0.2, and x/D =0.5 in Figures 6.19 and 6.20 at λ=1.4, 2.8 and 3.6, but are less evident in these Figures (although the vortices are still present in the jet).

The planar data in Section 6.3.1.1 shows that the higher co-flowing conditions cause the coherent corner vortices to extend the primary jet in the z-direction, which consequently changes the cross-stream concentration profiles. The cross-stream profiles in Figure 6.21 and Figure 6.22 at x/D =1 and 2, show that there is an increase in concentration gradient from velocity ratios λ=0.55 to 3.6. This corresponds to the progressive contraction of the primary jet observed at x/D =1 and x/D =2 at λ=1.4 – 3.6 in the time-averaged planar data in Section 6.3.1.1. In Figure 6.23 at x/D

=4 an increase in concentration gradient is only observed up to λ=2.8. Using the concentration of the linear region (manually determined using a line of best fit with maximum R^2 value) at z/D =0 from Figures 6.21 to 6.23, the concentration gradient was calculated and is compared for all velocity ratios. Figure 6.24 presents the dimensionless absolute value of the concentration gradient in the y-direction $\left|\frac{D}{\overline{C_c}}\frac{\Delta\overline{C}}{\Delta y}\right|$ at x/D = 1, 2 and 4 versus velocity ratio. There is a distinct correlation between $\left|\frac{D}{\overline{C_c}}\frac{\Delta\overline{C}}{\Delta y}\right|$ and λ, for x/D =1 and 2, but the correlation is weak at x/D =4.

The cross-stream concentration profiles versus z/D through different planes of y/D are illustrated in Figures 6.25-6.27 at x/D =1, 2 and 4. Changes in concentration gradients are observed in all figures starting from the higher co-flowing conditions from λ=0.55 to 3.6 at x/D =1 where a slight increase in slope is observed in the linear region of the Gaussian profile. The cross-stream concentration profiles at x/D = 2 and 4 in Figures 6.26 and 6.27 show that the concentration gradient increases from λ=0.55 to 2.8 and decreases from λ=2.8 to 3.6. These results are consistent with the analysis of the planar images of the primary jet in Section 6.3.1.1. Plotting the dimensionless concentration gradient in the z-direction $\left|\frac{D}{\overline{C_c}}\frac{\Delta\overline{C}}{\Delta z}\right|$ versus λ in Figure 6.28, shows that there is a decline in gradient with λ at x/D =1, implying that the jet is expanding in the z-direction, on the contrary at x/D =2 where the gradient is increasing with λ, corresponding to a contraction, which are also consistent with observations from sections 6.3.1.1 and 4.4.3.

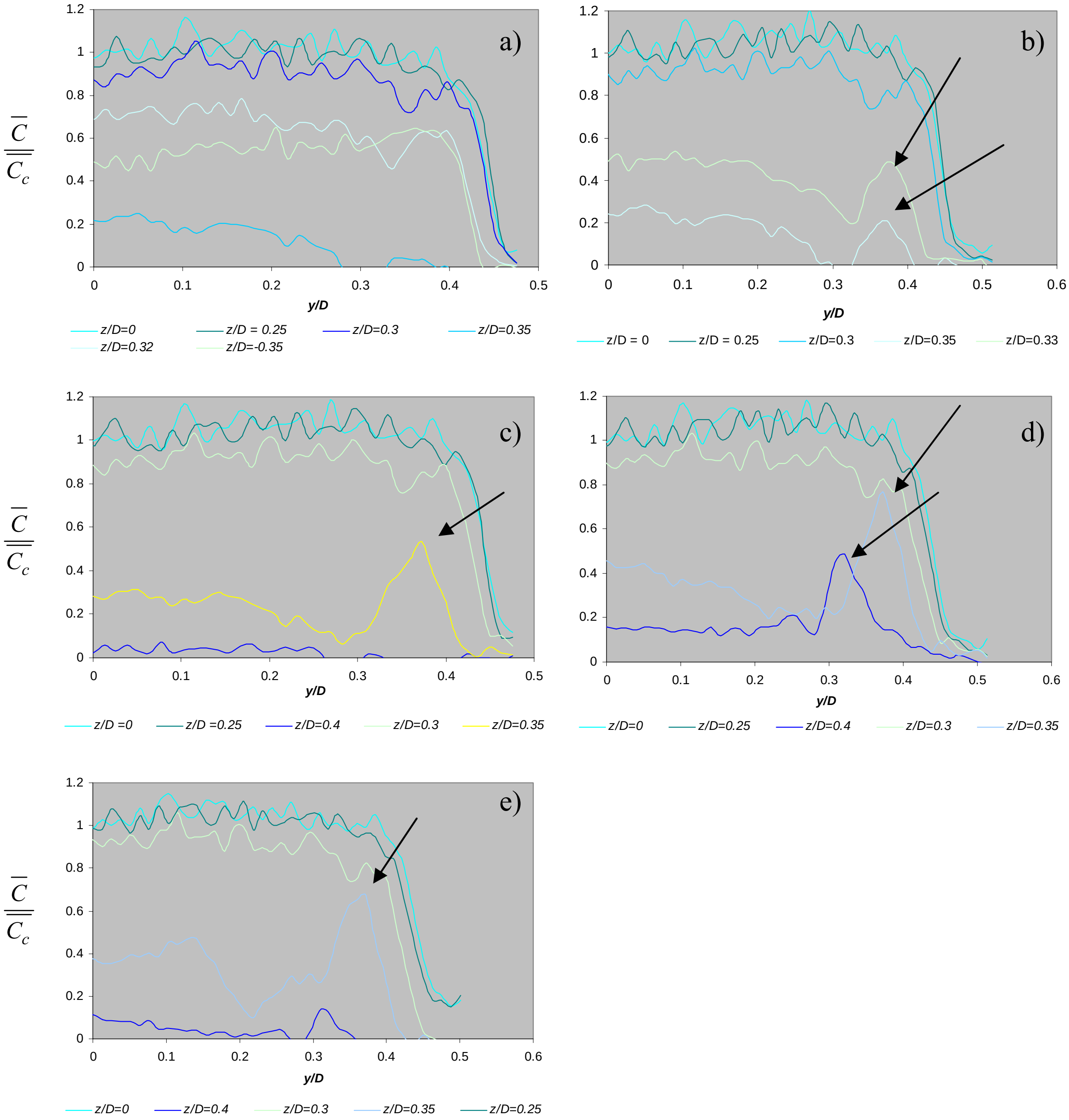

Figure 6.18: Normalised Concentration of the primary jet versus *y/D* through different *z/D* planes, at *x/D* =0.1, a) λ=0, b) λ=0.55, c) λ=1.4, d) λ=2.8, e) λ=3.6. The black arrows highlight the peaks corresponding to the distortion of the exit jet by the emergence of the corner vortex.

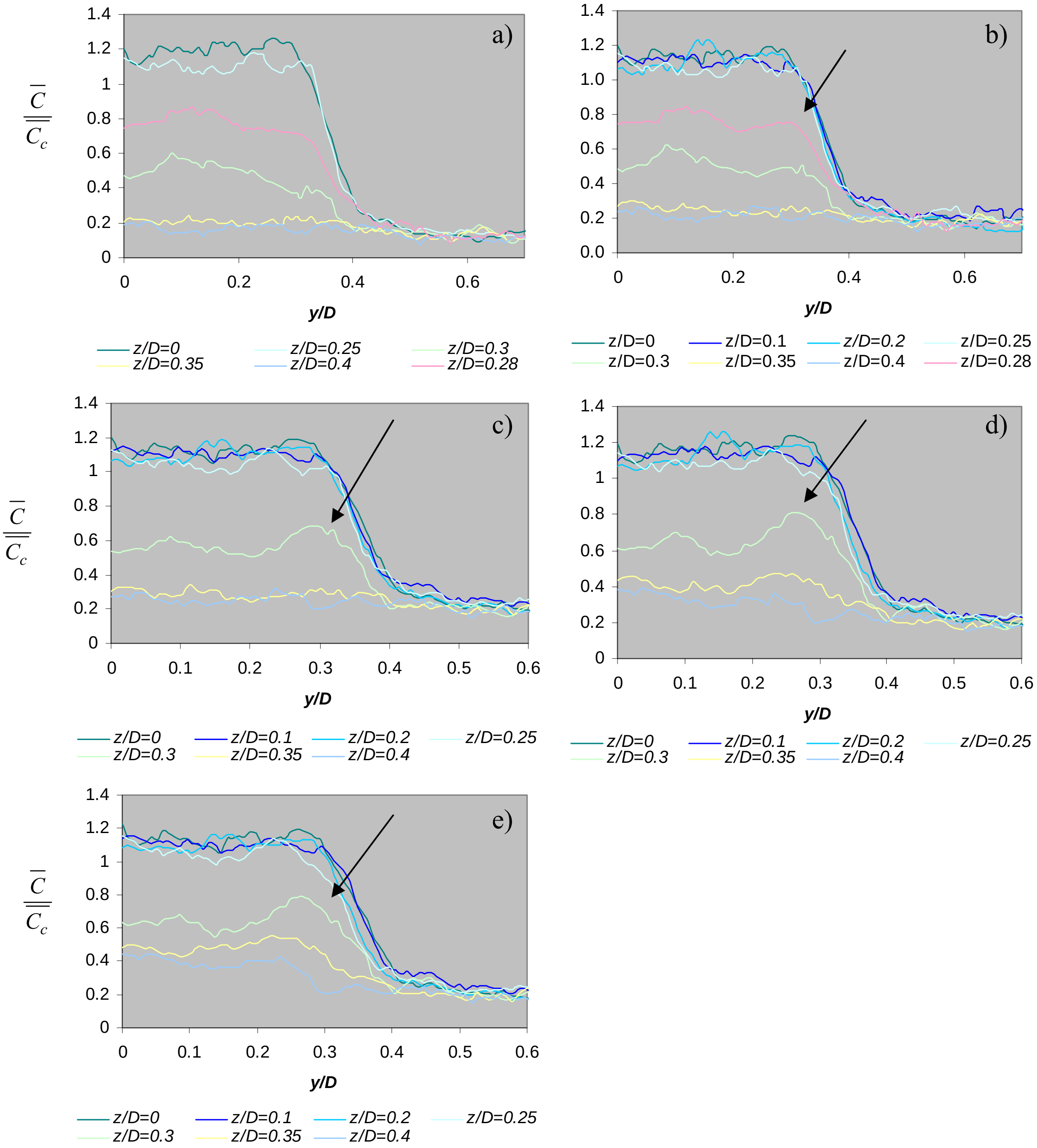

Figure 6.19: Normalised Concentration of the primary jet versus *y/D* through different *z/D* planes, at *x/D* =0.2, a) λ=0, b) λ=0.55, c) λ=1.4, d) λ=2.8, e) λ=3.6. The black arrows highlight the peaks corresponding to the distortion of the exit jet by the emergence of the corner vortex.

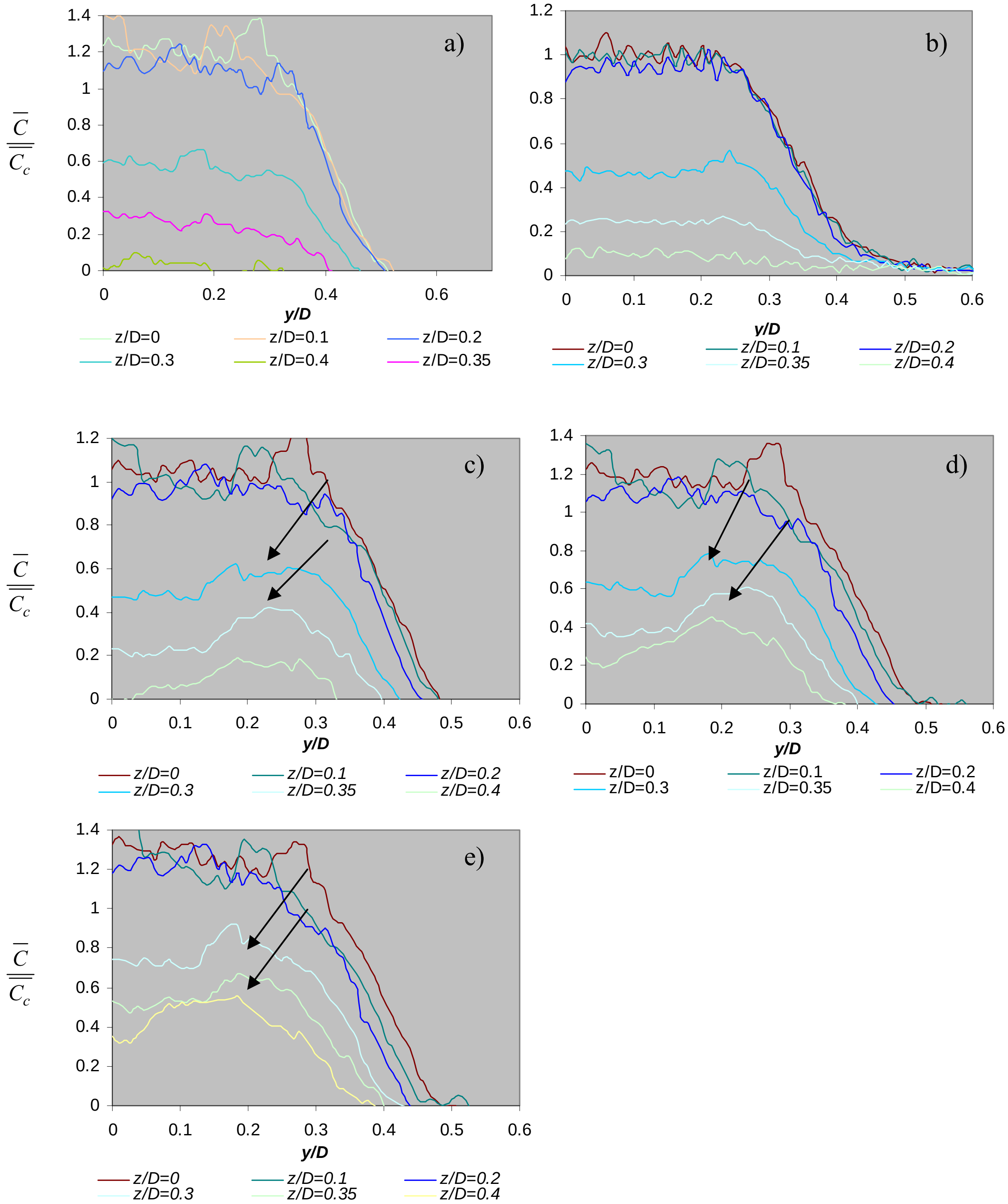

Figure 6.20: Normalised Concentration of the primary jet versus *y/D* through different *z/D* planes, at *x/D* =0.5, a) λ=0, b) λ=0.55, c) λ=1.4, d) λ=2.8, e) λ=3.6. The black arrows highlight the peaks corresponding, to the coherent corner vortices of fluid in close proximity to the corners of the primary jet.

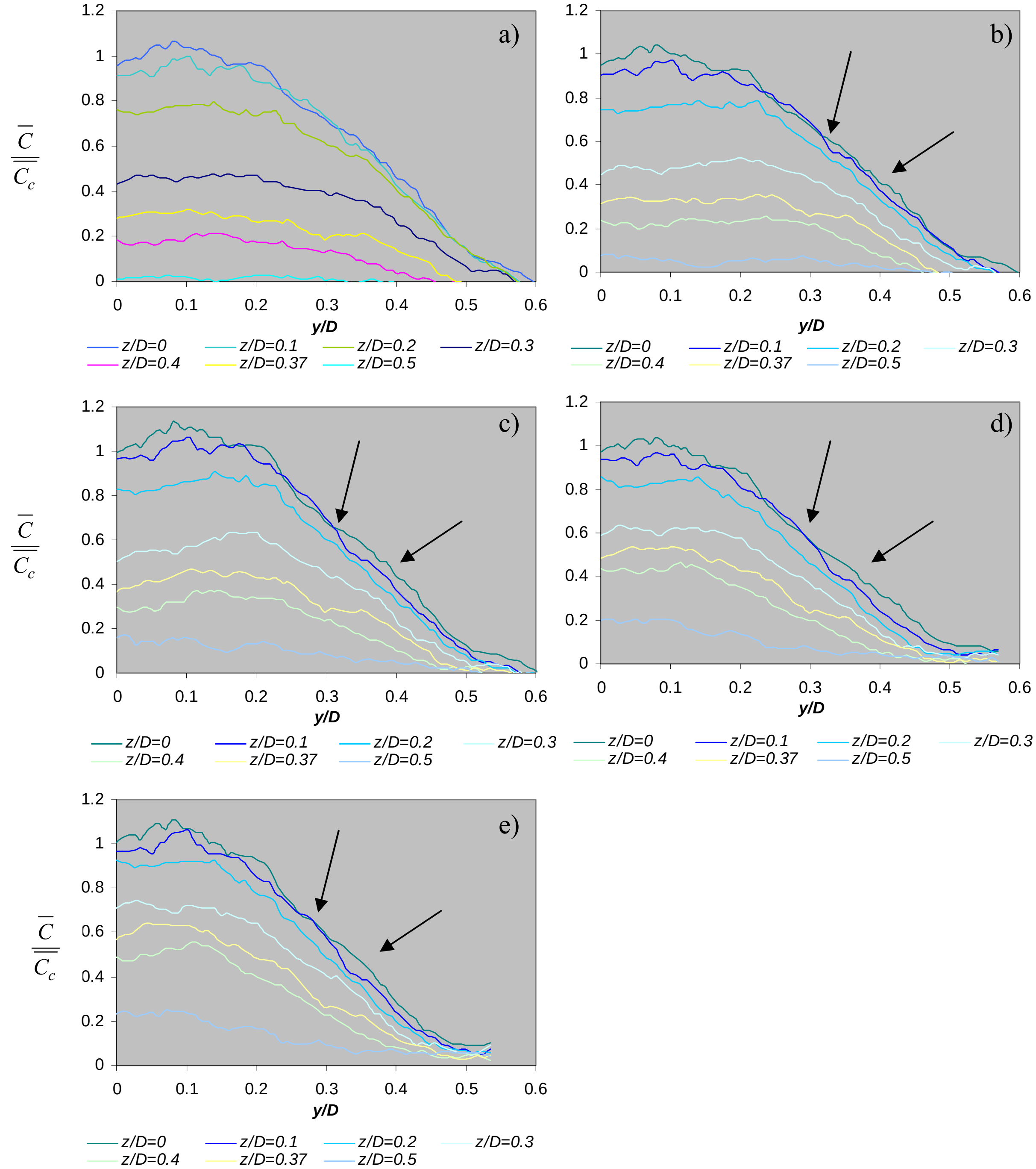

Figure 6.21: Normalised Concentration of the primary jet versus *y/D* through different *z/D* planes, at *x/D* =1, a) λ=0, b) λ=0.55, c) λ=1.4, d) λ=2.8, e) λ=3.6. The black arrows outline a progressive increase in concentration gradient with an increase in co-flowing conditions (λ).

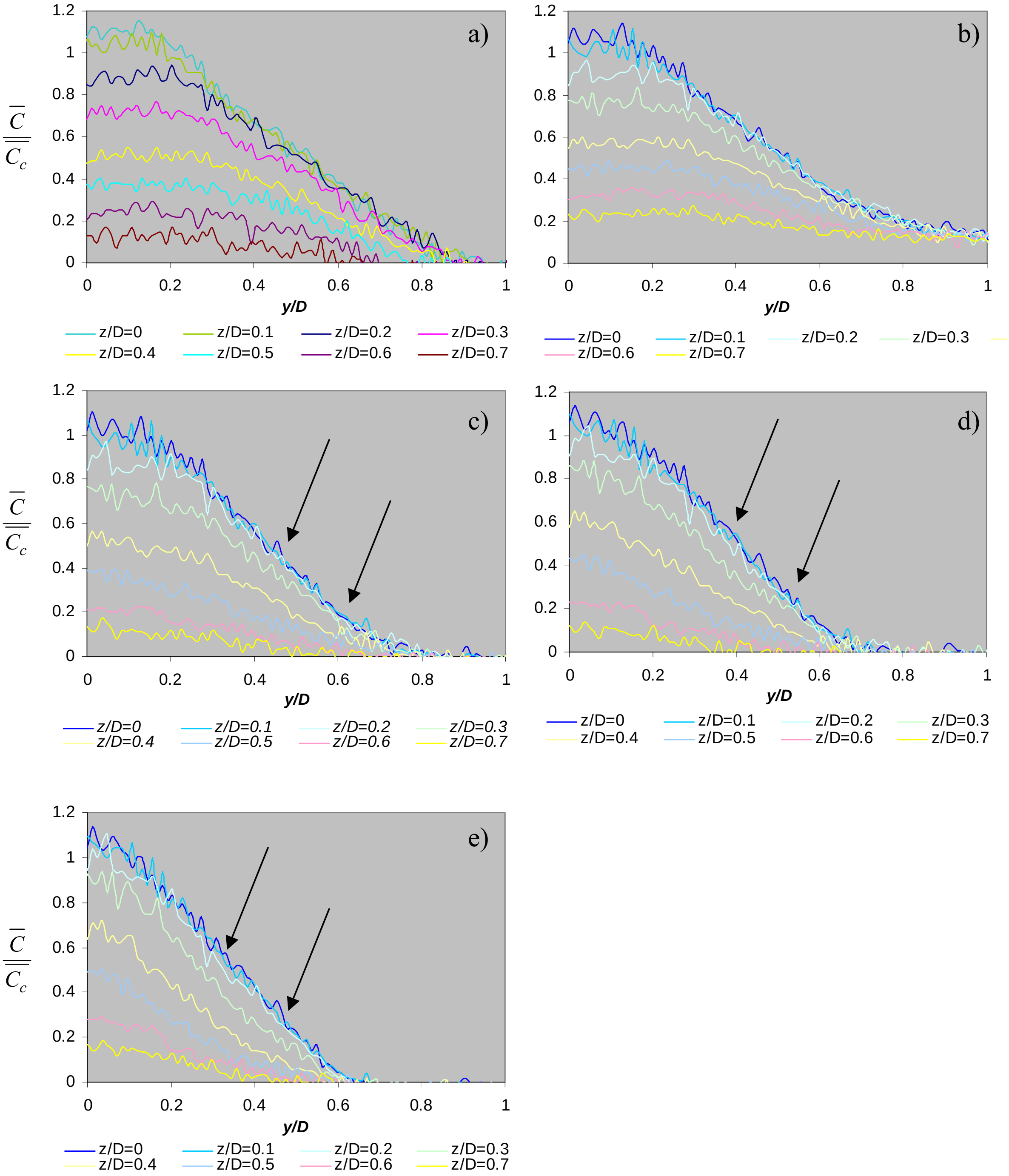

Figure 6.22: Normalised Concentration of the primary jet versus *y/D* through different *z/D* planes, at *x/D* =2, a) λ=0, b) λ=0.55, c) λ=1.4, d) λ=2.8, e) λ=3.6. The black arrows outline a progressive increase in concentration gradient with an increase in co-flowing conditions (λ).

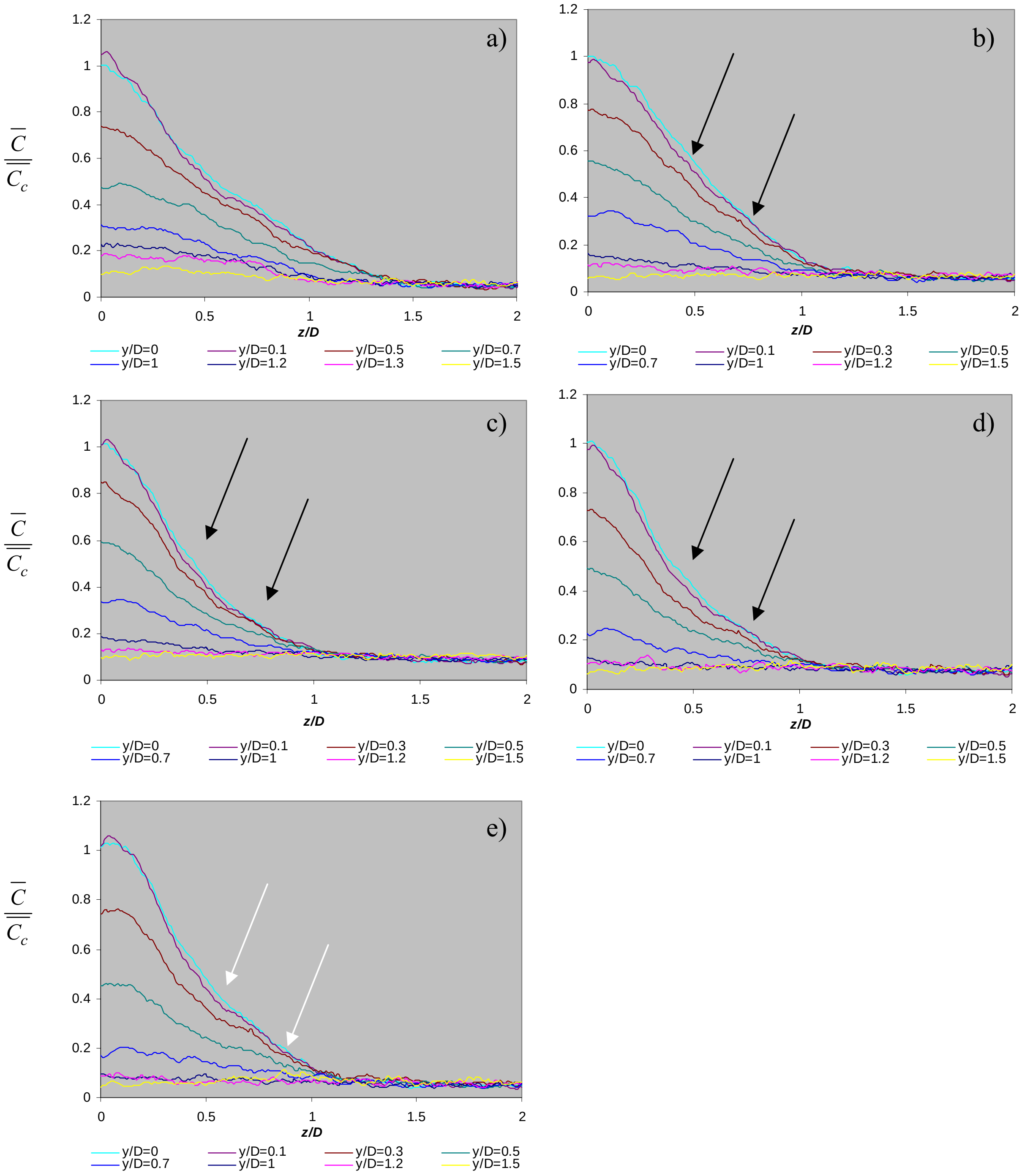

Figure 6.23: Normalised Concentration of the primary jet versus *z/D* through different *y/D* planes, at *x/D* =4, a) λ=0, b) λ=0.55, c) λ=1.4, d) λ=2.8, e) λ=3.6. The black arrows outline a progressive increase in concentration gradient with an increase in co-flowing conditions of λ=0.55, 1.4 and 2.8. The white arrows highlight a decrease in concentration gradient at λ=3.6.

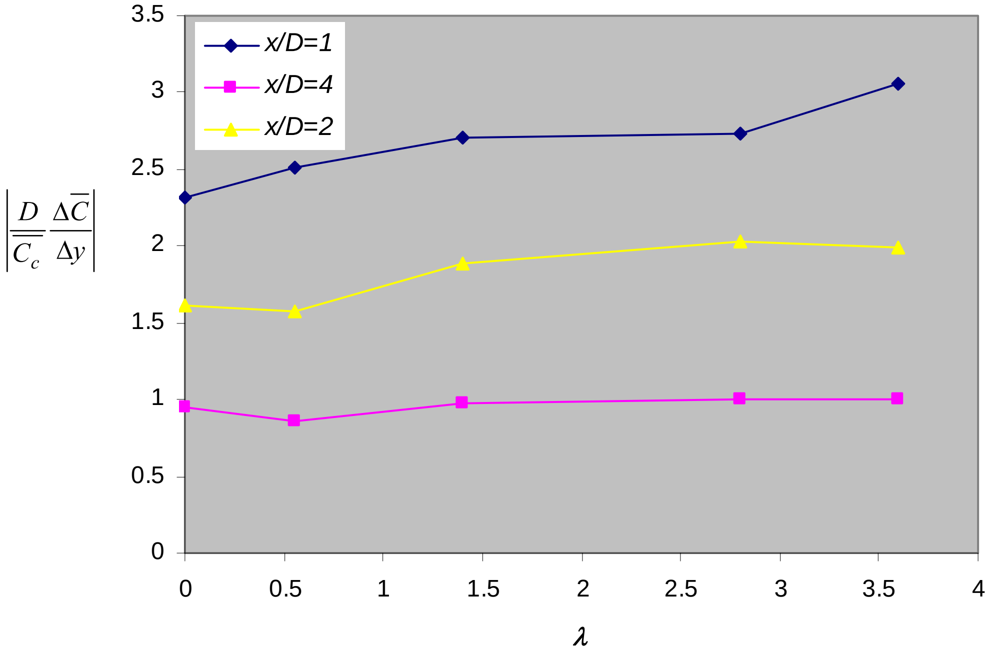

Figure 6.24: Absolute value of the dimensionless concentration gradient in the *y*-direction versus velocity ratio of the primary jet, for *z/D* =0.

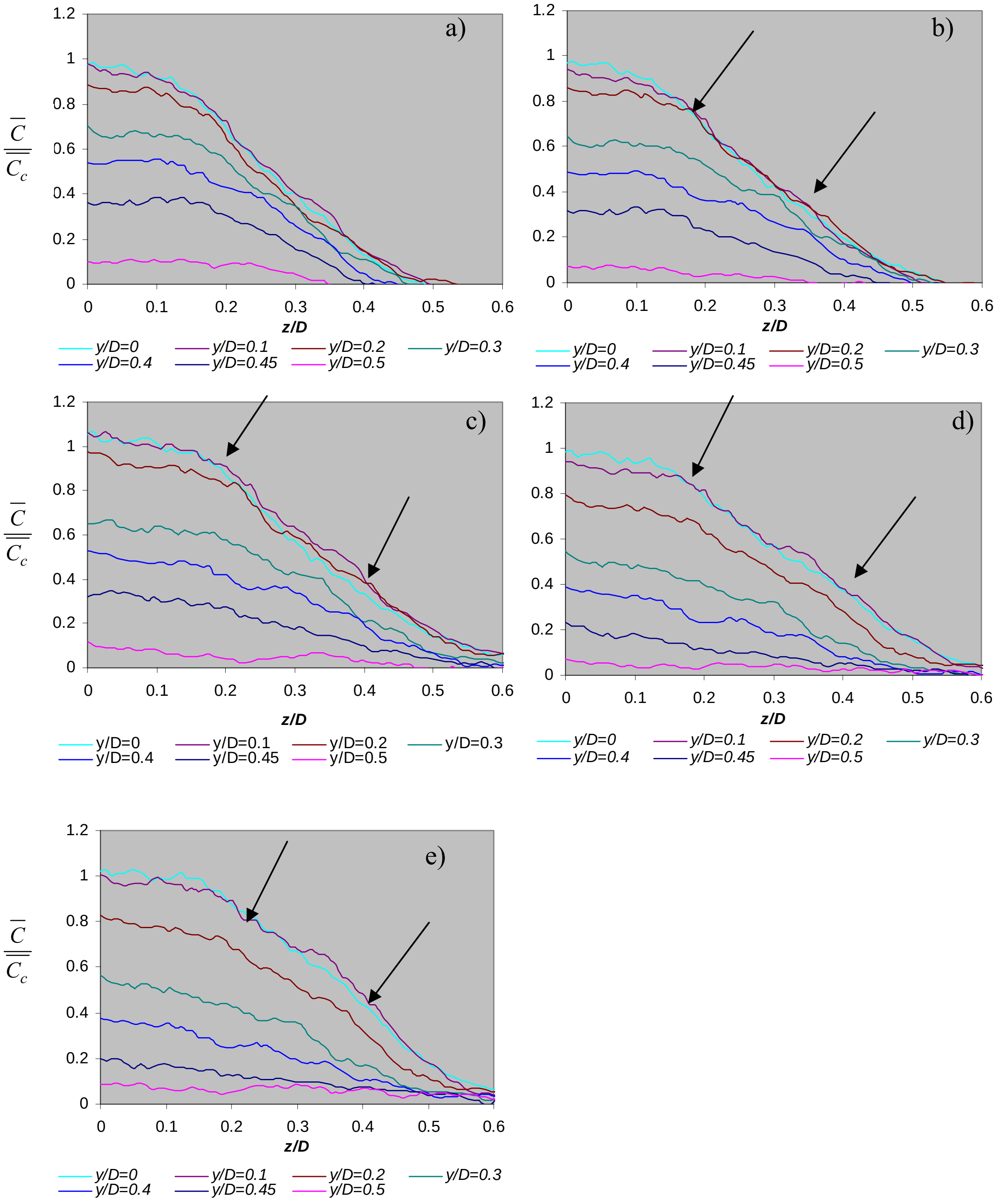

Figure 6.25: Normalised Concentration of the primary jet versus *z/D* through different *y/D* planes, at *x/D* =1, a) λ=0, b) λ=0.55, c) λ=1.4, d) λ=2.8, e) λ=3.6. The black arrows outline a progressive decrease in concentration gradient with an increase in co-flowing conditions (λ).

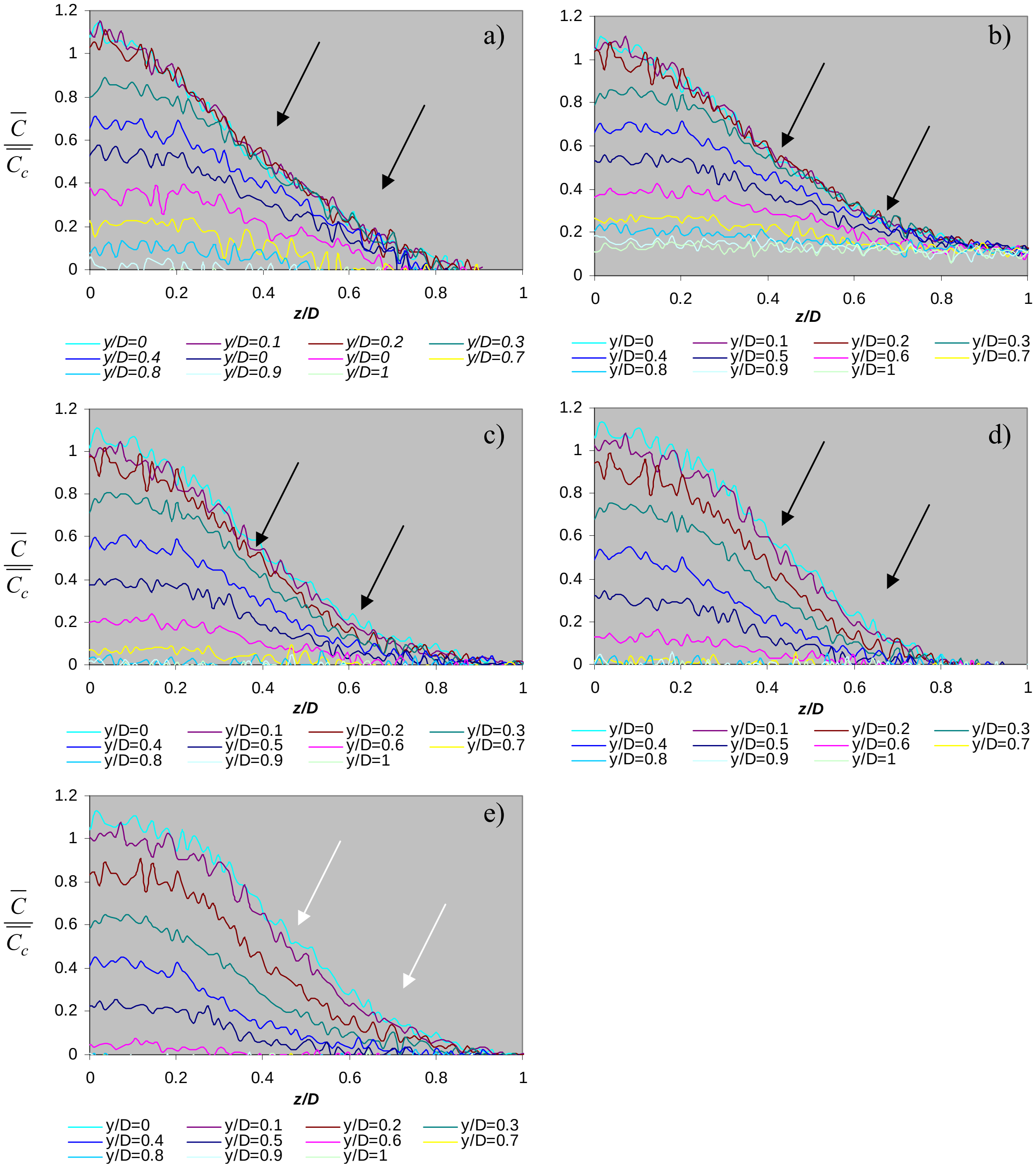

Figure 6.26: Normalised Concentration of the primary jet versus *z/D* through different *y/D* planes, at *x/D* =2, a) λ=0, b) λ=0.55, c) λ=1.4, d) λ=2.8, e) λ=3.6. The black arrows outline a progressive increase in concentration gradient with an increase in co-flowing conditions from λ=0.55 to 1.4 and 2.8. The white arrows highlight a decrease in concentration gradient at λ=3.6.

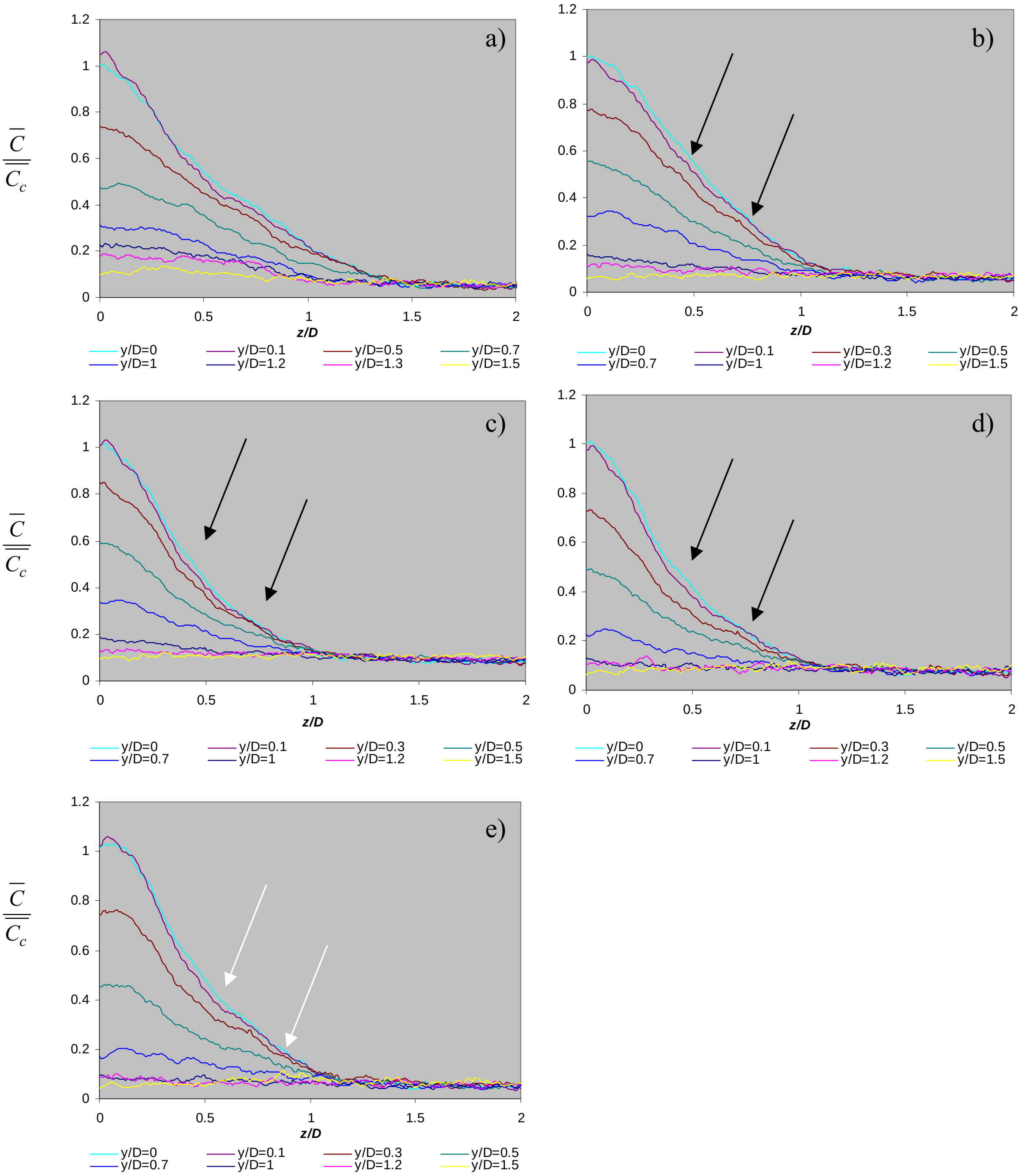

Figure 6.27: Normalised Concentration of the primary jet versus *z/D* through different *y/D* planes, at *x/D* =4, a) λ=0, b) λ=0.55, c) λ=1.4, d) λ=2.8, e) λ=3.6. The black arrows outline a progressive increase in concentration gradient with an increase in co-flowing conditions of λ=0.55, 1.4 and 2.8. The white arrows highlight a decrease in concentration gradient at λ=3.6.

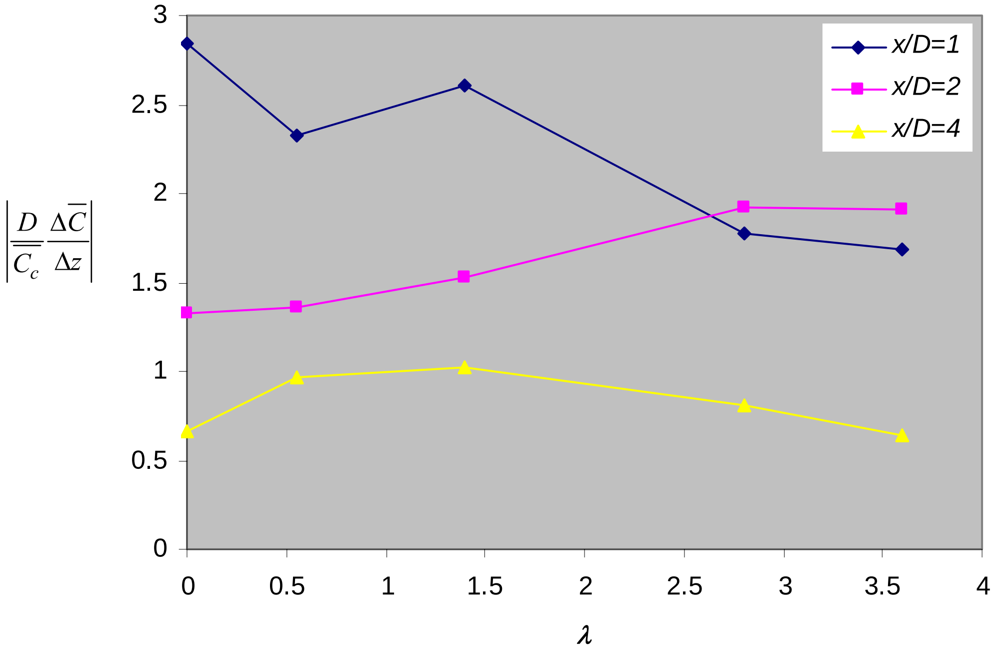

Figure 6.28: Absolute value of the dimensionless concentration gradient in the *z*-direction versus velocity ratio of the primary jet for *y/D* =0.

6.3.1.4 Discussion

The secondary structures embedded within a rectangular jet are strongly influenced by the resultant velocity gradient of the primary and secondary jets and become strong features in the mean flow field causing distortion of the jet structure at higher velocity ratios with respect to λ=0. These flow structures are very important to flow development. Downstream these structures progressively increase in size as the shear layer of the primary jet also increases through mixing, causing them to be attracted to one another on each side of the major axis and causing the jet to expand in the *z*-direction and contract in the *y*-direction further downstream at approximately *x/D* =2. This expansion/contraction effect observed at *x/D* =2 becomes more apparent with higher velocity ratios, also having effects on the concentration gradients in the *y* and *z* directions.

The dilution of centerline jet fluid is a good indication of when the primary/secondary jet interaction becomes momentum controlled, because the concentration of the jet on the centerline is determined by the vortex ring. Centerline mixture fraction data reveals that the region between *x/D* =2 and *x/D* =4 primary and secondary jet mixing becomes momentum controlled.

The extent of dilution of the primary jet on the centerline is strongly controlled by the secondary to primary velocity ratio. This is supported with conclusions drawn from Chapter 4.

6.3.2 Secondary Jet

6.3.2.1 Planar Data

Figures 6.29 to 6.36 present the time averaged normalised concentrations of the secondary jet fluid at axial stations of *x/D* =0.1, 0.2, 0.5, 1, 2, 4, 6 and 8 for λ=0.55, 1.4, 2.8, 3.6 and ∞. The coherent corner vortices observed for the primary jet in the near field are also present in the secondary jets and is highlighted by white arrows in Figures 6.29, 6.30, 6.31 and 6.32. The coherent corner vortices are first observed in proximity to the corners of the secondary jet at *x/D* =0.1and 0.2, λ=0.55 and 1.4 and is highlighted with white arrows in Figures 6.29 and 6.30. At *x/D* =0.5 and 1 (Figures 6.31-6.32) the coherent vortices are still very much a characteristic of the flow. However the rectangular jets start to assume a rhombus-like shape, which is highlighted with black arrows. At axial stations of *x/D* =4, 6 and 8 and a velocity ratio of λ=0.55 the secondary jets in Figures 6.34a) 6.35a) and 6.36a) deviate significantly from their geometric axes (white arrows). The secondary jets appear to be fully merged at *x/D* =8 for all λ, however further upstream at *x/D* =6 only at λ=0.55 (Figure 6.35a) do the jets appear to have merged.

Figures 6.37-6.39 are schematic diagrams of the corner vortices and their change with λ. The presence of corner vortices or braids on rectangular and square jets has been well documented by a number of authors (Grinstein *et al.*, 1995, Grinstein, 2001 and Miller *et al.*, 1995) and as for the primary jet, they play an important role in the distortion of the secondary jets with λ. Figure 6.37 (*x/D*=0.1) shows how the change in velocity gradient when λ <1 favours the change in the corner vortices of the secondary jet, particularly at λ =0.55, where the corner vortices adjacent to the side of the major axis are larger and increase in size thus causing jet distortion. These distortions experienced at *x/D* =0.1 are only minor because the shear layer has not yet developed. In Figure 6.38 however, where *x/D*=0.5 the change in velocity gradients cause the corner vortices which share an interface with the primary jet to increase with size and strength at λ=0.55. The distortion at λ=0.55, *x/D* =0.5, however, is not only limited to the primary secondary jet interface, the corner vortices on the opposite side, adjacent to the minor axis side which also increase in size and strength contribute to the overall distortion of the secondary jets.

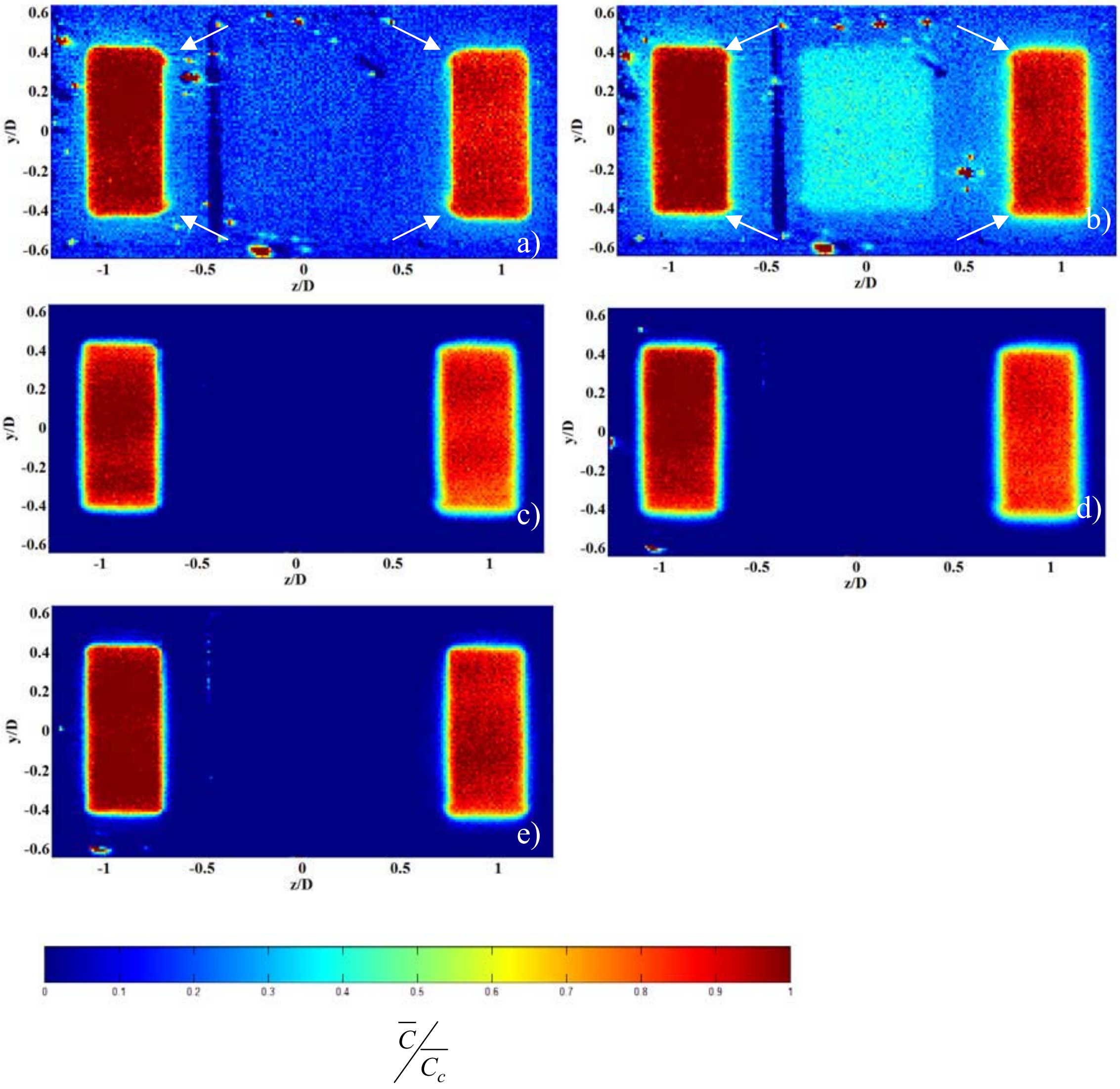

Figure 6.29: Time averaged normalised concentration of the primary jet at *x/D* =0.1, for a) λ=0.55, b) λ=1.4, c) λ=2.8, d) λ=3.6, e) $\lambda=\infty$. The white arrows highlight the mean field distortion by increased strength of corner vortices of the secondary jets.

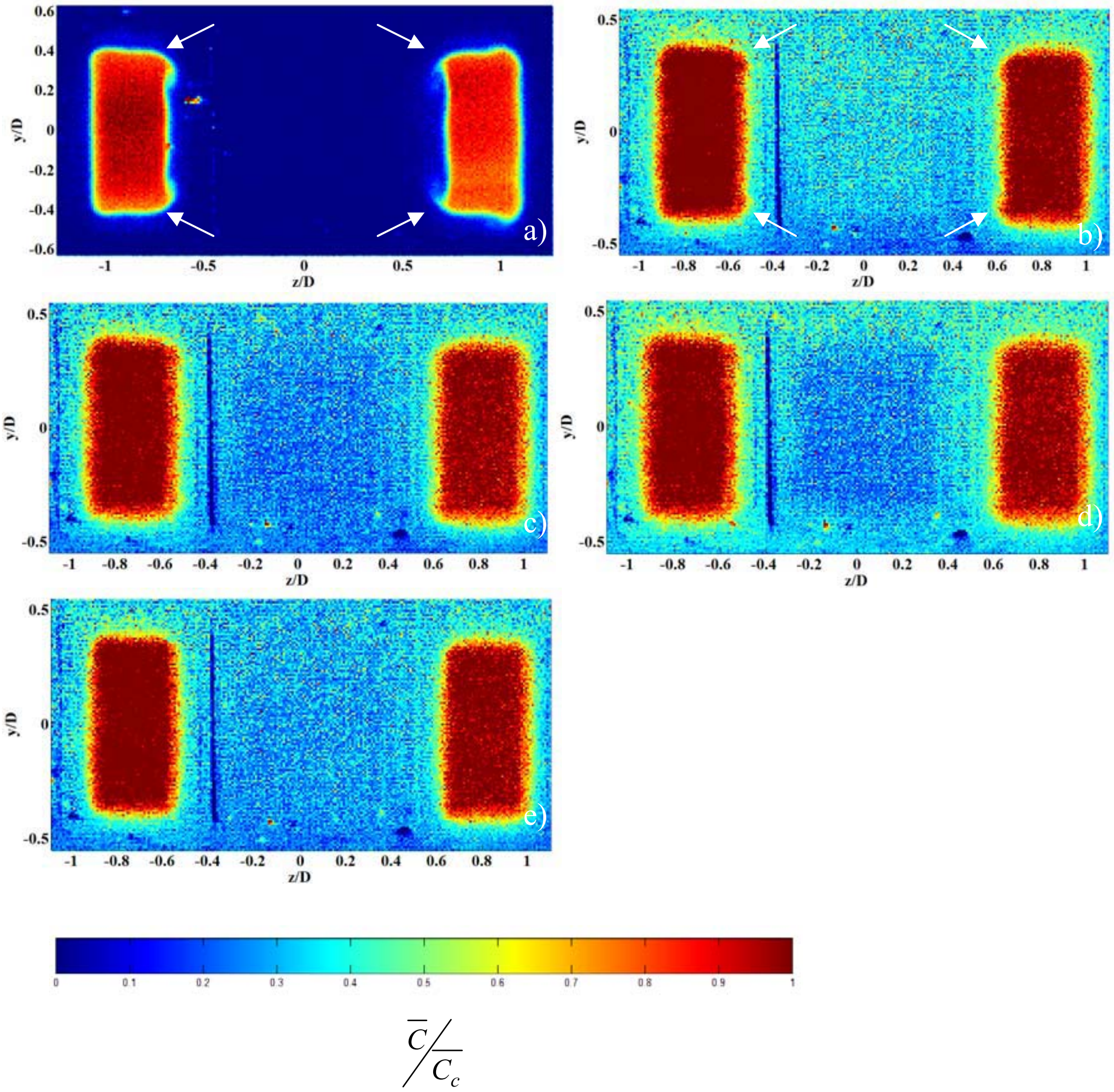

Figure 6.30: Time averaged normalised concentration of the primary jet at *x/D* =0.2, for a) λ=0.55, b) λ=1.4, c) λ=2.8, d) λ=3.6, e) λ=∞. Mean field distortion by increased strength of corner vortices of the secondary jets.

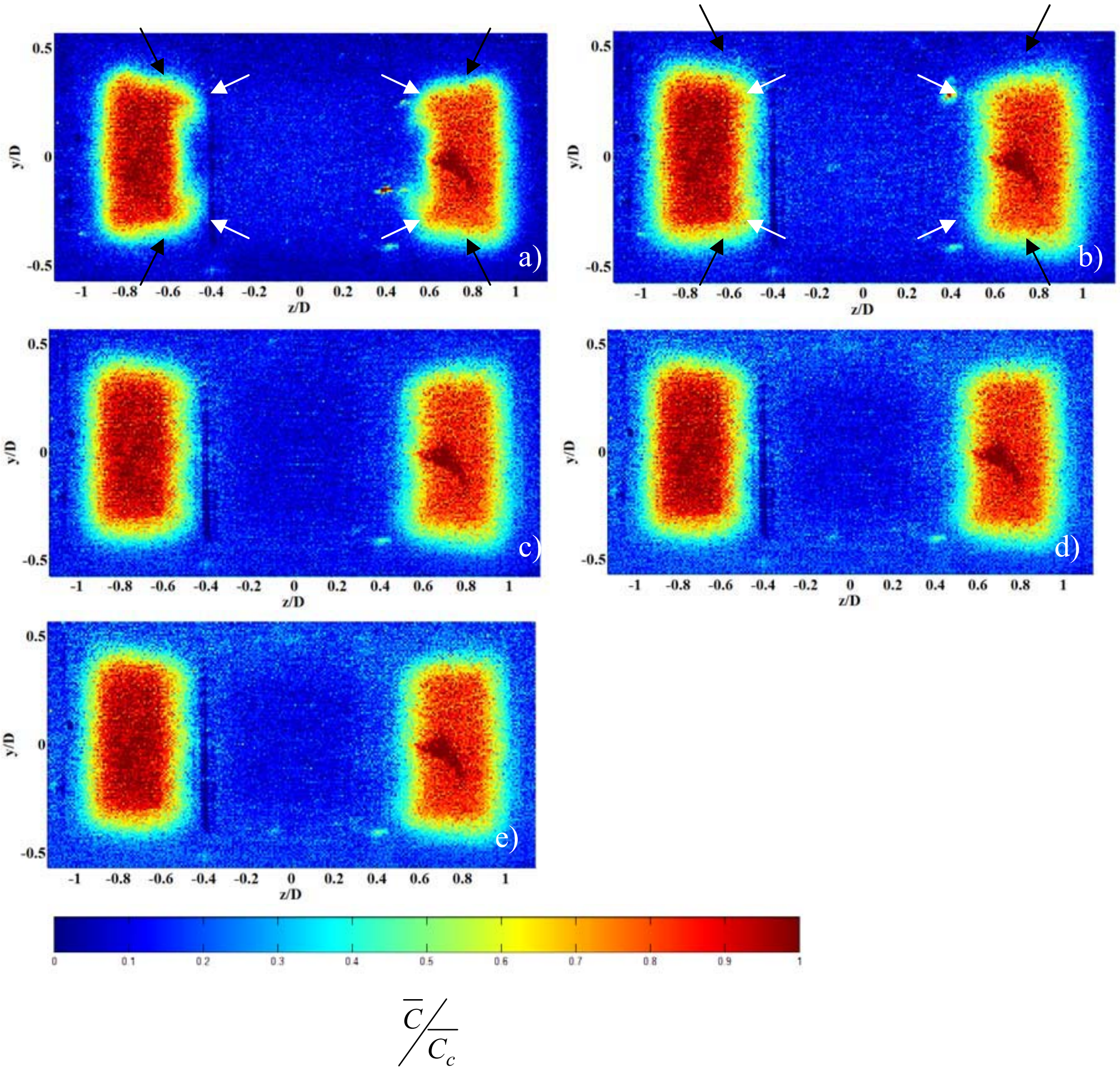

Figure 6.31: Time averaged normalised concentration of the primary jet at *x/D* =0.5, for a) λ=0.55, b) λ=1.4, c) λ=2.8, d) λ=3.6, e) λ=∞. Mean field distortion by increased strength of corner vortices of the secondary jets. The black arrows outline a deformation of the secondary jet from a rectangular structure to a rhombus like shape.

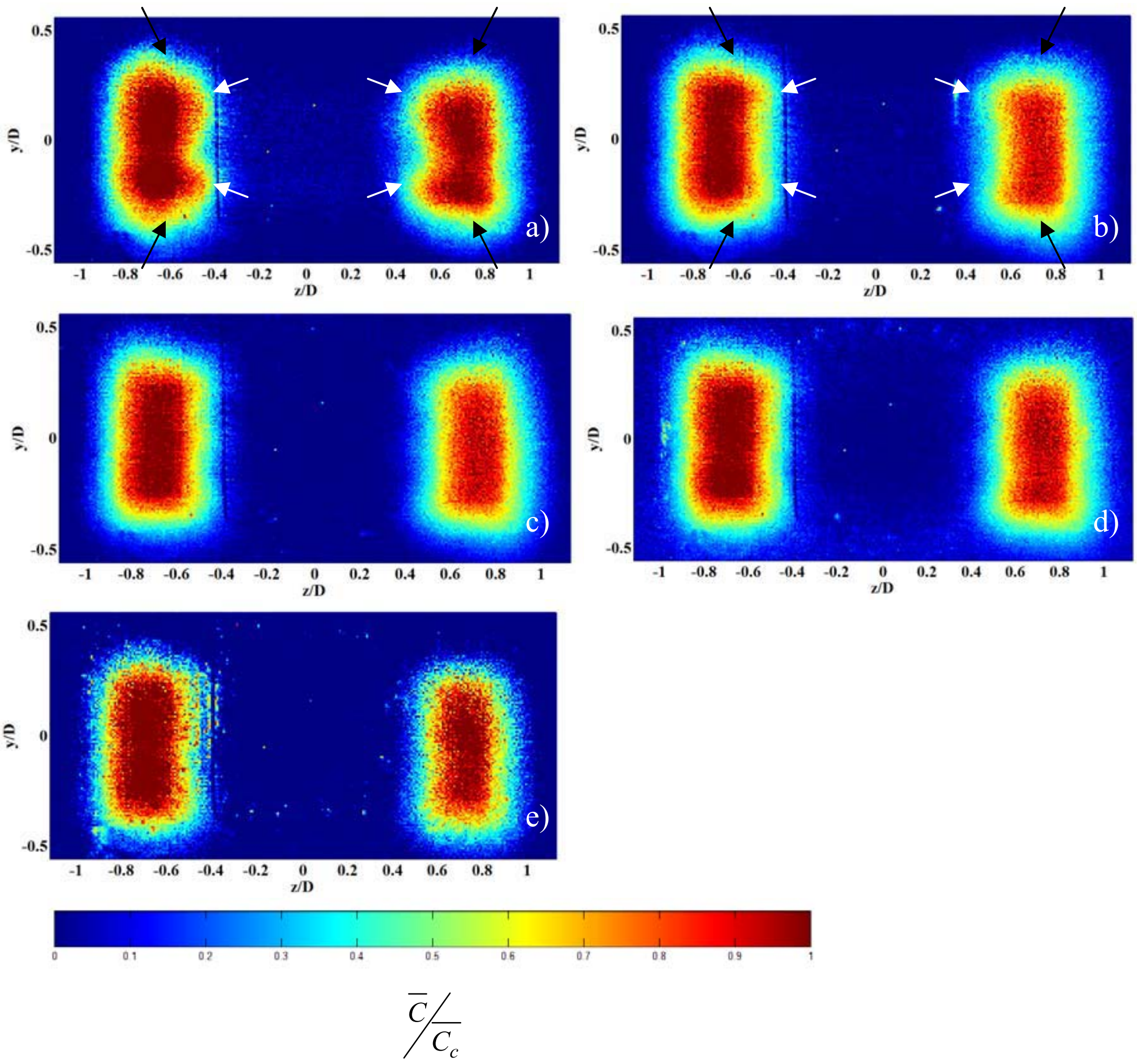

Figure 6.32: Time averaged normalised concentration of the primary jet at x/D =1, for a) λ=0.55, b) λ=1.4, c) λ=2.8, d) λ=3.6, e) $\lambda=\infty$. Mean field distortion by increased strength of corner vortices of the secondary jets. The black arrows outline a deformation of the secondary jet from a rectangular structure to a rhombus like shape.

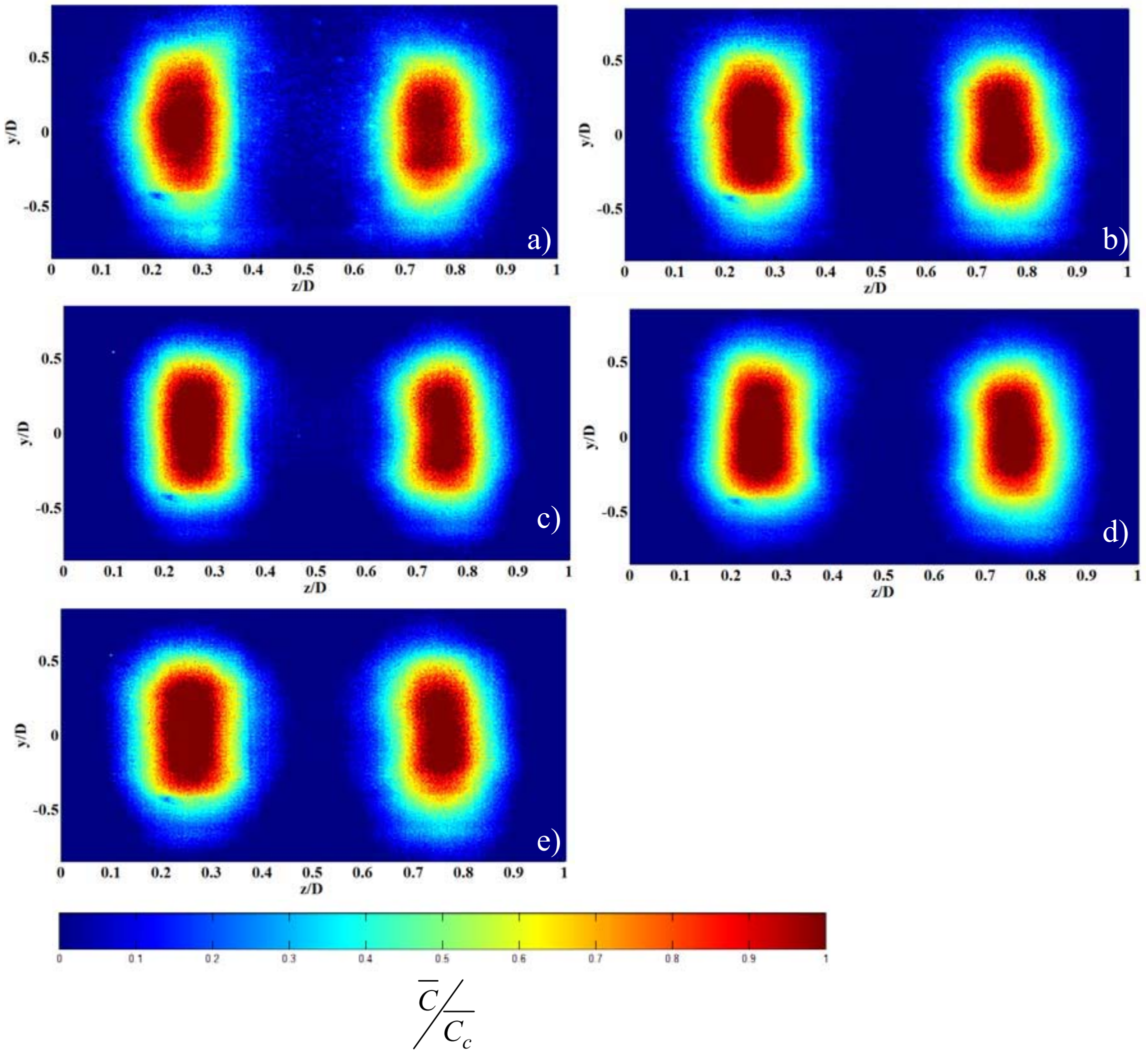

Figure 6.33: Time averaged normalised concentration of the primary jet at *x/D* =2, for a) λ=0.55, b) λ=1.4, c) λ=2.8, d) λ=3.6, e) $\lambda=\infty$.

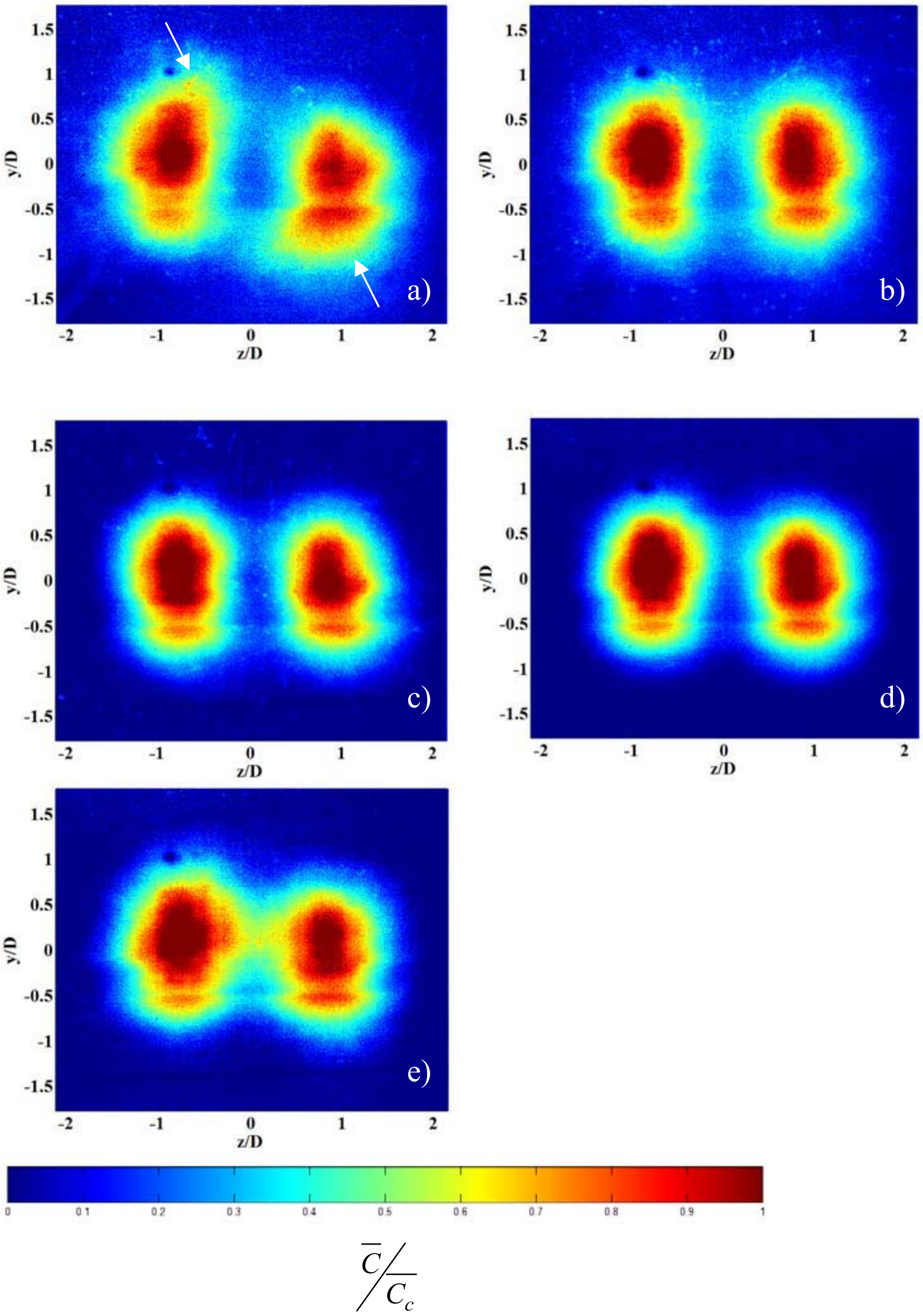

Figure 6.34: Time averaged normalised concentration of the primary jet at *x/D* =4, for a) λ=0.55, b) λ=1.4, c) λ=2.8, d) λ=3.6, e) λ=∞. The white arrows highlight the deviation of the secondary jets from their geometric axis when λ=0.55.

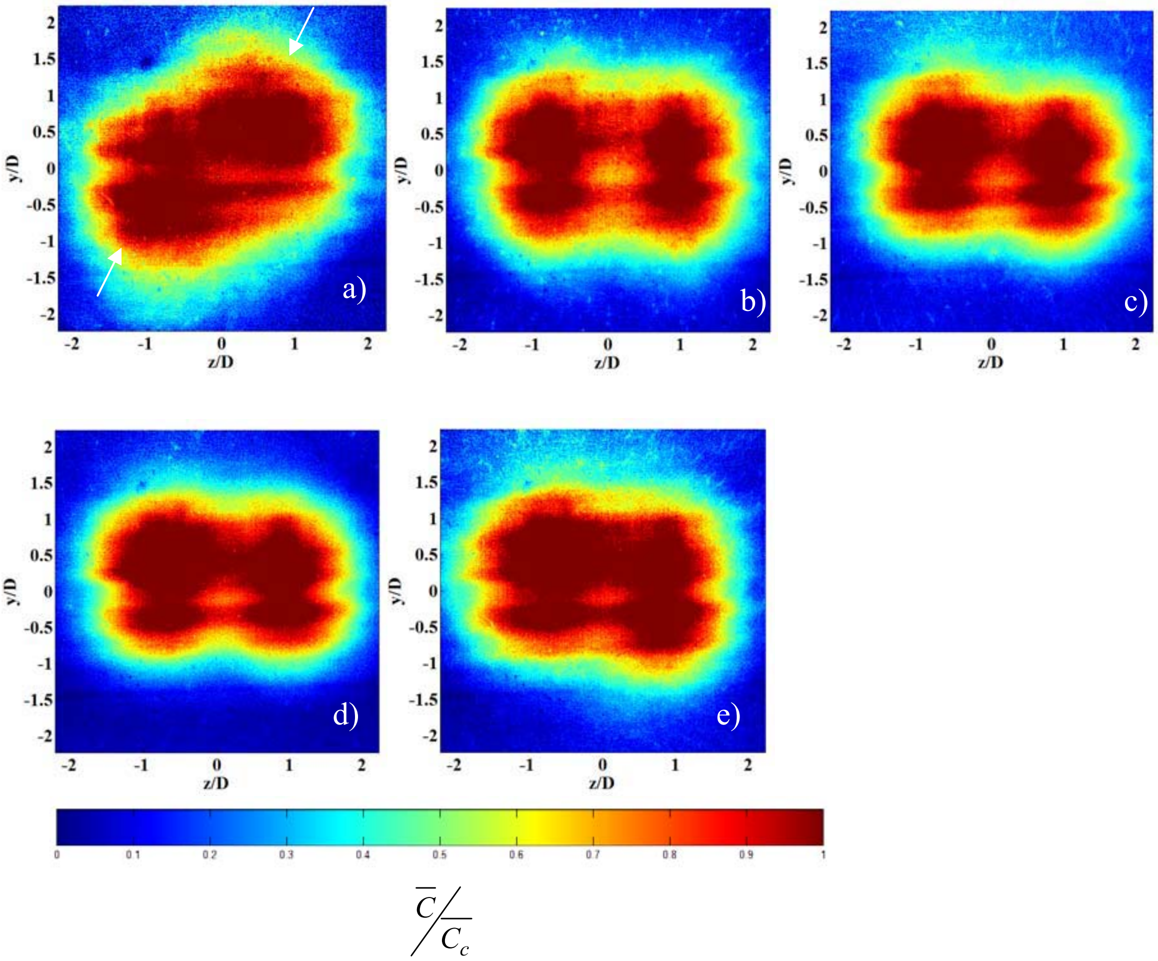

Figure 6.35: Time averaged normalised concentration of the primary jet at *x/D* =6, for a) λ=0.55, b) λ=1.4, c) λ=2.8, d) λ=3.6, e) λ=∞. The white arrows highlight the deviation of the secondary jets from their geometric axis when λ=0.55.

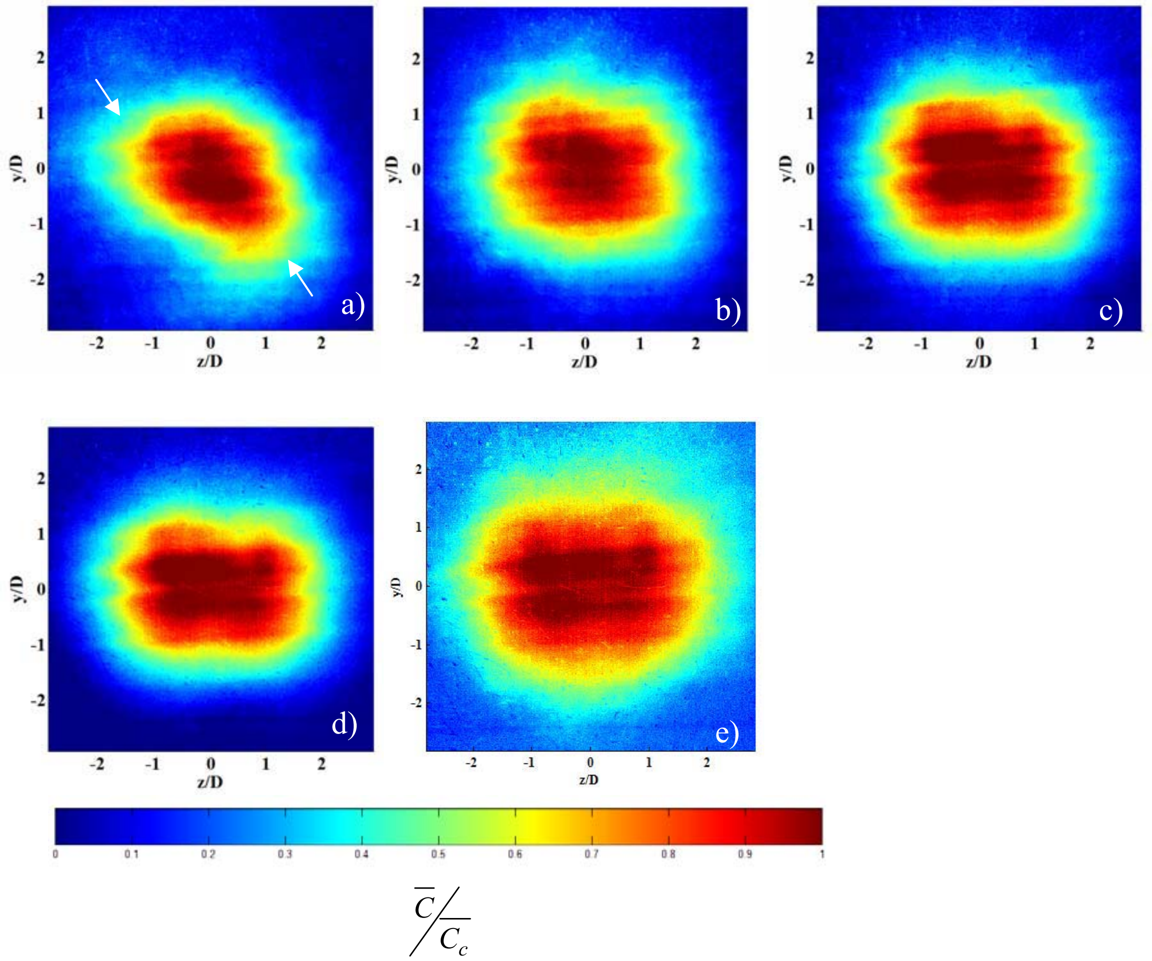

Figure 6.36: Time averaged normalised concentration of the primary jet at x/D =8, for a) λ=0.55, b) λ=1.4, c) λ=2.8, d) λ=3.6, e) λ=∞. The white arrows highlight the deviation of the secondary jets from their geometric axis when λ=0.55.

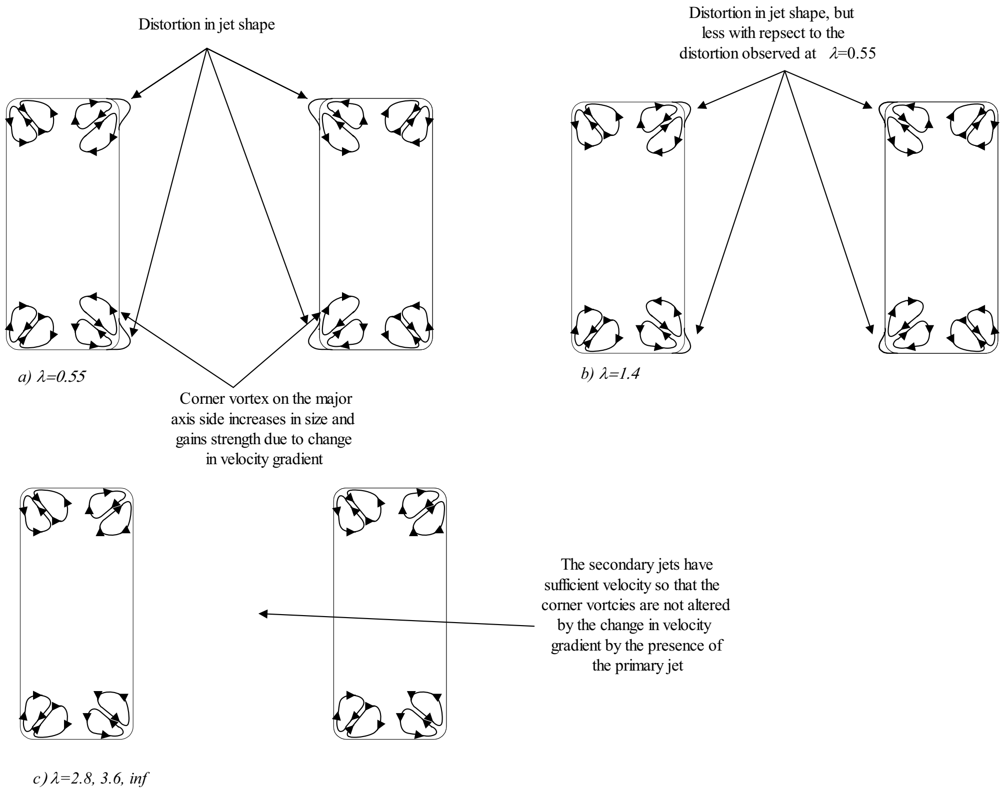

Figure 6.37: Sketch of the progressive development with λ of the coherent corner vortices on the secondary jet for λ= 0.55, 1.4, 2.8, 3.6 and ∞, x/D=0.1.

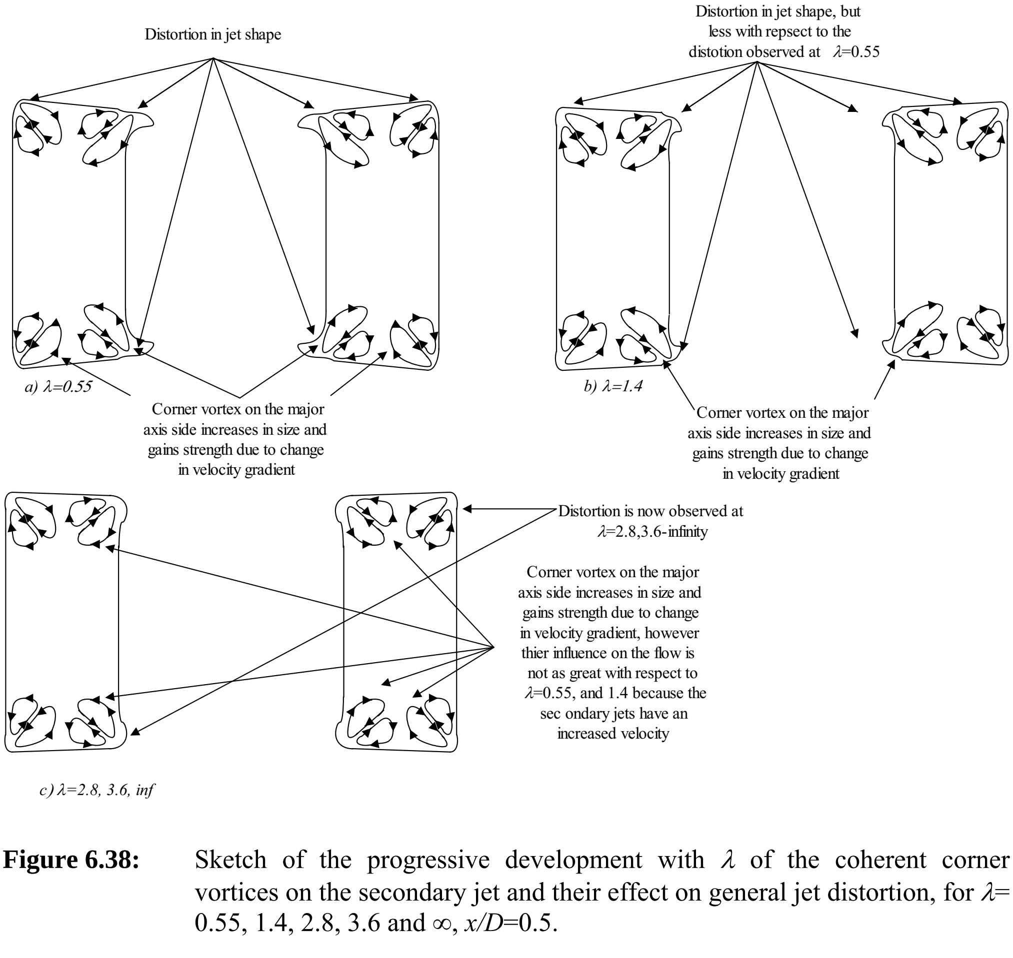

Figure 6.38: Sketch of the progressive development with λ of the coherent corner vortices on the secondary jet and their effect on general jet distortion, for λ= 0.55, 1.4, 2.8, 3.6 and ∞, x/D=0.5.

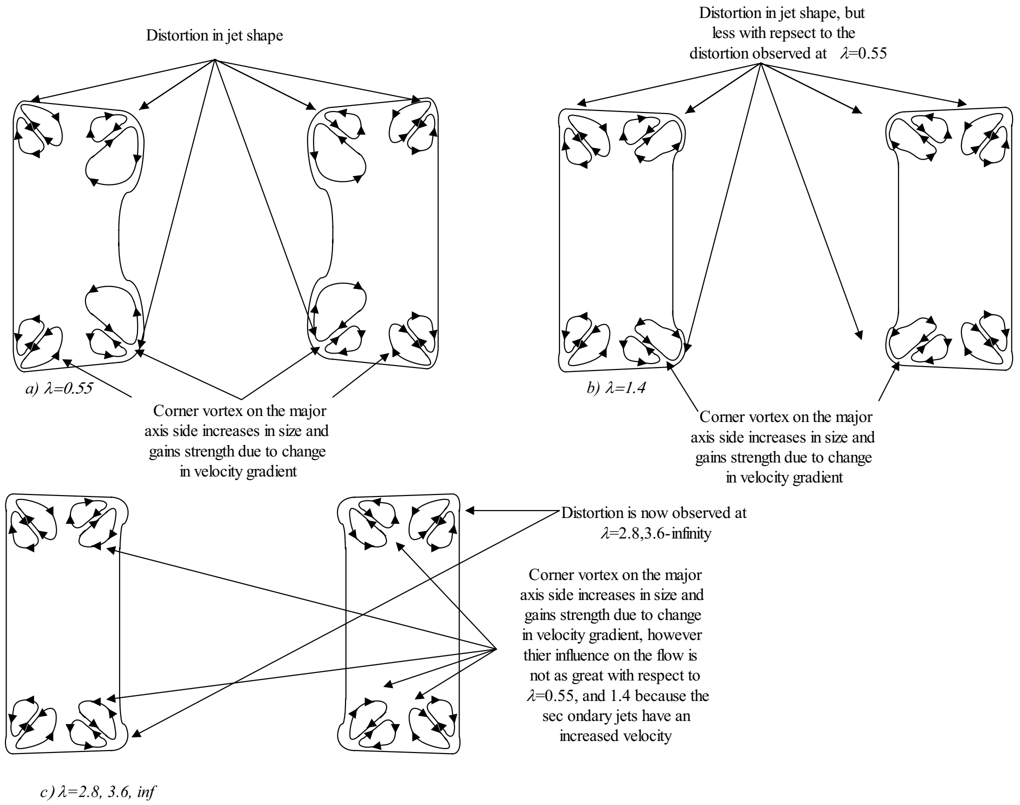

Figure 6.39: Sketch of the progressive development with λ of the coherent corner vortices on the secondary jet their effect on general jet distortion, for λ= 0.55, 1.4, 2.8, 3.6 and ∞, *x/D*=1.

6.3.2.2 Secondary Fluid Mixture Fraction on the Jet Axis

The inverse mixture fraction on the centerline of the secondary jets is shown in Figure 6.40. It reaches self-similarity at approximately *x/D* =2 regardless of the flow conditions. The higher velocity and momentum of the primary jet at λ=0.55 results in greater dilution of the secondary jet for *x/D* >2 due to entrainment of the ambient fluid by the primary jet. Values of the decay constant K_1 calculated form the linear portion of Figure 6.40 are shown Figure 6.41 versus the inverse velocity ratio and tabulated Table 6.3. For λ=0.55 K_1 has the lowest value of all the cases, due to the greater dilution of the secondary jet. For λ=1.4 to λ=3.6 the values of K_1 progressively decrease from 10.85 to 7.46. In comparison, the absence of the primary jet (λ=∞) decreases the rate of dilution, (K_1 = 11.70).

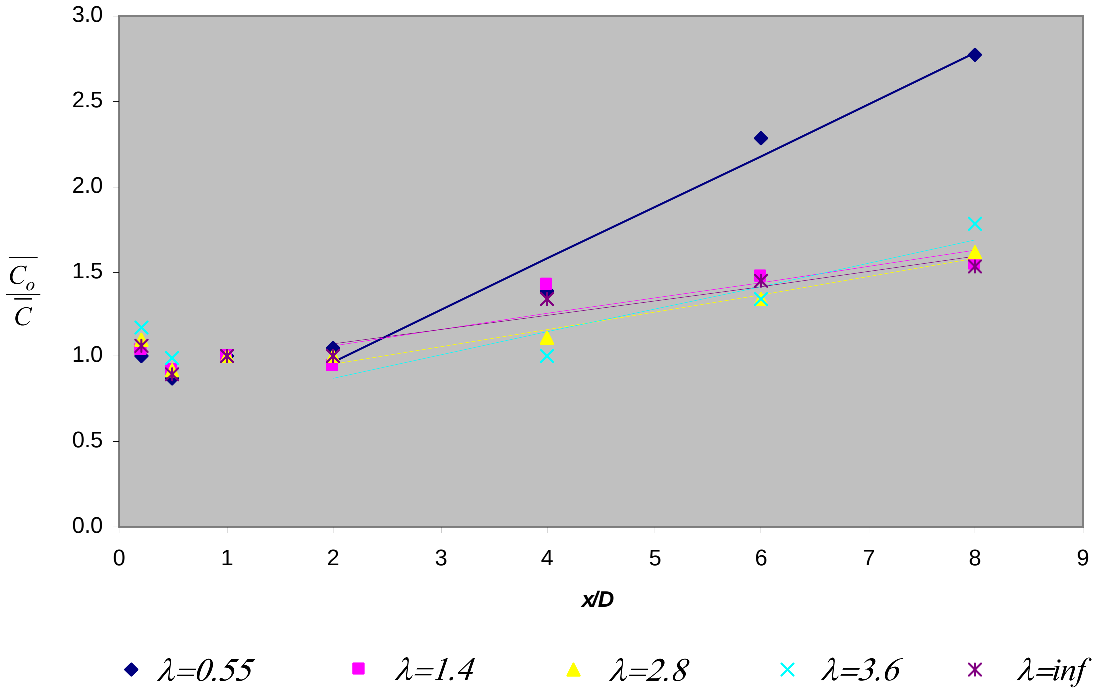

Figure 6.40 Inverse centreline mixture fraction versus dimensionless axial distance for the secondary jet at velocity ratios of λ=0.55, 1.4, 2.8, 3.6 and ∞. The straight lines represent the linear fits in the self-similar region.

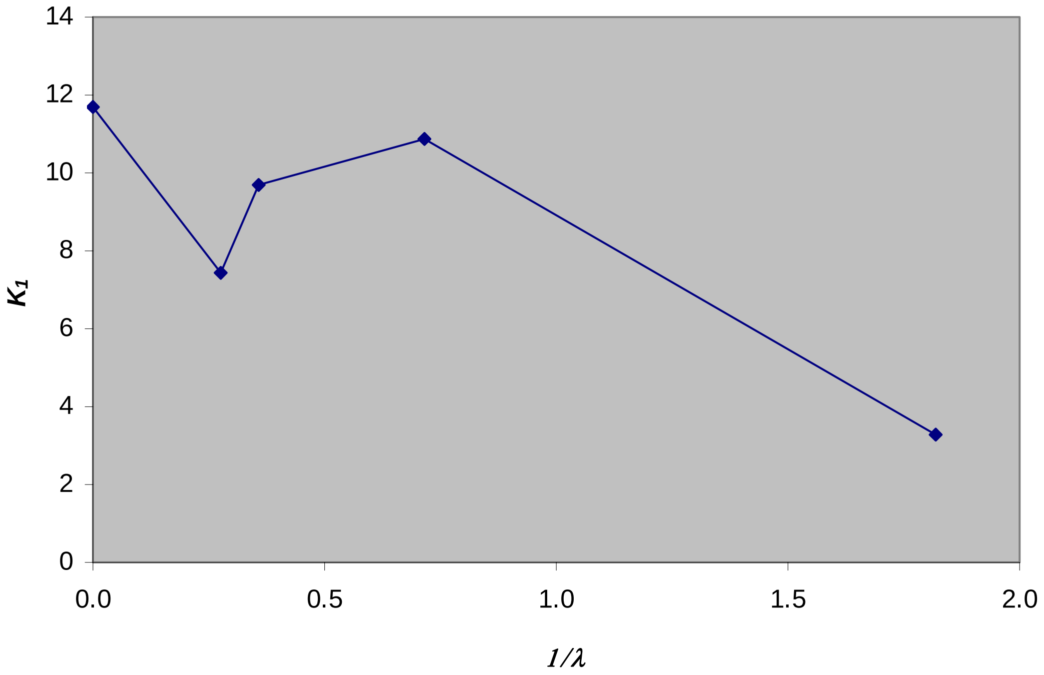

Figure 6.41: Correlation between K_1 of the secondary and the secondary to primary velocity ratio.

λ	K_1	x_{01}/D
0.55	3.30	1.18
1.4	10.85	9.57
2.8	9.71	7.27
3.6	7.46	4.53
∞	11.70	10.54

Table 6.3: Calculated values of the Centreline decay constant K_1 and the primary virtual origin of the secondary jet as a function of velocity ratio.

6.3.2.3 Secondary Jet Cross Stream Mixture Fraction

Figures 6.42 to 6.46 show the normalised concentrations of the secondary jet versus *y/D* at different values of *z/D* at axial stations *x/D* =0.1, 0.2, 0.5, 2 and 4 respectively and velocity ratios of λ=0.55, 1.4, 2.8, 3.6 and ∞. Similarly, Figures 6.48 to 6.50 show the normalised concentrations of the secondary jet versus *z/D* at different values of *y/D* at axial stations of *x/D* =4, 6 and 8.

The effect of corner structures identified in section 6.3.2.1 on the concentration is highlighted with black arrows in Figures 6.42, 6.43 and 6.44. In Figures 6.39 a) – d) there is significant evidence to suggest that at *x/D* =0.1 the coherent corner vortices are present at velocity ratios of λ= 1.4, 2.8 and 3.6. At *x/D* =0.2 peaks corresponding to the presence of coherent vortices appear only at λ=0.55 and λ=1.4. At *x/D* =0.5 in Figure 6.44 the presence of the coherent structure is only present at $\lambda=0.55$. The higher co-flowing conditions affect the concentration gradient of the primary jet in the *y*-direction at *x/D* =2 and *x/D* =4 in Figures 6.45 and 6.46. Figure 6.47 is a plot of the dimensionless concentration gradient versus $1/\lambda$, at *x/D* =2 and 4, distinctly shows that there is an increase in concentration gradient with higher velocity ratios.

Normalised concentration profiles through planes parallel to the minor axis (*y*-direction) illustrates how the co-flowing conditions may affect the merging of the two secondary jets. At *x/D* =4, λ= ∞, the black arrows (Figures 6.48e) highlight the secondary jets as they start to merge. At λ=∞ without, the presence of the primary jet, the secondary jets show a greater tendency to merge than for other λ. At *x/D* =6 (Figures 6.49) the black arrows highlight the merging of the secondary jets, illustrating how at λ=0.55 the secondary jets appear to be fully merged. At *x/D* =8 (Figures 6.50) the secondary jets appear to be merged for all cases.

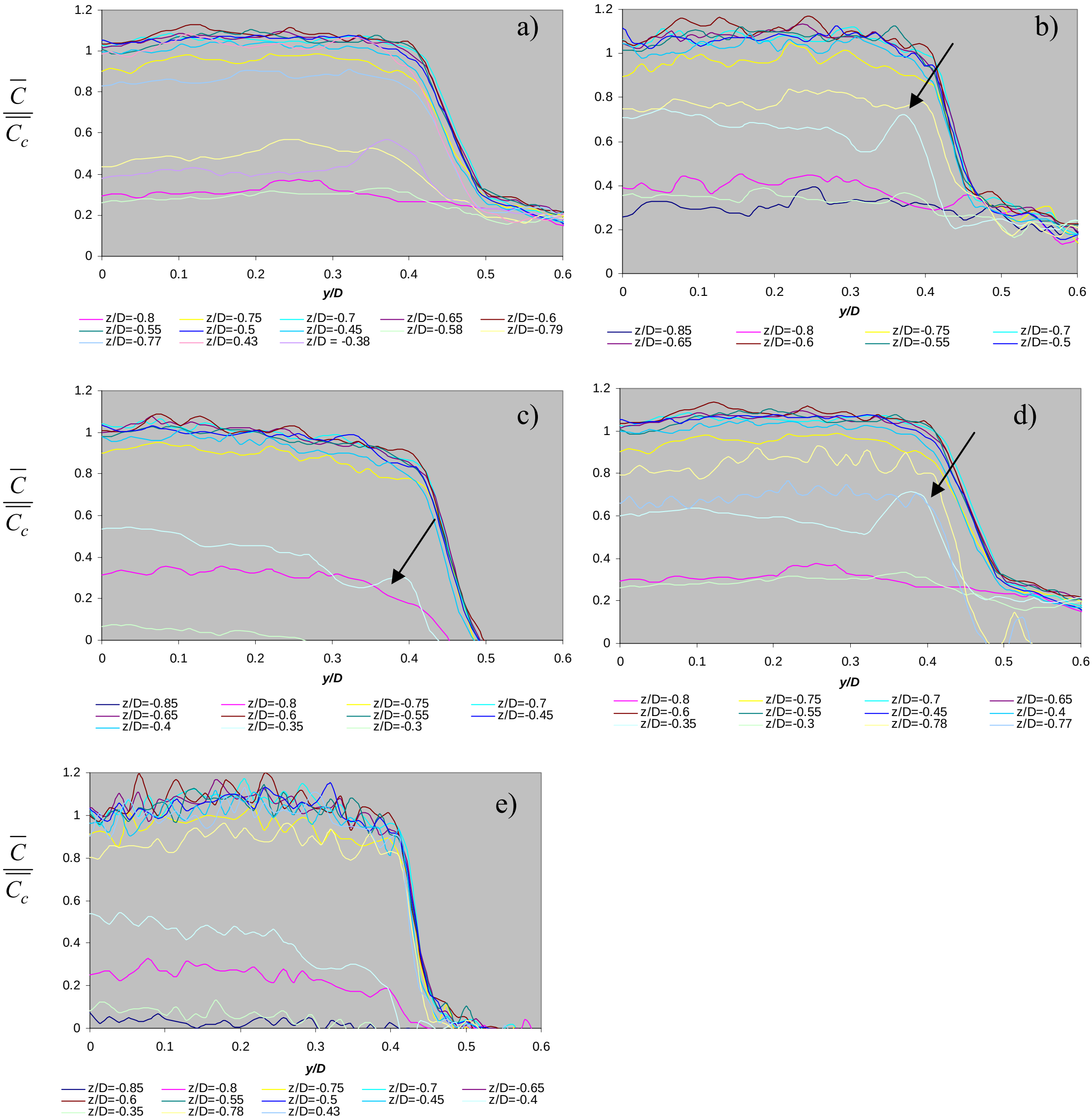

Figure 6.42: Normalised Concentration of the secondary jet versus *y/D* through different *z/D* planes, at *x/D* =0.1, a) λ=0.55, b) λ=1.4, c) λ=2.8, d) λ=3.6, e) λ=∞. The black arrows highlight the peaks corresponding, to the coherent corner vortices in close proximity to the corners of the secondary jet.

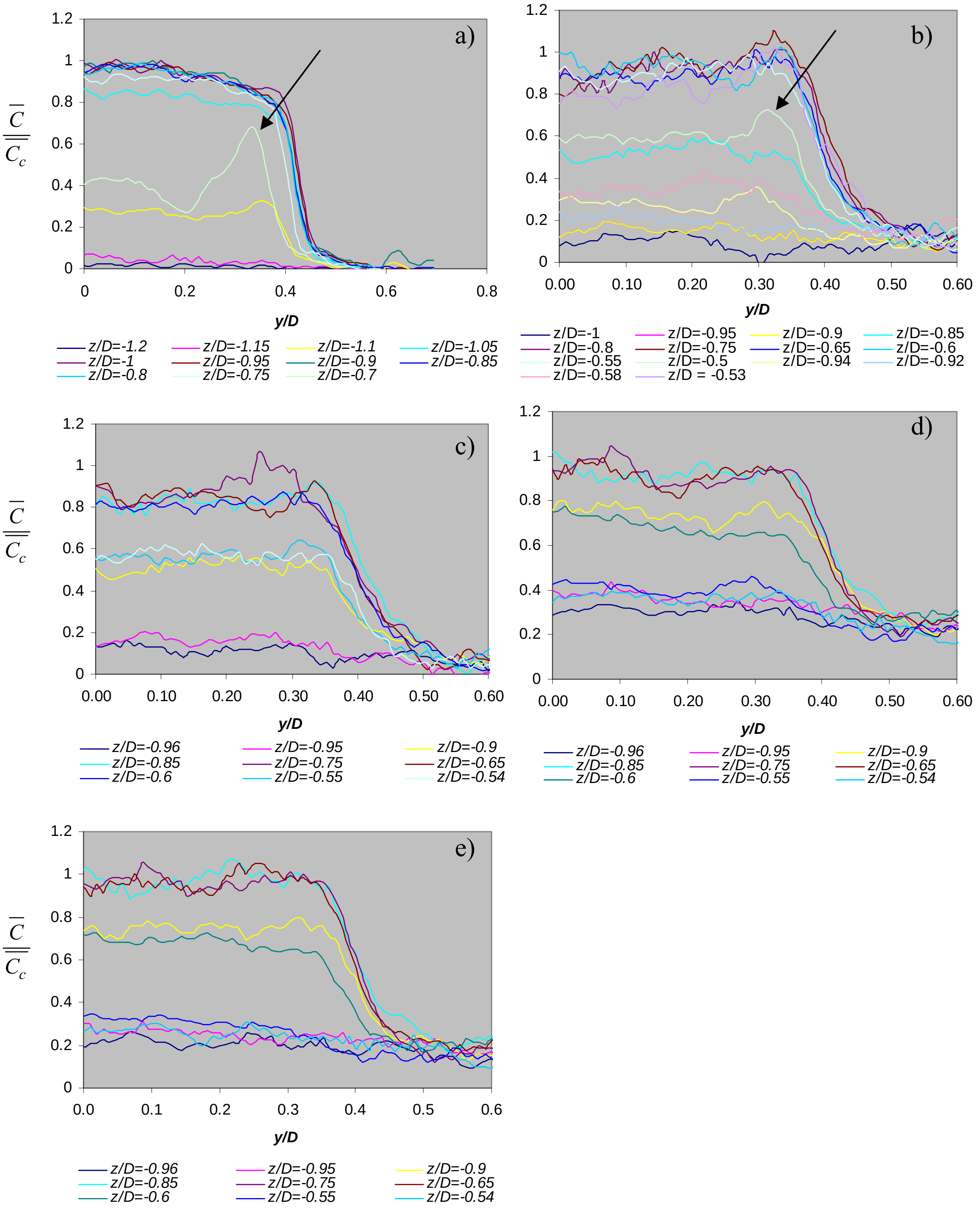

Figure 6.43: Normalised Concentration of the secondary jet versus *y/D* through different *z/D* planes, at *x/D* =0.2, a) λ=0.55, b) λ=1.4, c) λ=2.8, d) λ=3.6, e) λ=∞. The black arrows highlight the peaks corresponding, to the coherent corner vortices of fluid in close proximity to the corners of the secondary jet.

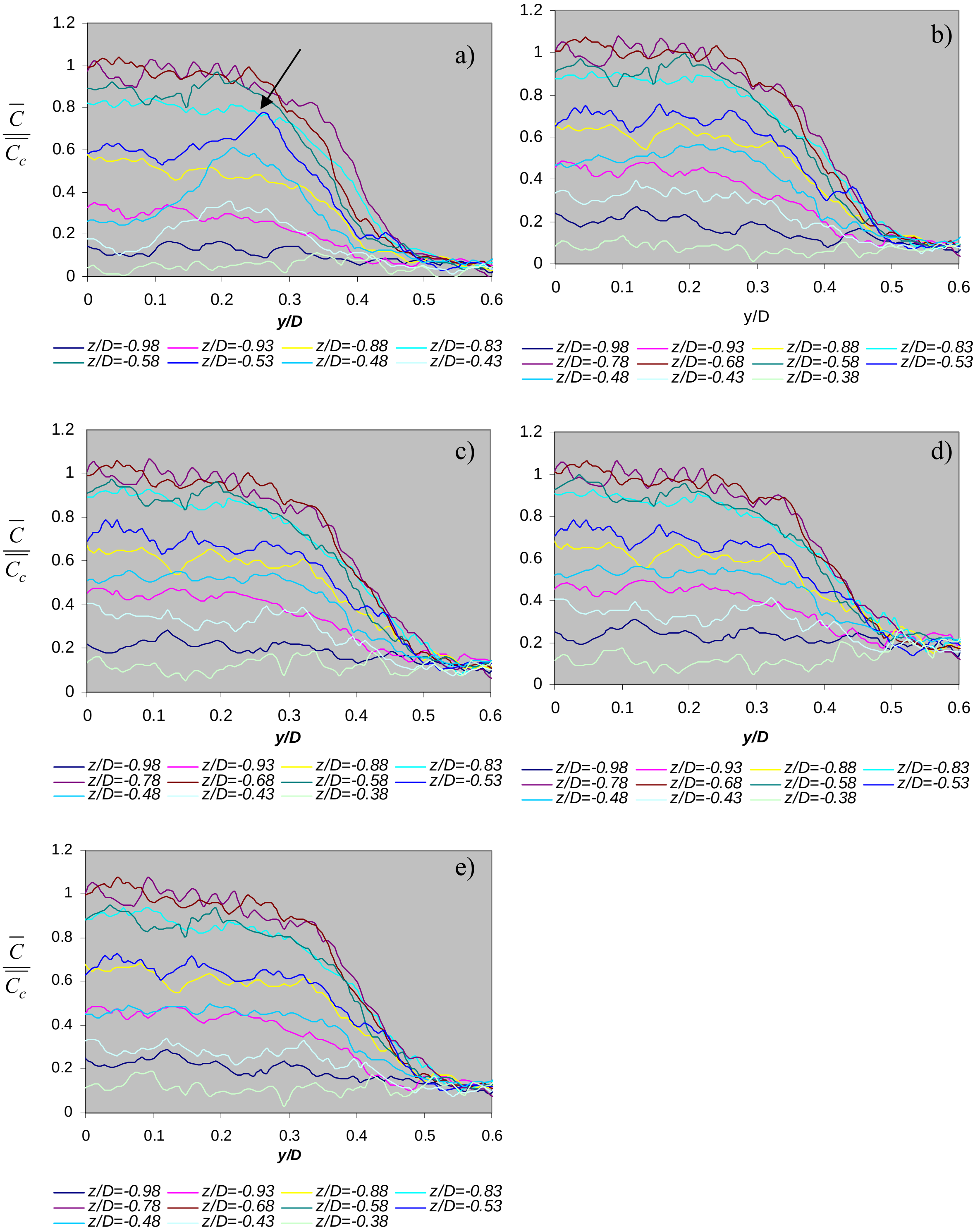

Figure 6.44: Normalised Concentration of the secondary jet versus *z/D* through different *y/D* planes, at *x/D* =0.5, a) λ=0.55, b) λ=1.4, c) λ=2.8, d) λ=3.6, e) $\lambda=\infty$. The black arrow highlights the peak corresponding, to the coherent corner vortex in close proximity to the corners of the secondary jet.

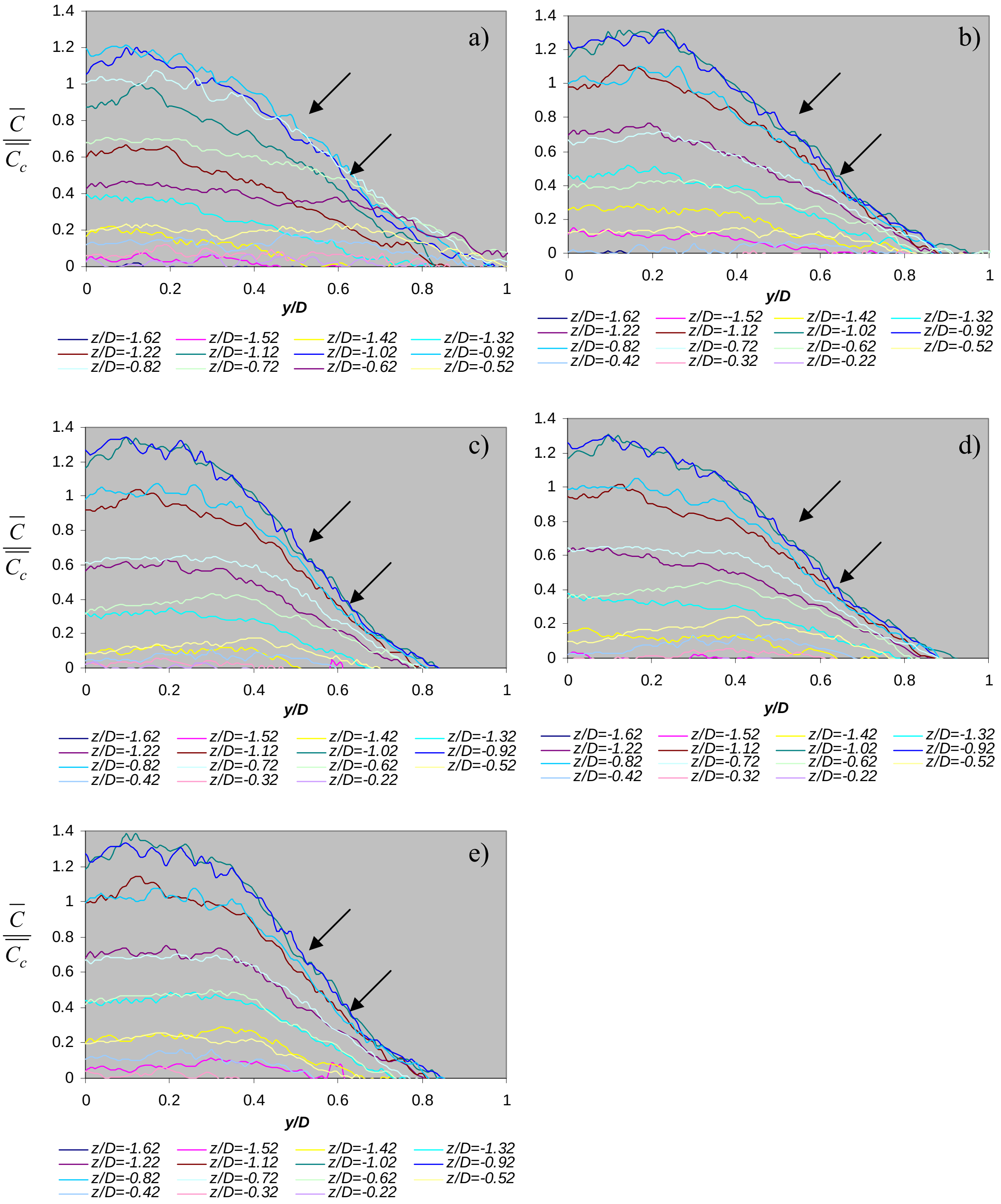

Figure 6.45: Normalised Concentration of the secondary jet versus *y/D* through different *z/D* planes, at *x/D* =2, a) λ=0.55, b) λ=1.4, c) λ=2.8, d) λ=3.6, e) λ=∞. The black arrows outline a progressive increase in concentration gradient with an increase in co-flowing conditions.

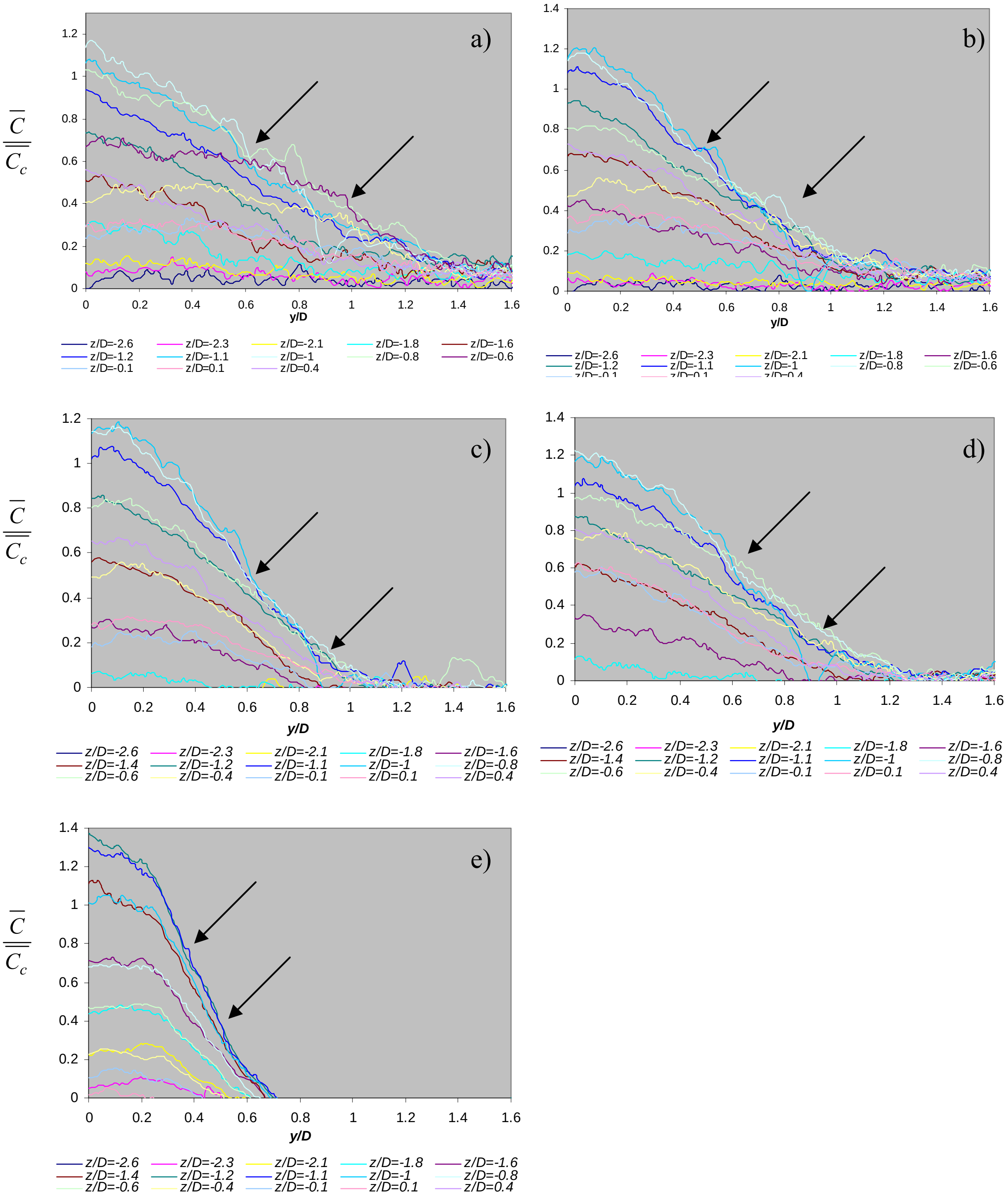

Figure 6.46: Normalised Concentration of the secondary jet versus *y/D* through different *z/D* planes, at *x/D* =4, a) λ=0.55, b) λ=1.4, c) λ=2.8, d) λ=3.6, e) λ=∞. The black arrows outline a progressive increase in concentration gradient with an increase in co-flowing conditions.

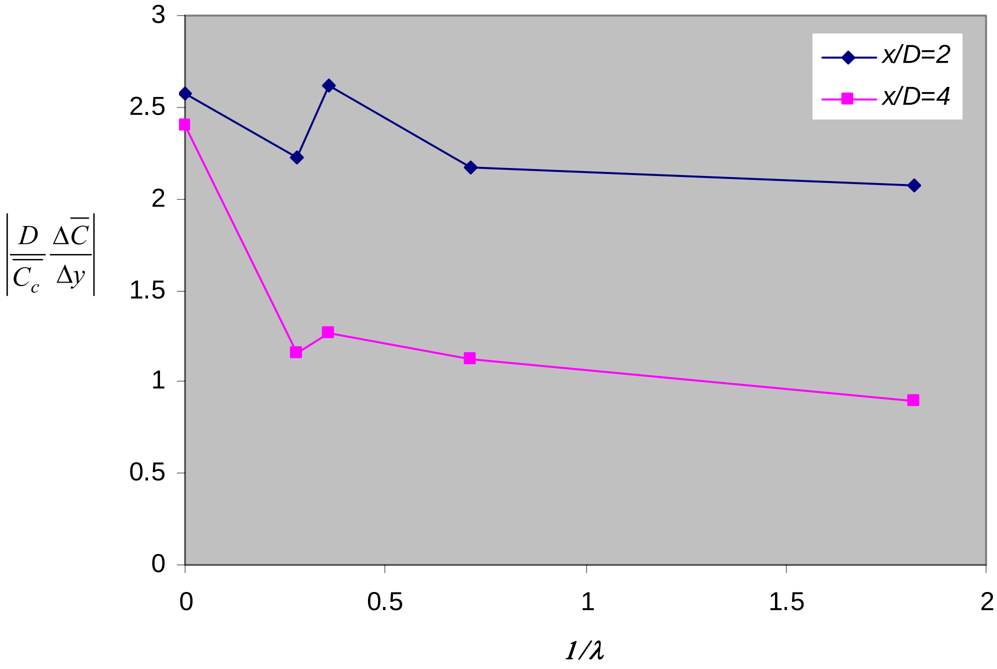

Figure 6.47: Absolute value of the dimensionless concentration gradient in the *y*-direction versus velocity ratio of the secondary jet, for *z/D* =0.

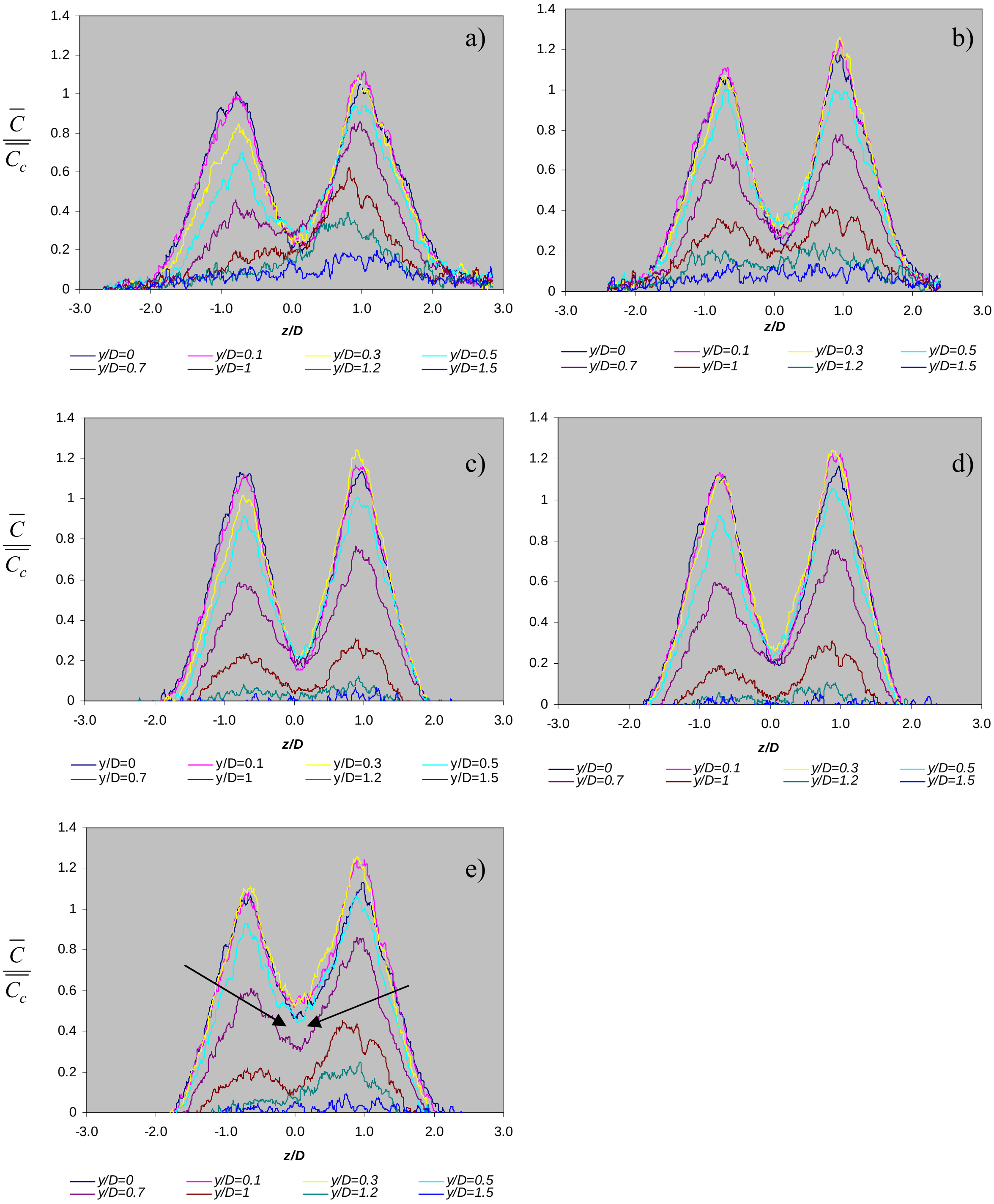

Figure 6.48: Normalised Concentration of the secondary jet versus *z/D* through different *y/D* planes, at *x/D* =4, a) λ=0.55, b) λ=1.4, c) λ=2.8, d) λ=3.6, e) $\lambda=\infty$. The black arrows highlight a favoured merging between the two jets for $\lambda=\infty$.

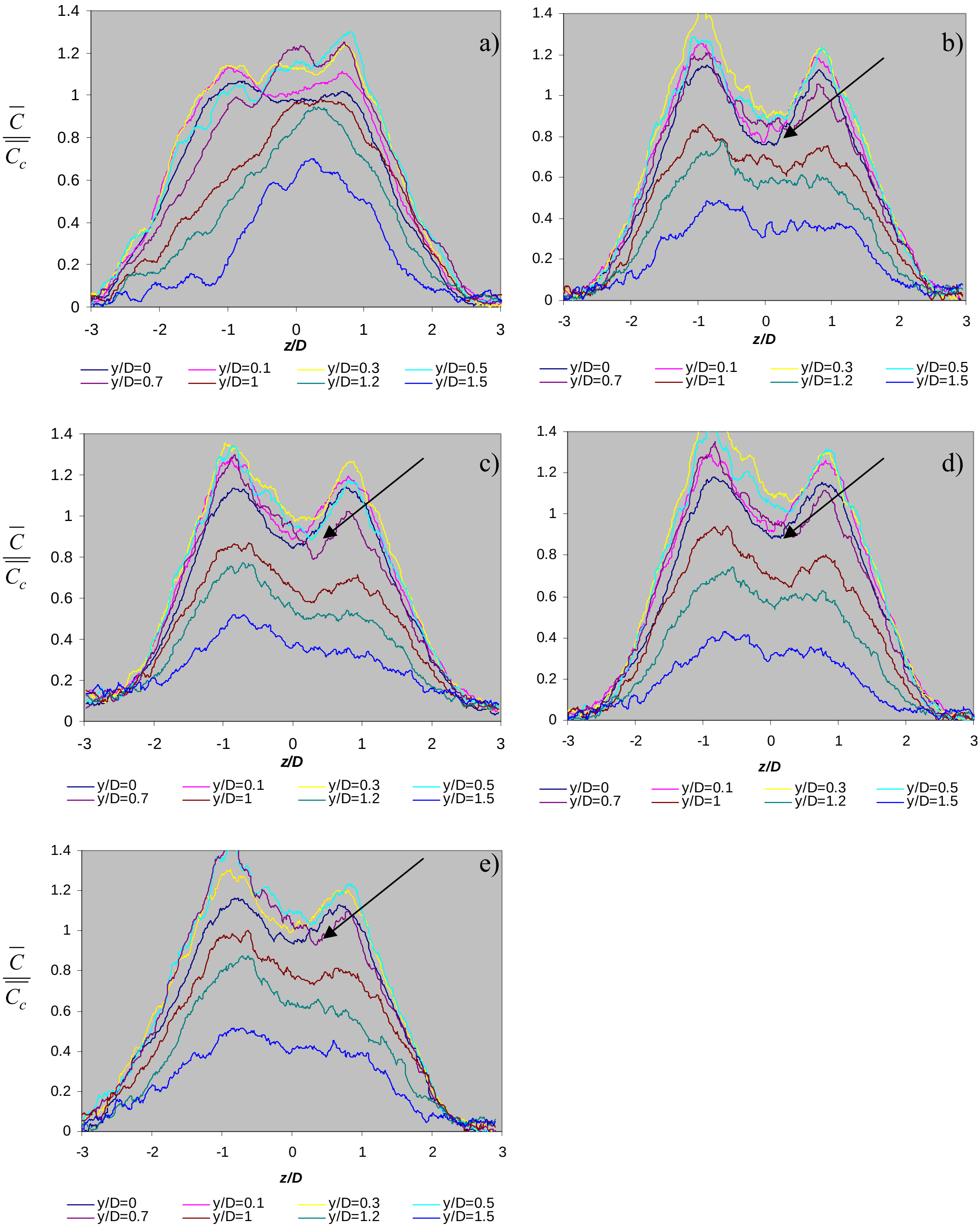

Figure 6.49: Normalised Concentration of the secondary jet versus *z/D* through different *y/D* planes, at *x/D* =6, a) λ=0.55, b) λ=1.4, c) λ=2.8, d) λ=3.6, e) λ=∞. The black arrows highlight the merging point between the two jets for λ=1.4, λ=2.8, λ=3.6, and λ=∞.

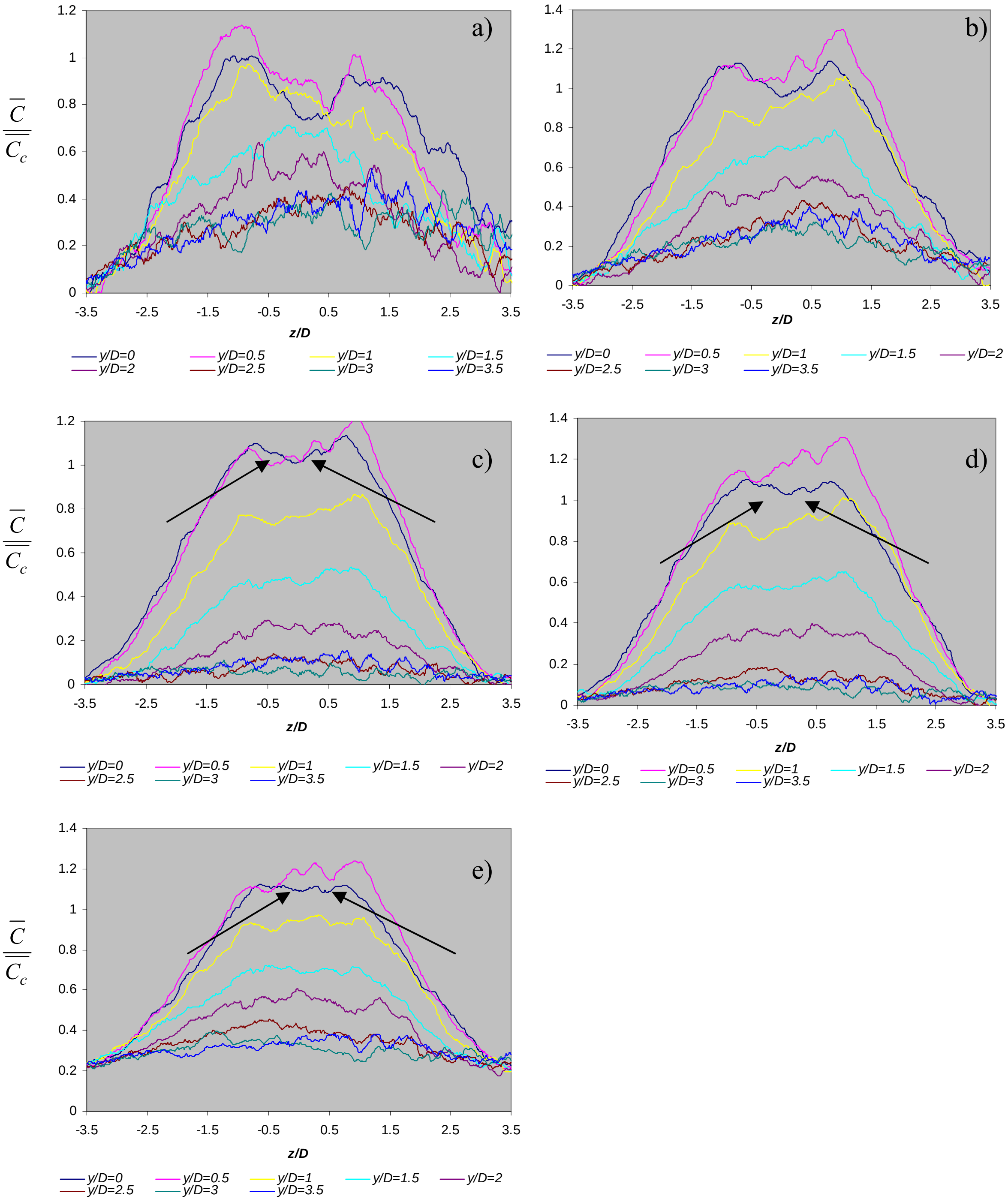

Figure 6.50: Normalised Concentration of the secondary jet versus *z/D* through different *y/D* planes, at *x/D* =8, a) λ=0.55, b) λ=1.4, c) λ=2.8, d) λ=3.6, e) $\lambda=\infty$. The black arrows highlight the merged jets for λ=2.8, λ=3.6, and $\lambda=\infty$.

6.3.2.4 Discussion

As for the primary jet, the secondary jets possess a pair of counter-rotating corner vortices, which are heavily affected by the local velocity gradients. Lower velocity ratios reveal that the primary jet exerts a change in velocity gradient, which cause not only the vortices on the primary jet side but also those on opposite corners to change in size and strength causing jet distortion. The centreline mixture fraction of the primary jet reaches self-similarity at $x/D = 4$, whereas the analysis of the data in Section 6.3.2.2 reveals that the secondary jets are self-similar for $x/D > 2$. Sfier (1976) and Sforza and Stasi (1979) who investigated the centerline decay of a passive scalar of a range of rectangular jets of different aspect ratios, found that lower aspect ratio jets reach self similarity before higher aspect ratios. This general conclusion can be also drawn from Sfier (1979) and Krothpalli *et al*., (1981) who focused on the centerline decay of velocity rather than passive scalars. There is also evidence that jet to jet interaction alters the individual structures of the secondary jets, even at $\lambda = \infty$, altering the concentration profiles in the x-direction.

The converging and merging regions established by Lin and Sheu (1991) for multiple parallel rectangular jets are applicable to this study. The time averaged images in Section 6.3.2.1 reveal that the presence of the primary jet retards merging between the secondary jets. The momentum of the primary jet is sufficient to retard merging of the secondary jets, in a similar fashion to the penetration of the primary jet through the re-circulation region of a co-annular jet. Merging of the secondary jets is also facilitated by higher λ, for instance at λ=2.8 and 3.6 the high appetite for entrainment of the secondary jets facilitates their interaction.

6.3.3 Axis Switching

Axis switching is a result of the faster growth rate of the jet's shear layers in the minor axis plane compared to those in the major axis plane. Factors influencing axis switching are upstream geometry, nozzle shape at the exit plane and aspect ratio. Comparison of the work of Gutmark and Grinstein (1999) Sfeir (1976) Krothpalli *et al*., (1981) Sforza *et al*., (1966) by Gutmark and Grinstein (1999) reveals that the axial position of the cross over points are proportional to the aspect ratio, AR (complete data set in Figure 6.53);

$$X_c \propto AR$$ **Equation 6.3**

Although Equation 6.3 identifies the aspect ratio as the major contributing factor to the location of crossover, the effect of upstream geometry should not be neglected. Tsuchyia *et al.*, (1986) observed that axis switching varied between 1 and 25 diameters downstream for rectangular jets issuing from an orifice with aspect ratio varying between 1 < AR < 5. Quinn (1992) located the cross over point from *x/D* = 1 to 20 for rectangular jets issuing from a contoured nozzle having aspect ratios between 1 and 20. After the first axis switch the original major axis side grows at a faster rate than the minor side resulting in a second axis switch. The location of the second axis switching is much less sensitive to aspect ratio (Gutmark and Grinstein, 1992). No measurements have been made to date on the effect of co-flowing streams on the position of axis switching in rectangular jets.

Figures 6.51 shows the dimensionless widths (*z/D*) and heights (*y/D*) of the primary jet as a function of axial distance (*x/D*) at velocity ratios λ=0 to 3.6. Similarly, Figure 6.52 shows the dimensionless widths and heights versus *x/D* of a secondary jet at velocity ratios λ=0.55 to ∞. The jet width and height is representative of the progressive downstream expansion of the minor and major axes. The numerical values of *W* and *H* were measured using the 'edge' function in the Matlab image processing toolbox (2004) on the planar time averaged images in Sections 6.3.1.1 and 6.3.2.1. The edge function is programmed to look for the local maxima of the gradient in the time-averaged image. The gradient is calculated using the derivative of a Gaussian filter. The method uses two thresholds, to detect strong and weak edges.

The axis switching of the primary jet at λ=0, shown in Figure 6.51a) occurs at *x/D* = 5.6. The presence of the secondary stream at λ=0.55 moves the point of axis switching to *x/D* =5. For λ=1.4 (Figure 6.51c) the jet switches axes twice at *x/D* = 4.8 and 6.7, similarly at λ=2.8 (Figure 6.51d) the jet switches at *x/D* = 4.8 and 6.5. However, at λ=3.6 axis switching is not observed at all. There is evidence that the presence of the secondary flow, for λ=0.55 to 2.8, controls the cross-over point of the major and minor sides. The observations from the time averaged planar data of the primary jet (Sections 6.3.1.1) conclude that there is a forced shortening of the primary jet in the *y*-direction (height) between 1 < *x/D* < 4.

Using the data retrieved from the literature and shown in Figure 6.53, a linear model was applied to the data of Gutmark and Grinstein, (1999) Sfeir, (1976) Krothpalli *et al*., (1981) and Sforza *et al*., (1966). All the data-sets have similar slopes ranging from 3.1 to 4 but with quite different intercepts. The only comparable point of axis switching in the current data to the values in the literature was for λ=0 at x_c/D = 5.6 because it is not influenced by a co-flowing stream. The extended linear models from the literature data revealed that for a rectangular jet with AR = 1.2, only the data of Krothpalli *et al*., (1981) delivers a comparable cross over point at x_c/D =5.1.

The dimensionless widths and heights of the secondary jets, shown in Figure 6.52 for λ=0.55 to ∞ show no apparent cross over in the region between $0 < x/D < 4$. It is not feasible to compare cross-over points of the secondary jet with the data in Figure 6.53, as the secondary jets always operate in a multiple jet arrangement, unlike the primary jet at λ=0.

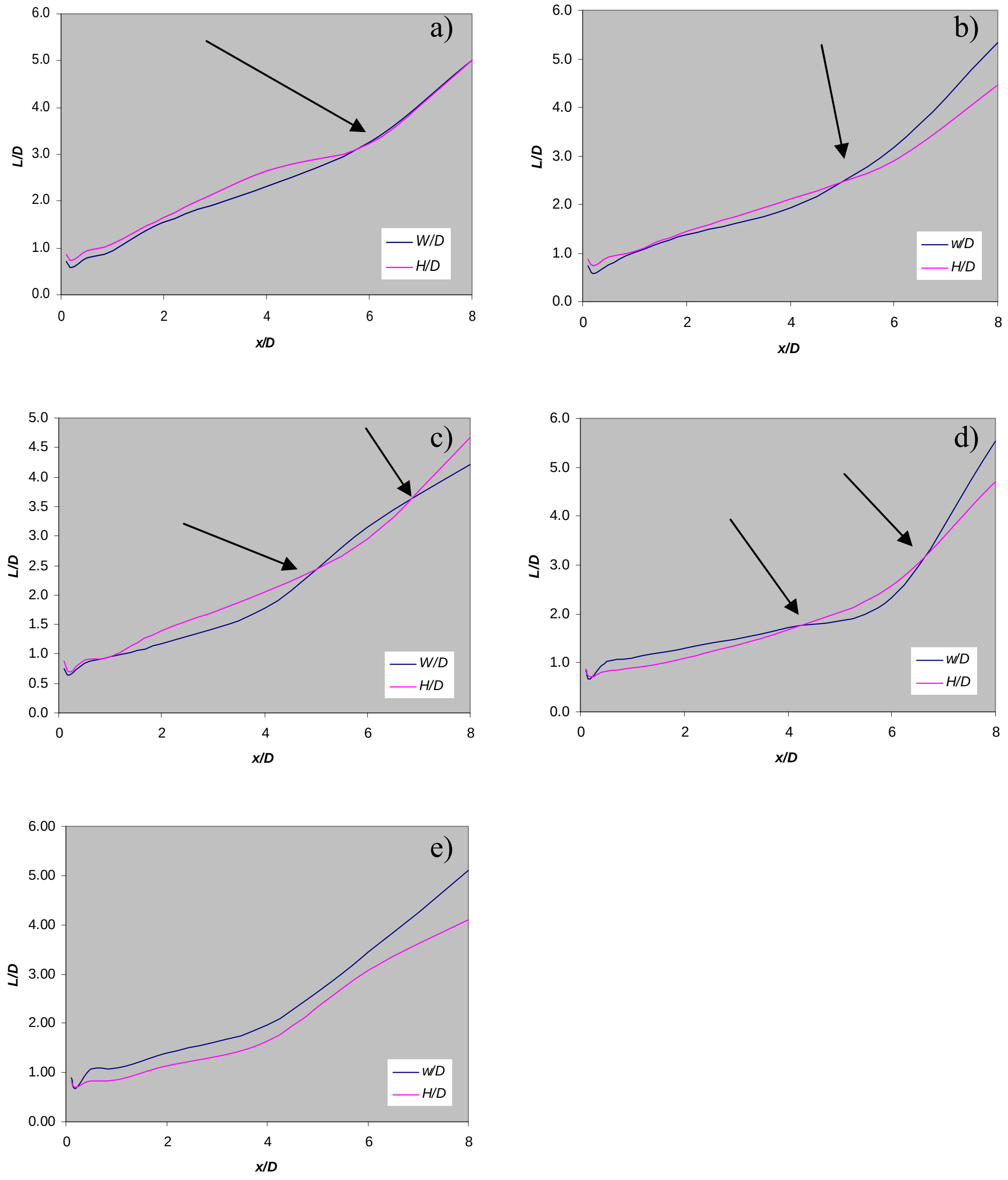

Figure 6.51: Normalised lengths of the major and minor axis sides of the primary jet as a function of downstream distance, *x/D*, a) λ =0, b) λ =0.55, c) λ =1.4, d) λ =2.8, e), λ =3.6. The black arrows show positions of axis switching.

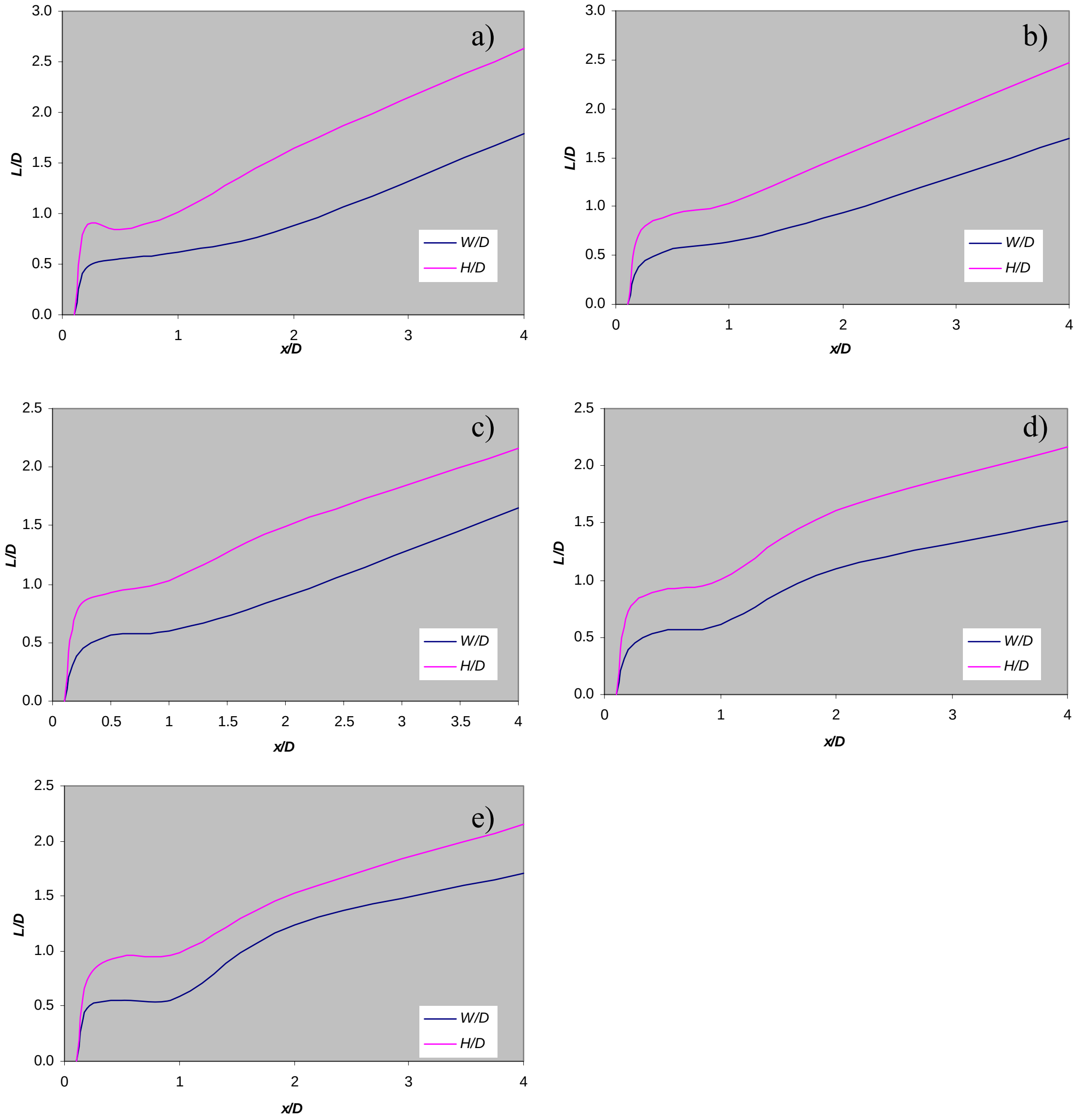

Figure 6.52: Normalised lengths of the major and minor axis sides of the secondary jet as a function of downstream distance, *x/D*, a) λ =0, b) λ =0.55, c) λ =1.4, d) λ =2.8, e), λ =3.6.

NOTE: This figure is included on page 218 of the print copy of the thesis held in the University of Adelaide Library.

Figure 6.53: Point of cross-over between the major and minor axis lengths versus aspect ratio various rectangular jets, illustrating the strong linear correlation between the first point of axis switching and jet aspect ratio (Gutmark and Grinstein, 1999).

6.3.4 Bulk Entrainment

The amount of fluid entrained in a moving jet is usually assessed by plotting the relative mass flow rate of a jet (m/m_0) versus x/D. Knowledge of the relationship of the relative mass flow is important in combustion modelling, for instance, Jenkins and Moles (1981; 1988) successfully used the relative mass flow rate developed by Ricou and Spalding (1963) for enclosed round jet flames for combustion modelling in rotary kilns.

$$\frac{m}{m_0} = C_E \frac{x}{D} + 1$$ **Equation 6.4**

where C_E is the entrainment coefficient. In order to determine the relative mass flow of the primary/secondary jet system it is necessary to calculate the mean mixture fraction within the time averaged jet flow. Several methods measure the mass flow rate of jets, the first was the entrainment shroud of Ricou and Spalding (1961) more recently it has been directly measured using PIV by Han and Mungal (2001). Using a specified window of the time averaged mixture fraction of WxH dimensions consisting of a total of *I*x*J* pixels, the bulk mixture fraction is determined as;

$$\overline{\xi_B} = \frac{1}{IxJ}\sum_{1}^{I}\sum_{1}^{J}\overline{\xi_{i,j}}$$ **Equation 6.5**

As for Section 6.3.3 the numerical values of *W* and *H* were measured using the ‘edge’ function in the Matlab image processing toolbox (Mathworks, 2004) on the planar time averaged images in Sections 6.3.1.1 and 6.3.2.1. For λ=0.55, 1.4, 2.8 and 3.6 where there are two streams flowing at once, the total bulk mixture fraction is the sum of the primary and secondary jet bulk mixture fractions;

$$\overline{\xi_{TB}} = \overline{\xi_{PB}} + \overline{\xi_{SB}}$$ **Equation 6.6**

In jet flow like any other flow, mass is conserved;

$$\frac{\dot{m}}{\dot{m}_o} = \frac{1}{\overline{\xi_{TB}}}$$ **Equation 6.7**

where $\dot{m}$ is the mass flow of a jet system at a downstream distance *x/D*, $\dot{m}_o$ the mass flow rate at the nozzle exit plane. Figure 6.54 is the relative bulk-entrainment of the combined primary and secondary rectangular jets for λ=0, 0.55, 1.4, 2.8, 3.6 and ∞ as well as a direct comparison to a round turbulent pipe jet (Ricou and Spalding, 1961). However, for the case when λ=0 and ∞ higher relative rates of entrainment are observed. It may be possible that smaller relative rates of bulk-entrainment of ambient fluid, observed for the cases when all jets are operating, is due to entrainment of the lower momentum jet by the higher momentum jet at the expense of ambient fluid. The entrainment mechanism has been explained in Chapter 2 and Section 4.1. The entrainment coefficient used by Ricou and Spalding (1961) and examined in more detail by Hill (1972) was calculated by measuring the slope of the linear region of data in Figure 6.54. Figure 6.55 reports the entrainment coefficient versus velocity ratio for the primary and secondary jets under different co-flowing conditions, and shows how the presence of the secondary jet from λ= 0 to λ=0.55 causes the entrainment coefficient to drop from 1.19 to 0.58, and remain more or less constant thereafter.

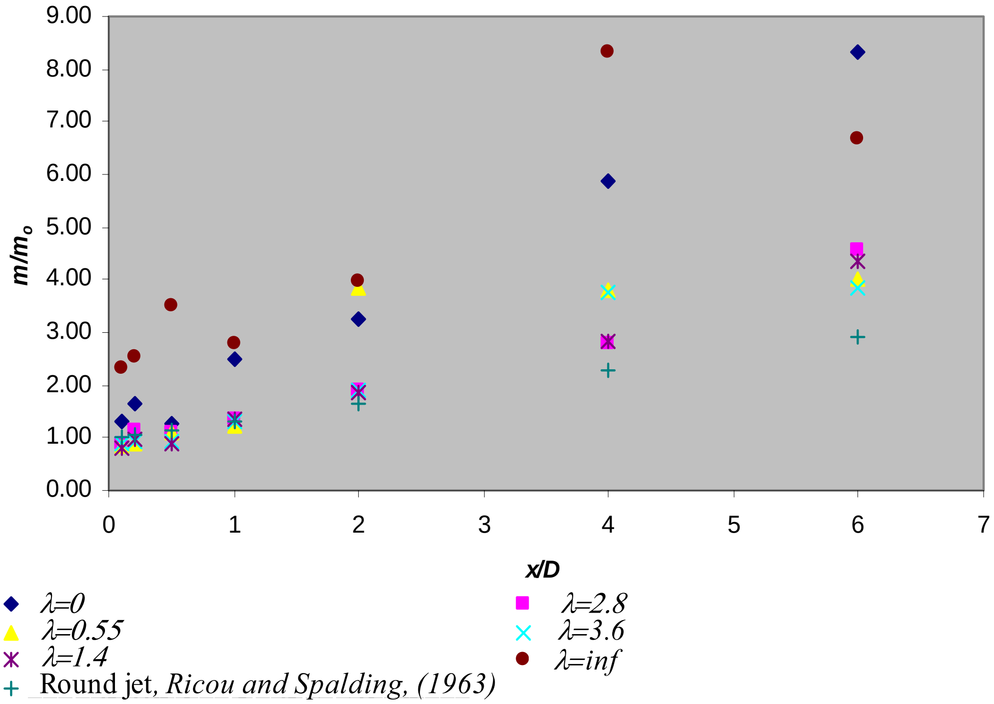

Figure 6.54: Relative entrainment ratio of the primary/secondary jet versus axial distance *x/D* system for λ=0, 0.55, 1.4, 2.8, 3.6, ∞ and round pipe jet (Ricou and Spalding, 1963).

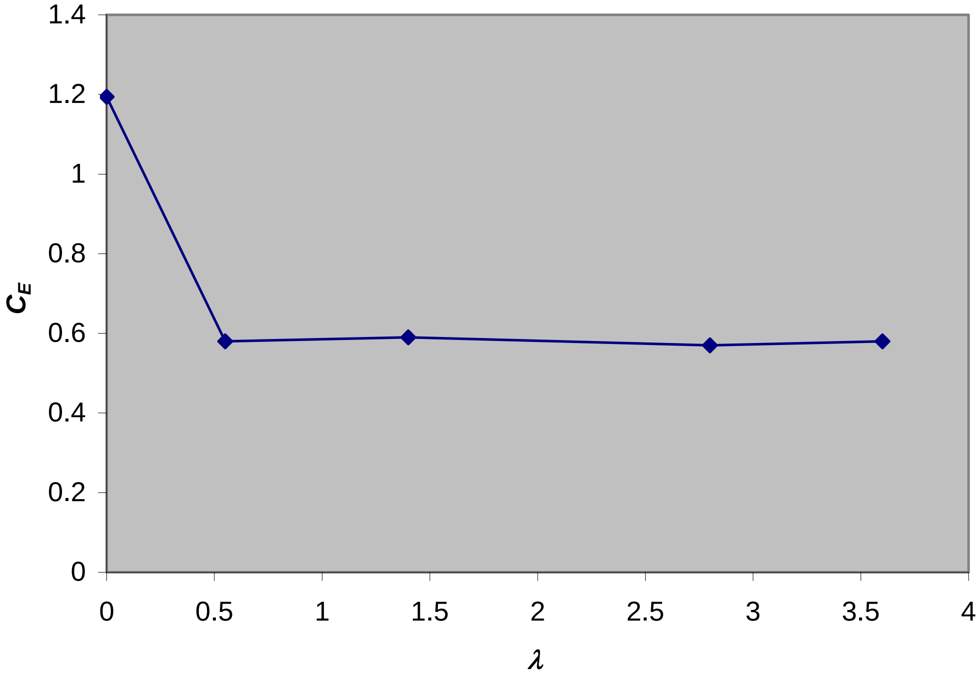

Figure 6.55: Entrainment coefficient of the primary/secondary jet system versus velocity ratio.

6.4 Conclusion

Time averaged images in Section 6.3.1.1 reveal that large-scale deformations of the primary jet occur between $1<x/D<4$ for $\lambda=2.8$ with respect to the primary jet with no co-flow ($\lambda=0$).

The driving force in the deformation from the original jet structure, be they small scale in the near field (velocity controlled), or large scale in the intermediate field (momentum controlled) is the amount of velocity or momentum exchanged between the primary and secondary jets, or the net difference. The exchange in velocity or momentum changes the local velocity gradients, hence the vorticity. This changes the nature of the counter rotating corner vortices of both the primary and secondary jets. For $\lambda>1.4$ the amount of velocity and momentum exchange is sufficient to change the nature of the corner vortices on each of the corners on the primary jet. The corner vortices of the primary expand with size at $x/D=0.5$ and cause an expansion of the jet in the z-direction before turning the primary jet into an elliptical shape at approximately $x/D=2$. This observation is consistent with contraction of the primary jet through Plane C in Section 4.4.3. The corner vortices of the secondary jets also undergo change with velocity ratio causing a significant degree of distortion. However, this is favoured by higher primary jet velocities, i.e. at $\lambda<1$.

The characteristic decay constant, K_1, of the primary jet for different λ is a quantitative measure of the dilution of primary fluid in the momentum-controlling region. As stated above the general nature of the structures of the primary and secondary jets are controlled by vorticity hence by velocity exchange. A clear dependence between K_1 and λ exists in the self similar region where supposedly mixing is controlled by momentum or momentum exchange. It is appropriate at this stage to introduce some new scaling parameters when performing low Reynolds number modelling of this type, which may achieve similar flow characteristics in full scale boilers. These parameters are based on the driving force in the near and intermediate mixing fields of co-flowing streams respectively, i.e. such as velocity and momentum difference rather than velocity and momentum ratio. Equations 6.7 and 6.8 are the modified secondary to primary velocity and momentum ratios λ' and κ'.

$$\lambda' = \frac{\overline{u_2} - \overline{u_1}}{\overline{u_1}} = \lambda - 1$$ **Equation 6.8**

$$\kappa' = \frac{\dot{m}_2 \overline{u_2} - \dot{m}_1 \overline{u_1}}{\dot{m}_1 \overline{u_1}} = \kappa - 1$$ **Equation 6.9**

Chapter 7

7 Mathematical Modelling of the Mean Scalar Mixing Field of Rectangular Jets

7.1 Introduction

Empirical models have been developed by many experimentalists to describe the mean turbulent mixing of jets. Albertson (1950) derived analytically semi-empirical relationships that predicted the volume of fluid entrained by a round jet in the near and far regions. Ricou and Spalding (1961), Hill (1972) and Wyganski and Fielder (1969) all derived one dimensional empirical relationships quantifying the amount of entrained fluid as a function of downstream distance in round turbulent jets. Wall *et al*. (1980) derived and validated semi-empirical relationships for a co-annular jet. These examples are all empirical models applied to real experimental data. However other alternatives exist such as computational fluid dynamics (CFD) for single phase flow where numerical methods are employed to solve the full set of continuity and Navier Stokes equations in turbulent form with relevant closure models. It is the nature of these closure models which determine the computational time of the model and the length scale of calculated turbulent structures. Traditionally the Eddy-stress and Reynolds stress models were used in the early periods of CFD (1970’s-1980’s) but were insensitive to small scale turbulence (Wilcox, 1998, Miller *et al*., 1995). Direct Numerical Simulation, which is the resolution of full set of Navier Stokes and continuity equations down to the turbulent structure of the smallest length scale is also used to study the properties of non-circular turbulent jets. This approach be-it highly effective, requires super-computers and long compilation times. Recently a turbulent closure model called Large Eddy Simulation (LES) has been readily used for a number of studies. For instance Grinstein *et al*., (1995) and Grinstein, (1993; 2001) used LES on simulations of turbulent square and rectangular jets, Hart (2001) and Hart *et al*., (2004) used LES on the primary/ secondary rectangular jet groups found in the Yallourn Stage 1 boilers. LES does not possess the ability to resolve the turbulent structure of the smallest length scale like DNS, but solves the continuity and Navier-Stokes equations within more acceptable time frames.

Although CFD is a very important tool in turbulence studies, it still constitutes high computation times with single-processor desktop computers and hence is unfeasible for inputs for an overall combustion model which assesses the effects of fuel change on brown coal fired boilers and is used as a preliminary design tool.

Measurements on the scalar mixing field of the round simple jet has also been performed by a number of experimentalists and reviewed in detail in Section 2.4.1. Becker *et al*. (1967) who was the pioneer of passive scalar measurement in jets, modelled the centerline concentration of the round unconfined free jet using spline regions of 1st order polynomials and modelled radial profiles using the Gaussian error curve. This type of analysis was extended to a co-annular jet by Grandmaison *et al*., (1996) and to a high aspect ratio rectangular jet by Grandmaison and Pollard, (1991). Scalar distributions of multiple co-flowing plane jets were described in a similar manner by Grandmaison and Zettler (1989) and Ng and Grandmaison (1989).

Reproduction of three dimensional scalar characteristics, as is required for combustion modelling, can be performed for unconfined round jets by linear interpolation between scalar measurements at two different radial positions. However, in rectangular and multiple co-flowing systems linear interpolation between two radial positions for determining the concentration at specific downstream positions is not straight forward due to the non-axisymmetric nature of rectangles. Sforza *et al*., (1966) interpolated using elliptical isovels (elliptical curves) between each radial position in order to obtain a three dimensional map of the flow field of rectangular jets.

A different approach to representing or approximating three dimensional data from a complex system has been used in the current work. It uses a two dimensional regression of a scalar variable of specific transverse cross-sections of the flow field. Rather than model the longitudinal scalar characteristics of the flow, which is what has traditionally been done in the past, multiple transverse planes (cross-sections) are used to build up longitudinal values and thereby reproduce the three-dimensional characteristics of the jets.

7.2 Model Development

Section 3.2 identified and defined the independent variables of the current study as, x, y, z and λ. A model was developed using these variables.

7.2.1 Model Selection

As stated in section 6.1 the mean jets were mapped in the transverse direction yielding scalar matrices of concentration as a function of y and z. A series of candidate systems of three dimensional equations were trialed such as Gaussian error curves, polynomials, Gompertz model etc. Their ability to fit the data accurately and then be used to reproduce the three dimensional characteristics of the data were assessed. The modified version of the Gaussian error curve was employed:

$$a\exp\left\{-0.5\left[\left(\frac{\left|y/D-y_o\right|}{b}\right)^d-\left(\frac{\left|z/D-z_o\right|}{c}\right)^e\right]\right\} \qquad \textbf{Equation 7.1}$$

where a, b, c, d, e, y_o and z_o are all empirical constants. The choice of this model was based on the fact that it could map the high concentration gradients experienced in the shear layer close to the nozzle associated with rectangular and square jet flows. The constant 'a' represents the local maximum, of an ixj matrix, representing of time-averaged scalar mixture fraction.

Figure 7.1 is a schematic diagram representing the effect of the b, c, d and e terms on the modified Gaussian error curve. The constants 'b' and 'c' characterize the upper curvature or the intersection associated with oblique asymptote and the upper horizontal asymptotes as y/D or z/D $\longrightarrow 0$. The constants "d" and "e" characterize the curvature or the intersection of the oblique asymptote and lower horizontal asymptotes (as y/D or z/D. The terms y_o and z_o are the virtual origins of the jet in the y and z direction.

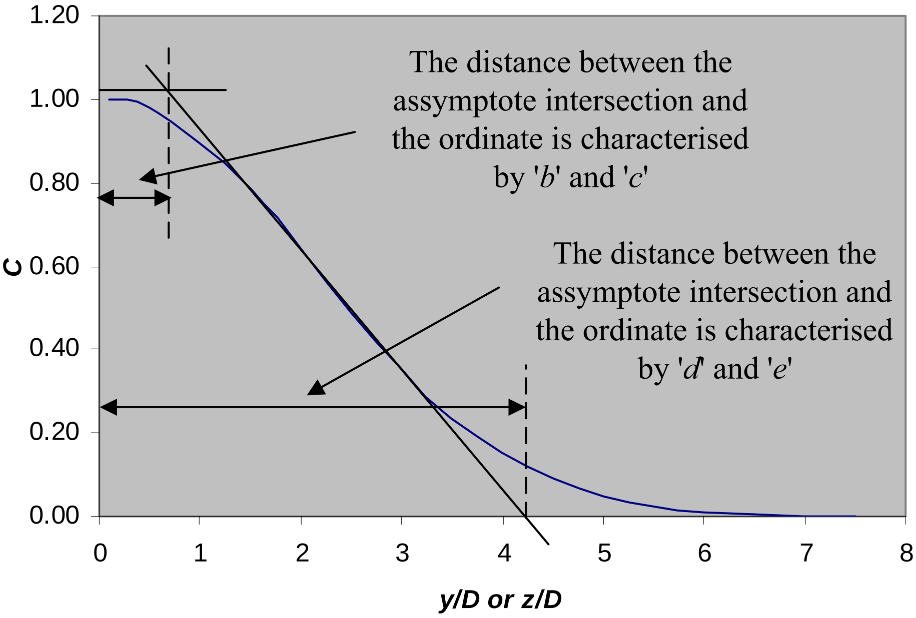

Figure 7.1: Schematic diagram of a form of the modified Gaussian error curve (Equation 7.1) with upper and lower tangential intersections illustrating the effect of parameters *b*, *c*, *d* and e on the modified Gaussian error curve.

7.2.2 Regression Procedure

Equation 7.1 was fitted to the time-averaged data of the primary and secondary jets described in Chapter 6. The curve fitting toolbox in Sigma Plot 9.0 (System Stat, 2006) which uses the method of weighted variables was applied. The normalised concentration with respect to the concentration on the centerline for each transverse image was used in preference to the mixture fraction because it has a local maximum of 1 anywhere in the flow field, whereas the mixture fraction does not, making the normalised concentration more sensitive to weighted regression techniques. The result is shown in equation 7.2.

$$\frac{\overline{C}}{\overline{C_c}} = a\exp\left\{-0.5\left[\left(\frac{|y/D-y_o|}{b}\right)^d - \left(\frac{|z/D-z_o|}{c}\right)^e\right]\right\}$$ **Equation 7.2**

The downside of using the normalised concentration is that the centerline mixture fraction of both the primary and secondary jets are required to complete the model. The centerline mixture fraction of the jets follow the inverse power law, introduced in Chapter 2, in the self-similar region, However, the results in Chapter 6 show how a co-flowing stream, such as the secondary jet, alters the centerline concentration. A 2nd order polynomial provides a good fit for the centerline mixture fraction data:

$$\frac{1}{\overline{\xi}_c} = \frac{\overline{C_o}}{\overline{C_c}} = \alpha\left(\frac{x}{D}\right)^2 + \beta\left(\frac{x}{D}\right) + \gamma$$

Equation 7.3

where the terms *α, β, γ* are the regression constants. The mixture fraction at any position in the flow is given by combining Equations 7.2 and 7.3:

$$\overline{\xi} = \frac{a\exp\left\{-0.5\left[\left(\frac{|y/D - y_o|}{b}\right)^d - \left(\frac{|z/D - z_o|}{c}\right)^e\right]\right\}}{\alpha\left(\frac{x}{D}\right)^2 + \beta\left(\frac{x}{D}\right) + \gamma}$$

Equation 7.4

The empirical constants *b, c, d*, *e* y_o z_o, are represented for all *x/D* and *λ,* and were modelled accordingly, whereas the terms *α, β, γ* were only modelled as a function of *λ*. A series of sub-models were obtained, which are presented in full in Appendix E. Several correlating methods such as the Chuchill-Usagi method (Chuchill and Usagi 1974) were attempted to derive appropriate relationships for the constants *x/D* and *λ*. However, simple numerical regression was chosen for it's ability to fit non linear equations to data-sets without requiring manual optimisation of parameters.

The data was reduced from 512*512 pixel images to 22*22 pixel images because of the large virtual memory required in the regression process. The reduction was performed by cropping the image to remove outside the jets, and then alternate columns and rows to conserve image integrity whilst reducing the amount of data. The procedure decreases the resolution of the cropped image as it is reduced to 22*22 pixels. Figure 7.2 shows a) the original time averaged primary flow image at *x/D* =0.1 for *λ*=0, b) the cropped image, and c) the reduced image respectively. The secondary jet image matrices were bisected by a centerline at *z/D* =0. The images were then reduced in a similar manner to the primary jet images. The terms *a, b, c, d* and *e* remained the same for the left hand and right hand secondary jets for each condition, whereas the terms y_o and z_o did not and had to be separately curve fitted.

The regression procedure delivered values for a, b, c, d, e y_o and z_o for all experimental conditions, These values were then modelled as a function of x/D and λ using polynomial, exponential and spline fitting techniques. The centreline mixture fractions were then curve fitted as a function of x/D using 2nd order polynomials. The terms α, β and γ, were then modelled as a function of λ, again using spline-fitted polynomials.

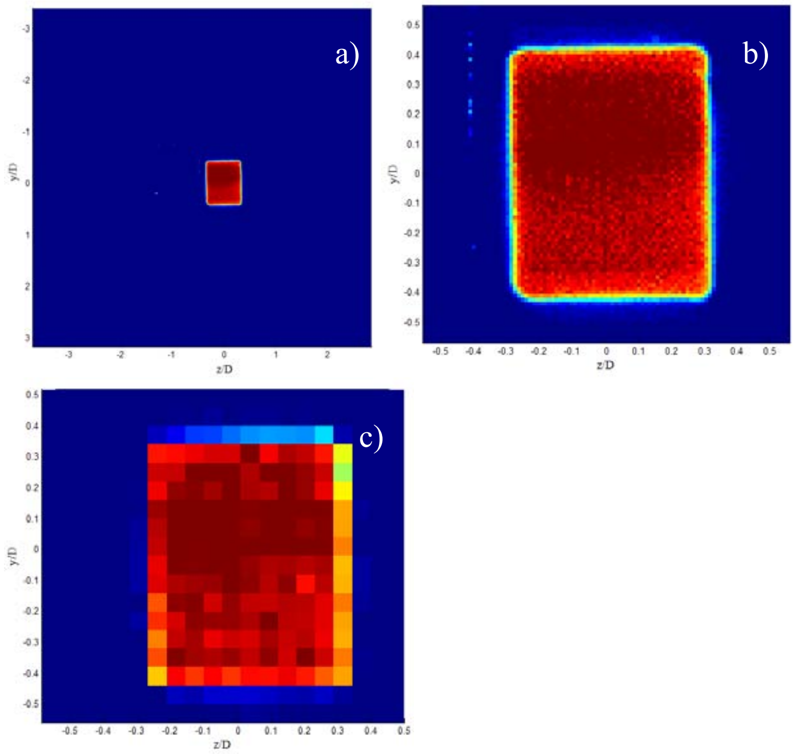

Figure 7.2: A time averaged primary flow image at x/D =0.1 for λ=0 a) the original image, b) cropped image and c) reduced image.

7.3 Model Results

7.3.1 Assessment of Mean Axial Data

Figure 7.3 compares the measured and interpolated centerline mixture fraction of the primary jet. The interpolated centerline mixture fraction has an absolute error of mostly between 0.3 and 11%. The only exception is for λ=1.4 and *x/D*>6 where the regression model under-predicts the actual mixture fraction by 20-25%.

The absolute errors associated in the interpolation of centerline mixture fraction of the secondary jet (Figure 7.4) generally does not exceed 20%, with the only exception being for λ=1.4 and *x/D*>4, where errors exceed 70%. Interpolation of the centerline mixture fraction is only a small portion of the field of the regression model's capabilities. Table 7.1 tabulates the errors in interpolated centreline mixture fraction over all *x/D* for each λ.

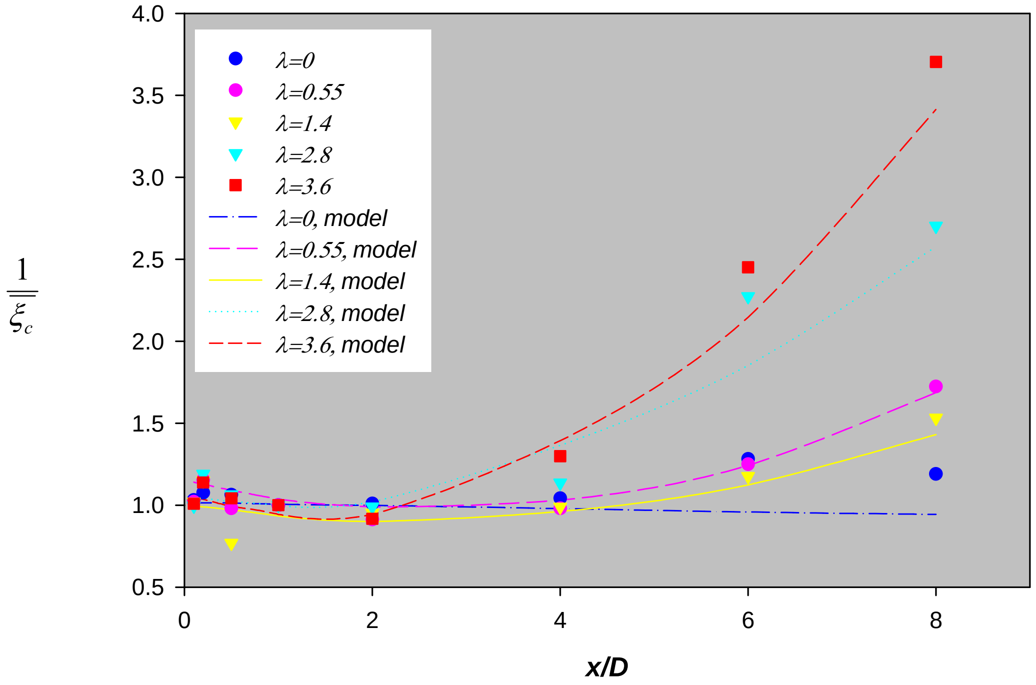

Figure 7.3: Comparison of measured and predicted values of centreline mean mixture fraction of the primary jet at velocity ratios of λ=0, 0.55, 1.4, 2.8 and 3.6.

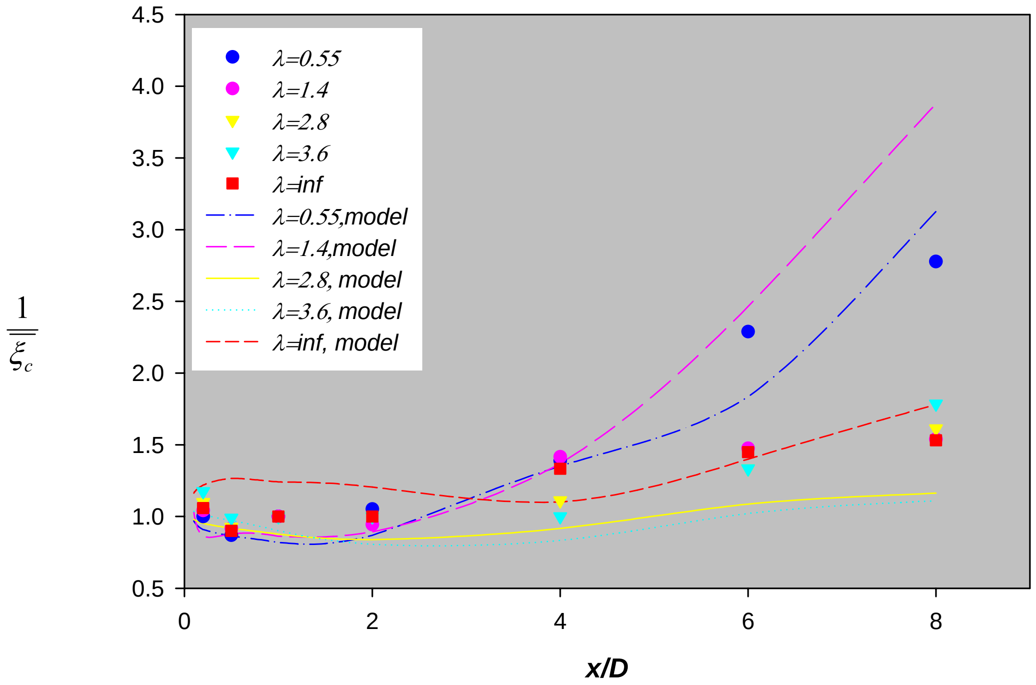

Figure 7.4 : Comparison of measured and predicted values of centreline mean mixture fraction of the secondary jet at velocity ratios of λ=0.55, 1.4, 2.8, 3.6 and ∞.

Jet	0	0.55	1.4	2.8	3.6	∞
Primary	±8.2%	±5.70%	±8.5%	±8.6%	±6.8%	NA
Secondary	NA	±11.5%	±37.6%	±15.2%	±17.6%	±19.6%

Table 7.1: Average estimated error between measured and predicted centreline mixture fraction for the primary and secondary jets.

7.3.2 Assessment of Cross Stream Concentration Profiles

Figures 7.5 to 7.12 show direct comparisons between the measured and predicted normalized concentrations of the primary jet at axial stations of x/D = 0.1, 1, 2 and 8 and at velocity ratios of 0 and 3.6. Only the positive values of z/D are reported in Figures 7.5-7.12 due to the symmetrical nature of the primary jet.

In the near field specifically at x/D=0.1 and λ=0 (Figure 7.5) the predicted normalized concentration in the bulk mixing region of the jet are within 25% of the measured values. Better predictions are achieved at low absolute values of z/D, such as z/D =0 and 0.15. However, even these cases have errors of approximately 25 % in the far shear layer. For a velocity ratio of λ=3.6 (Figure 7.6) the bulk mixing characteristics are still well predicted, with errors only rarely exceeding 10%. However, in the intermediate shear layer, for -0.4<*z/D*<-0.35 and 0.4>*z/D*>0.35, errors exceed 100%. These high errors are due to primary fluid peeling off at each corner of the primary jet as detailed in Chapter 6. The peeling off effect produces peaks in normalised concentration at *z/D* =-0.35 and 0.35, and at *y/D* =0.37 and -0.37. The modified form of the Gaussian error curve used is not well suited so cannot cope with this sort of sharp transition in concentration.

At *x/D* =1 and λ=0, Figure 7.7 shows comparisons between normalized measured and predicted values. The prediction improves slightly in the shear layer. The normalized concentration in the bulk flow is well predicted, (-0.4<*z/D*<0.4) with the absolute error rarely exceeding 20%. Similar results were obtained at λ = 3.6 (Figure 7.8).

Reasonable agreement is still achieved in the bulk fluid flow for *x/D* =2, λ=0 in Figure 7.9. For –0.4<*z/D*<0.4 and –0.6<*y/D*<0.6 predictions are not over estimated by more than 20%, however moving down progressively to *y/D* =-0.5 and 0.5 errors reach 30% and maximize to 80% for *y/D* =-0.8 and 0.8. For *z/D*<-0.4 and *z/D*>0.4 all points in the flow are overestimated by 60%. A change in velocity ratio to 3.6 alters significantly the fluid-dynamic nature of the flow, with the elongation of the primary jet in the *z*-direction and shortening in the *y* direction. The comparison of the predicted and measured normalized concentration at *x/D* =2 and λ=3.6 in Figure 7.10 shows how the regression model has problems predicting beyond *y/D*=0.3. The elongated shape of the primary jet in the *z*-direction requires a shortening in the *y*-direction, causing a steep concentration gradient in the shear layer. Consequently, in the region between –0.6<*z/D*<0.6 and *y/D*>0.3, the concentration is overestimated by values of no more than 30%, for *y/D*<0.3, absolute errors are less than 15%.

Concentration in the bulk fluid region for the primary jet at *x/D* =8 and λ=0 in Figure 7.11, (the bulk fluid region being –1.8<*z/D*<1.8 and *y/D*<2) is predicted within 20% and estimation of the concentration in the far shear layer (ie –1.8> *z/D*, *z/D*>1.8 and *y/D*>2) is achieved within 40% error. These trends in associated errors are also observed at a velocity ratio of 3.6 (Figure 7.12).

Figure 7.13 is the average relative error versus *z/D* for all the measured data-model comparisons in Figures 7.5-7.12. The results indicate that for 0.1 < *x/D* < 2, relative errors are below 40 % and are concentrated in the regions where bulk-fluid flow is encountered. For more extreme values of *z/D* heading further towards the shear layer, higher errors are encountered; this can be attributed to the regression model's difficulty in reproducing data for flows with high concentration gradients in the shear layer. For *x/D* =8 most errors are kept below 50%, due to the more 'relaxed' concentration gradients.

Similarly Figures 7.14-7.21 are the comparisons between measured and predicted normalized concentrations for the secondary jet at axial stations of *x/D*=0.1, 1, 2 and 8, for velocity ratios of λ=0.55 and 3.6. In Figures 7.14 and 7.15 at a downstream distance of *x/D*=0.1 and velocity ratios of λ=0.55 and 3.6, show that the normalized concentration in the bulk-fluid region is well predicted whereas in the far shear layer, predictions become less reliable. For λ=0, the region comprising between 0 < *y/D* < 0.4, -1.79 < *z/D* < -0.59 and 0.71 < *z/D* < 1.32 the normalized concentration was estimated within 30 % error. For λ=3.6, the region comprising between 0<*y/D*<0.4, -1.14<*z/D*<-0.7 and 0.69<*z/D*<1.14 the normalized concentration was estimated also within 30 % error.

Further downstream in Figures 7.16, 7.17, 7.18 and 7.19 for axial stations of *x/D* =1 and 2 respectively, the nature of the shear layer becomes more developed particularly from *x/D* =1 to *x/D*=2. This characteristic is felt throughout the regression model. In Figures 7.16-7.17, for *y/D* < 0.45, -1.08 < *z/D* < -0.45 and 0.2 < *z/D* < 1.17 all are within 40% error. Conversely in Figures 7.18 and 7.19 at *x/D*=2 and λ=0 and 3.6 respectively, errors are within 40% in the bulk flow region of *y/D* < 0.8, -1.4 < *z/D* < -0.62 and 0.74 < *y/D* < 1.48 for λ=0 and *y/D* < 0.8, -1.27 < *z/D* < -0.5 and 0.2 < *y/D* < 1.07 for λ=3.6.

In the far flow region of Figures 7.20 and 7.21 at *x/D* =8 at λ=0 and λ=3.6 where the jets have fully merged, the bulk fluid region comprising between *y/D* < 2.5 and –2.39 < *z/D* < 3.78 is over estimated by 30%.

Figure 7.22 is the calculated average relative error between the measured and predicted normalized concentration of the secondary jet for versus *y/D* for *x/D*=0.1, 2 and 8. The high concentration gradients in the near field at *x/D* =0.1 illustrate how the average error at *y/D* =0.3 is 60%, this increases progressively with *y/D* to 80 % and above. The intermediate region at *x/D* =2 provides small relative errors with measurements being predicted within 40%. The far region at *x/D* =8 also provides a relatively good fit within a 30% error range for *y/D*<1 with a progressive increase as observations are made further into the shear layer.

Errors between measured and predicted values can occur for several reasons such as sharp concentration gradients in the near field and the inability of the regression model to capture these gradients. Measurements with poor signal to noise ratios also contribute to errors. For instance in Figures 7.5 and 7.6 (primary jet, x/D =0.1, λ = 0 and 3.6 respectively) differences exist between the measured and predicted values because the large concentration gradients observed for $0.3<z/D<0.35$ which is typical as the jet has not yet developed. The modified Gaussian curve (Equation 7.4) has difficulty representing data in this region for the y and z–directions and is best suited for more developed flows as observed at x/D=1 and 2 in Figures 7.7 to 7.10. Another factor that can cause error between measured and predicted values is low quality experimental data. Figure 7.20 (secondary jet, x/D=8, λ=0.55) is a prime example of poor experimental data that has consequently altered the output of the regression procedure. The measured flow at x/D =8 has been diluted through entrainment to the point that the emitted signal is weak and susceptible to low signal to noise ratios, consequently rather than a 'smooth' Gaussian profile a noisy one is encountered, which can affect the regression procedure. The outcome of this is the large variance between measured and predicted values is illustrated in Figure 7.20.

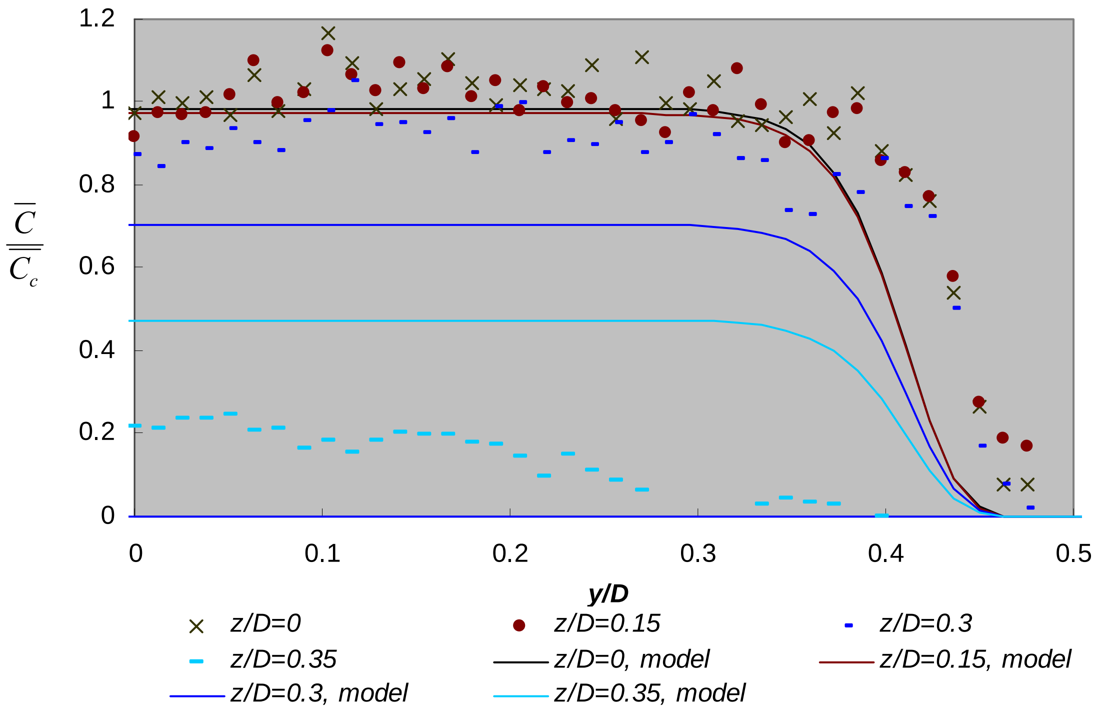

Figure 7.5: Comparison of the measured and predicted normalised concentration of the primary jet varying z/D at λ=0, x/D=0.1.

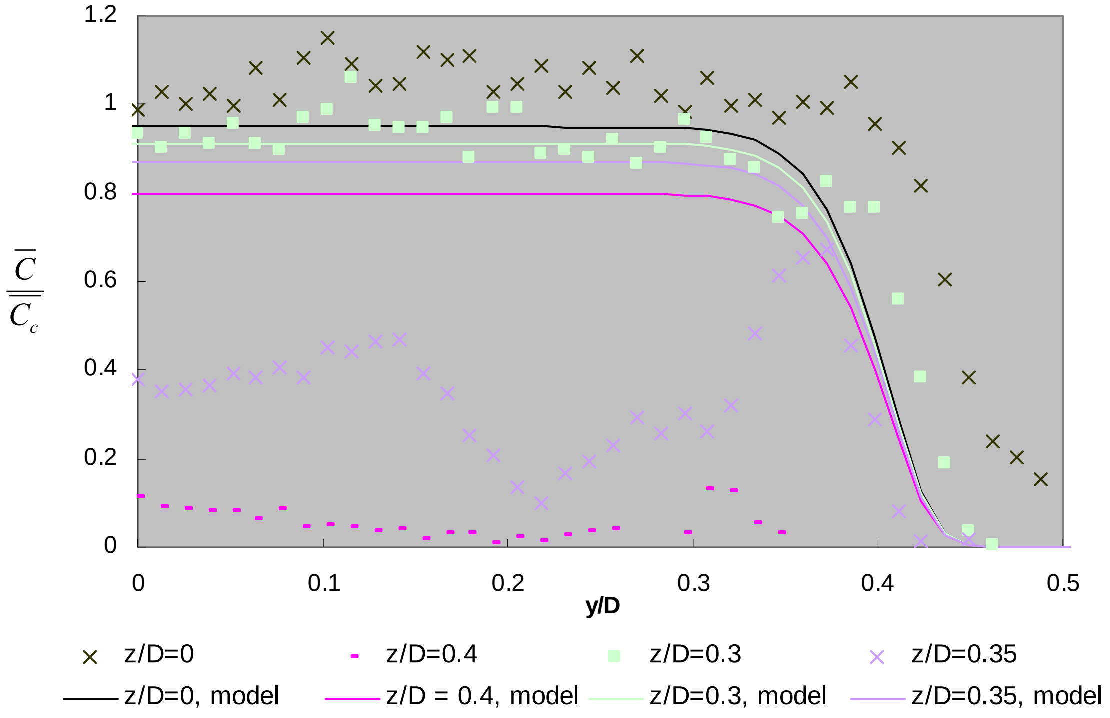

Figure 7.6: Comparison of the measured and predicted normalised concentration of the primary jet varying *z/D* at λ=3.6, *x/D*=0.1.

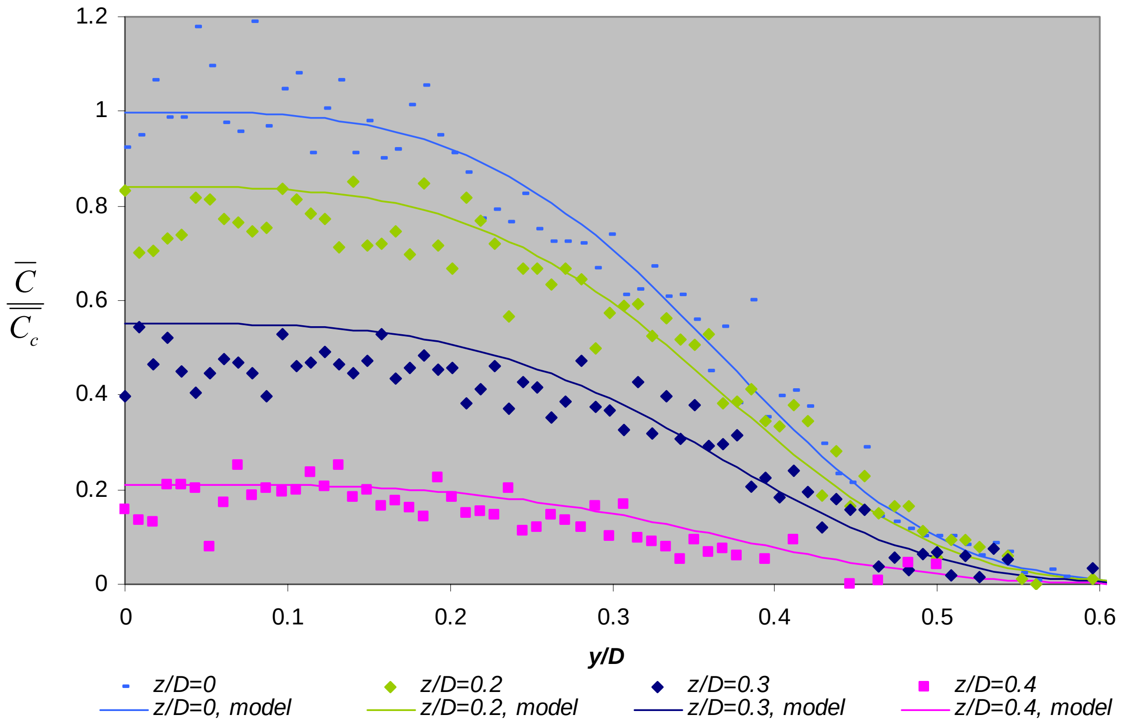

Figure 7.7: Comparison of the measured and predicted normalised concentration of the primary jet varying of *z/D* at λ=0, *x/D*=1.

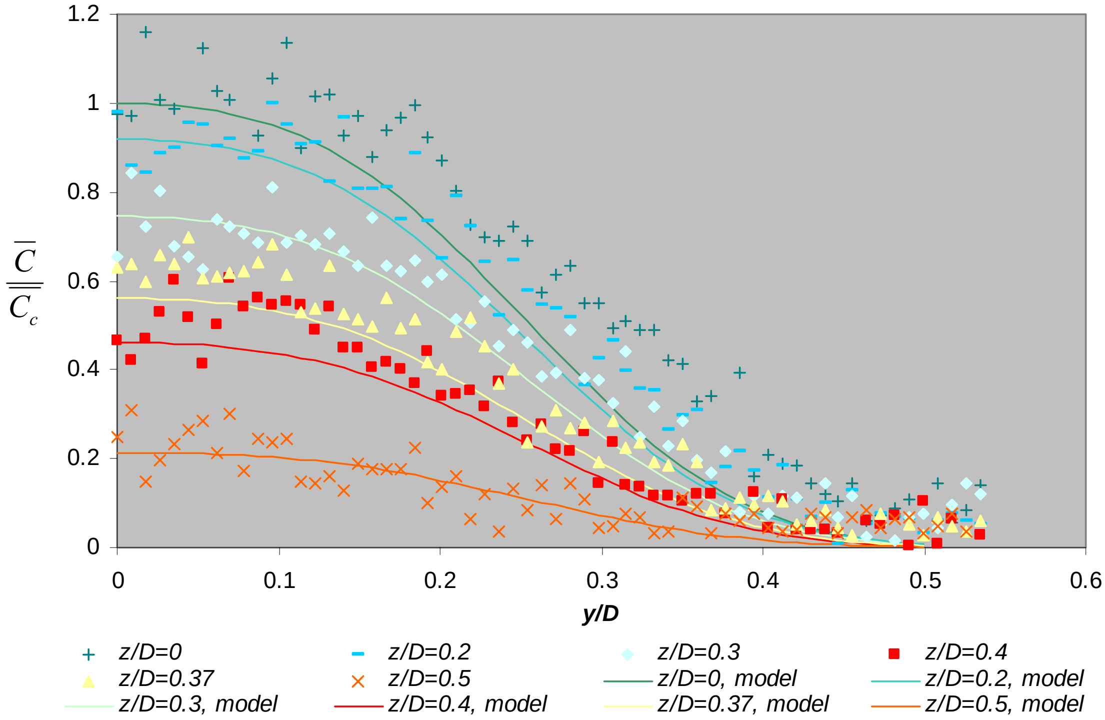

Figure 7.8: Comparison of the measured and predicted normalised concentration of the primary jet for different values of *z/D*, λ=3.6, *x/D*=1.

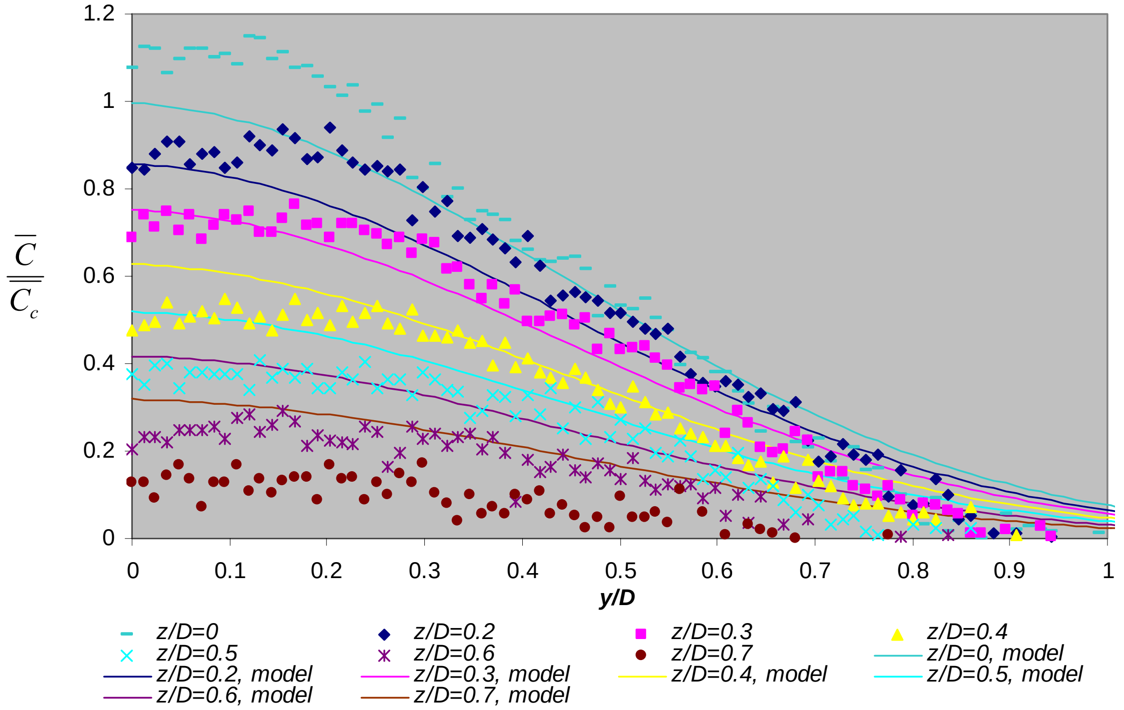

Figure 7.9: Comparison of the measured and predicted normalised concentration of the primary jet for different values of *z/D*, λ=0, *x/D*=2.

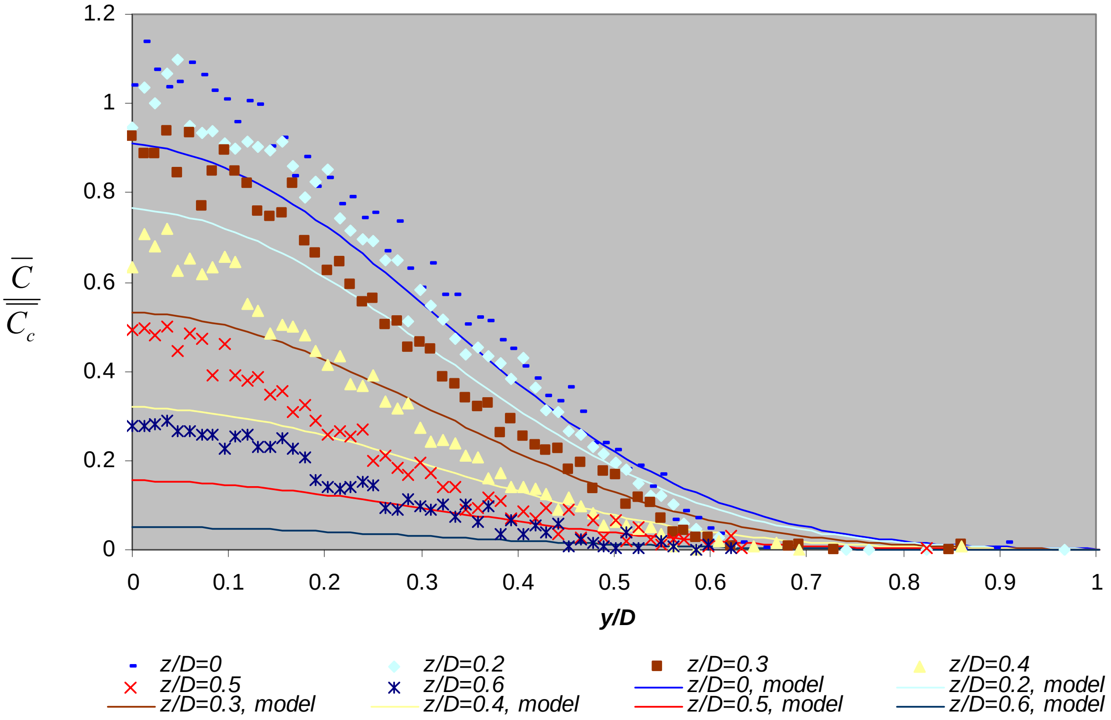

Figure 7.10: Comparison of the measured and predicted normalised concentration of the primary jet varying of z/D at λ=3.6, x/D=2.

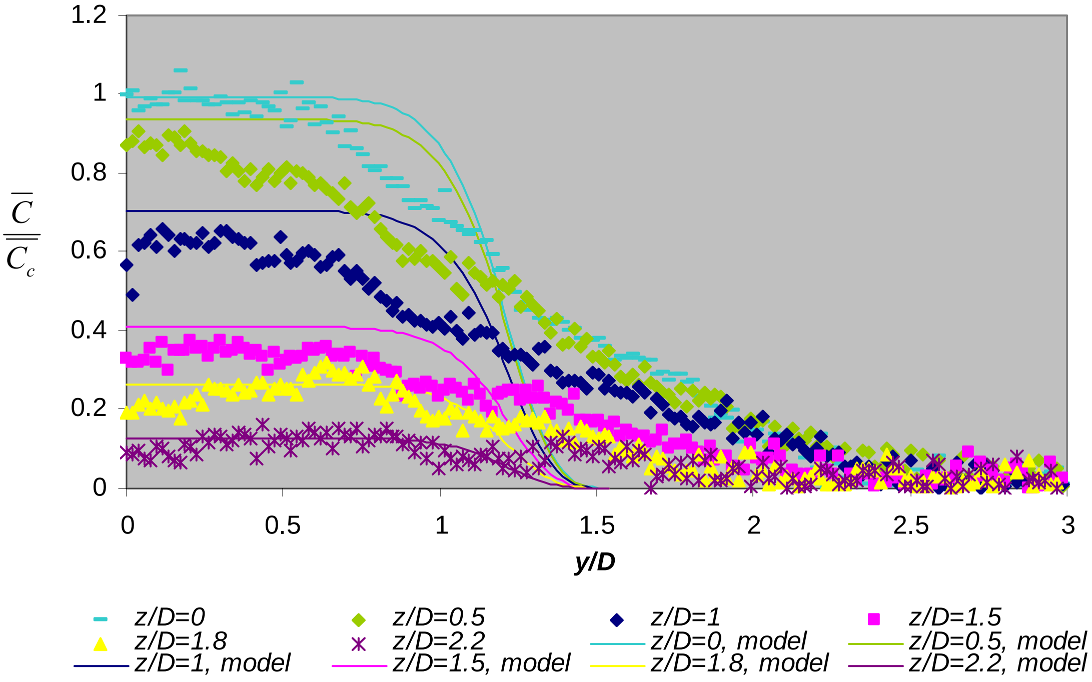

Figure 7.11: Comparison of the measured and predicted normalised concentration of the primary jet for different values of z/D, λ=0, x/D=8.

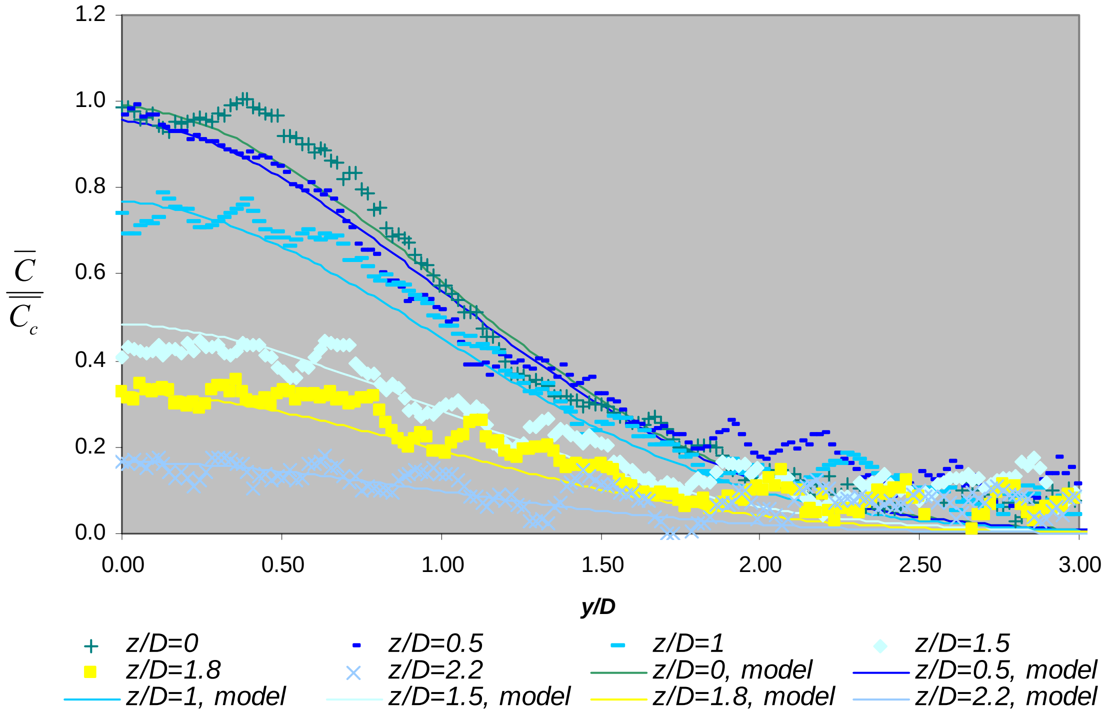

Figure 7.12: Comparison of the measured and predicted normalised concentration of the primary jet varying z/D at λ=3.6, x/D=8.

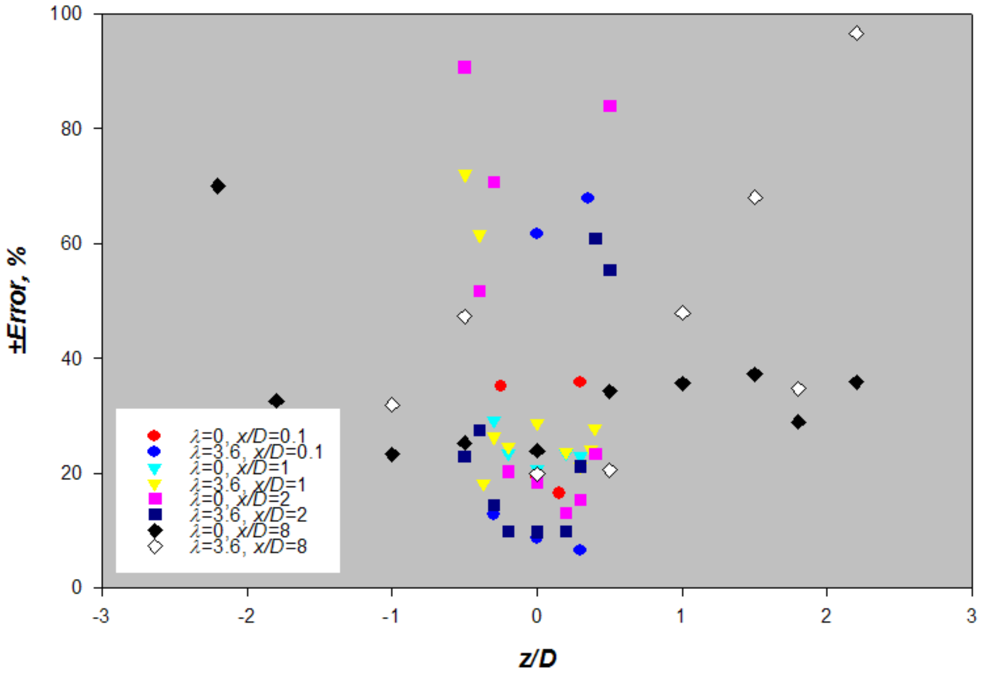

Figure 7.13: Relative Error of model predictions of the primary jet at axial stations of x/D = 0.1, 1, 2 and 8, for λ=0 and 3.6.

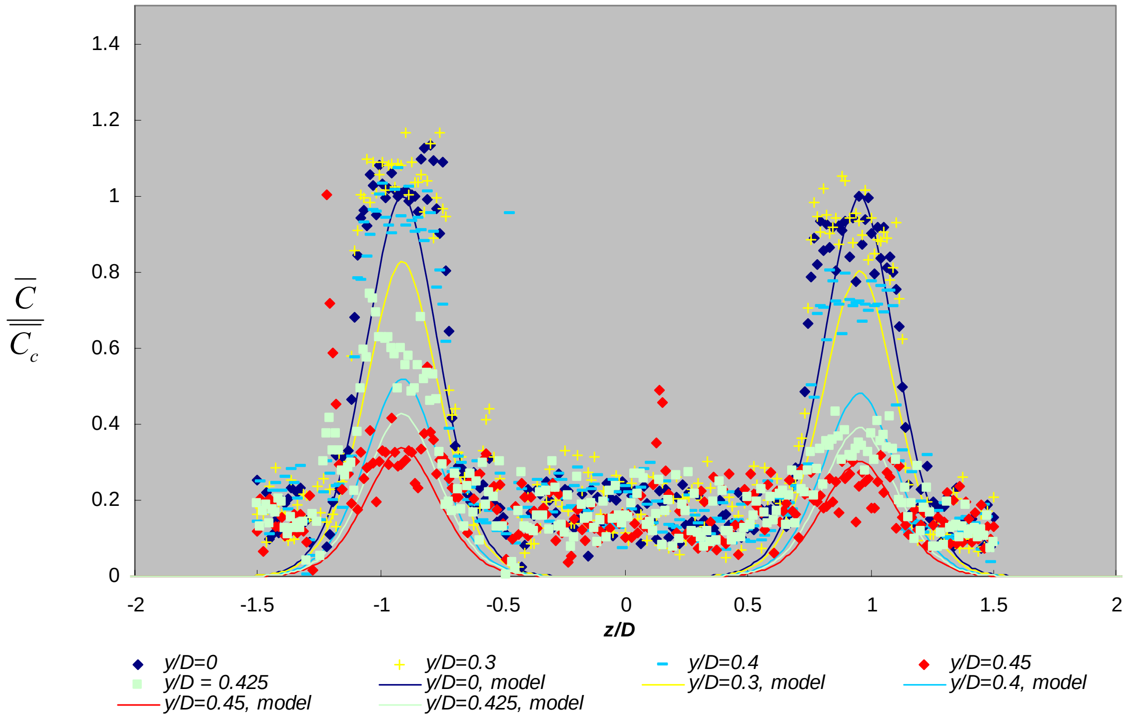

Figure 7.14: Comparison of the measured and predicted normalised concentration of the secondary jet varying *z/D* at λ=0.55, *x/D*=0.1.

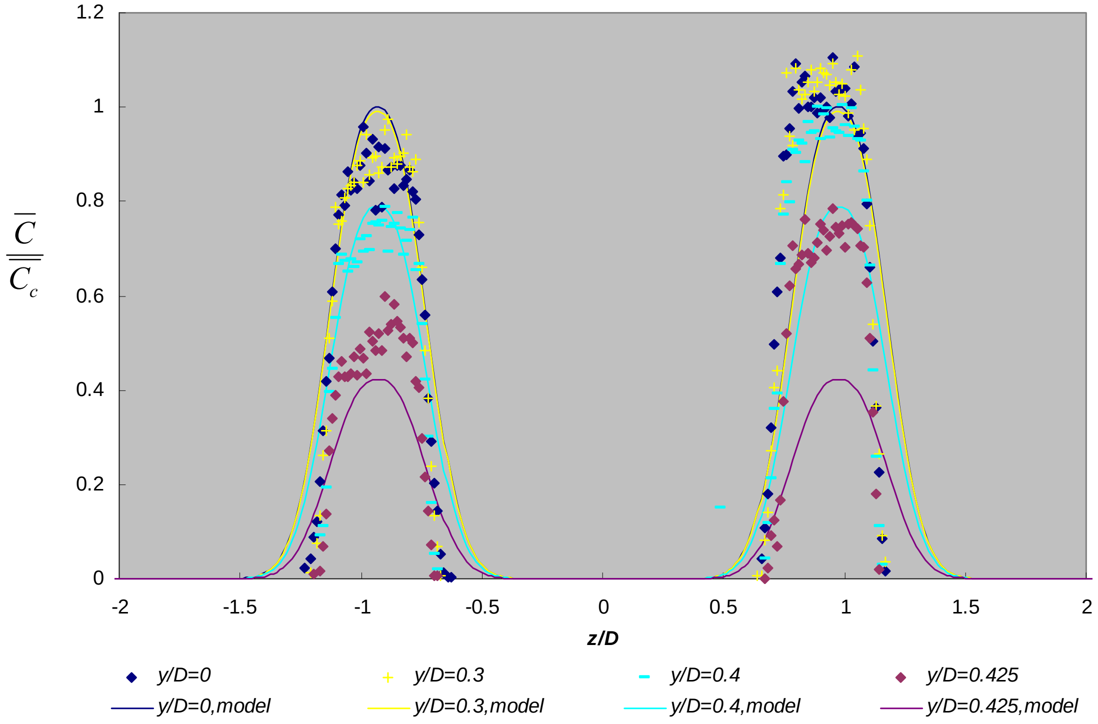

Figure 7.15: Comparison of the measured and predicted normalised concentration of the secondary jet for varying *z/D*, λ=3.6 at *x/D*=0.1.

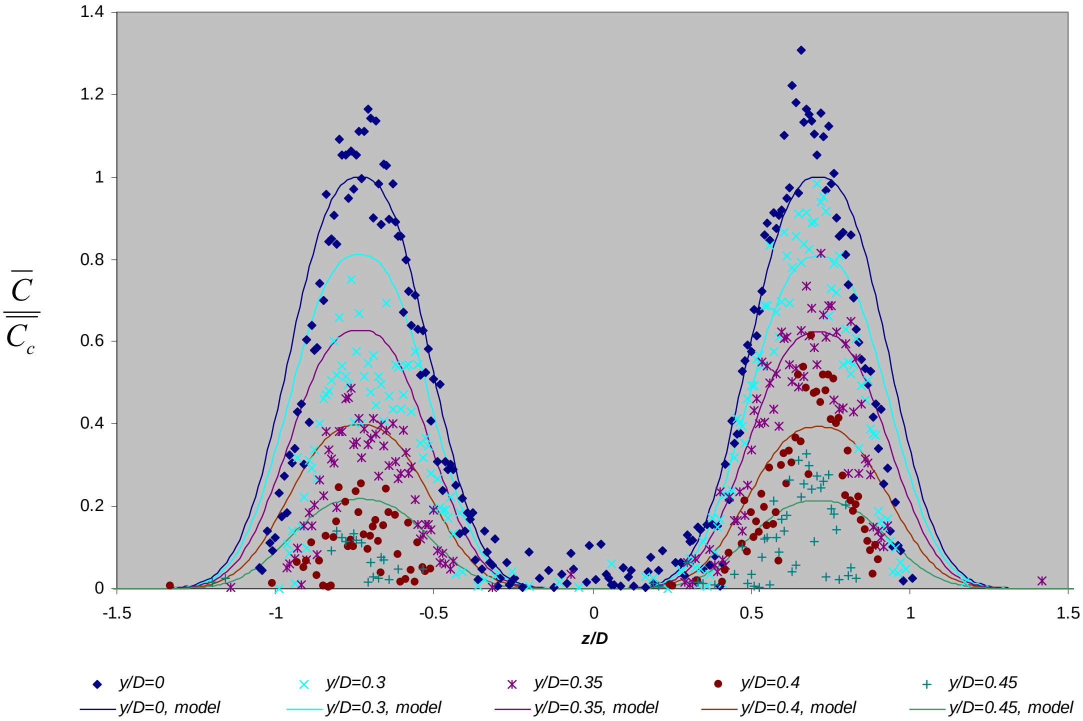

Figure 7.16: Comparison of the measured and predicted normalised concentration of the secondary jet for different values of z/D, λ=0.55, x/D=1.

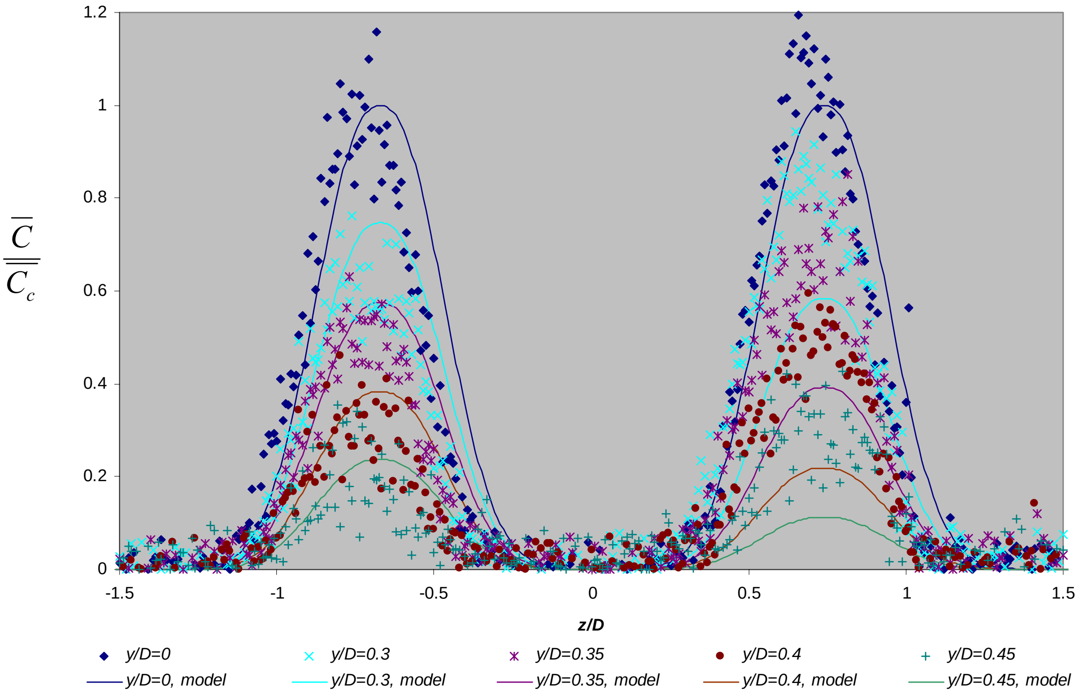

Figure 7.17: Comparison of the measured and predicted normalised concentration of the secondary jet for different values of z/D, λ=3.6, x/D=1.

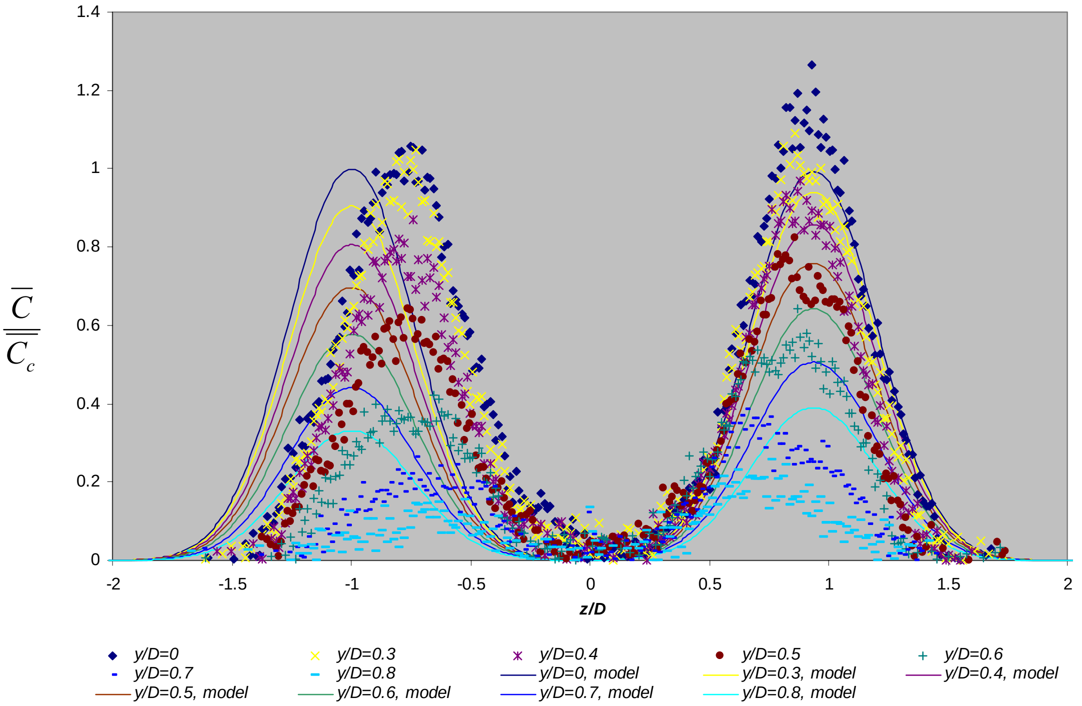

Figure 7.18: Comparison of the measured and predicted normalised concentration of the secondary jet for different values of *z/D*, λ=0.55, *x/D*=2.

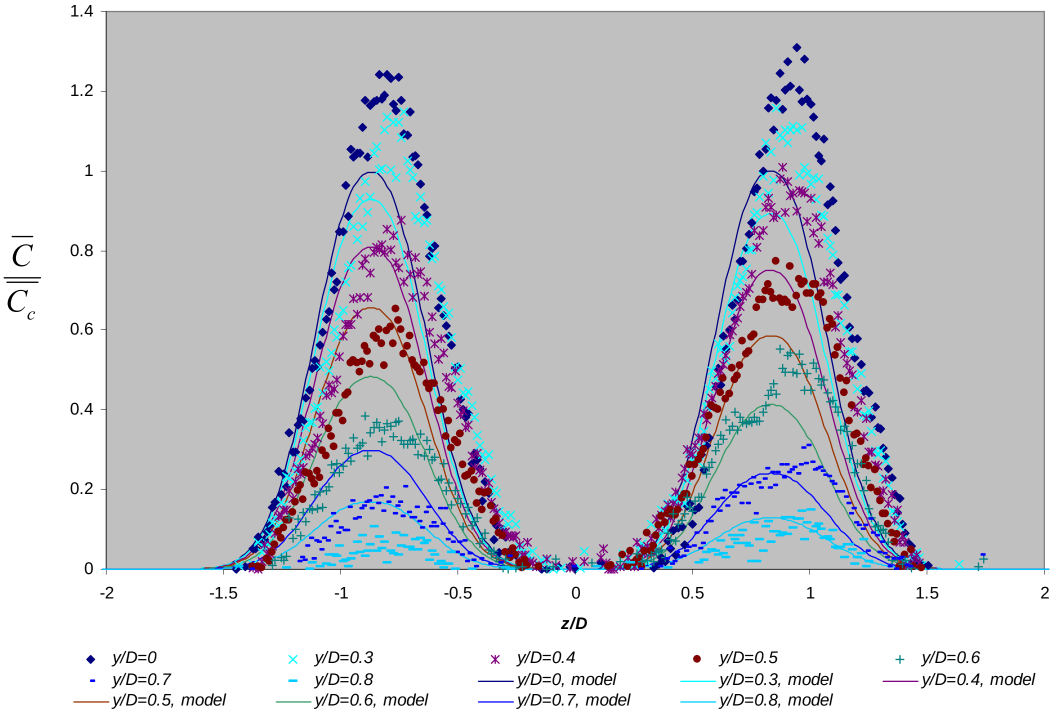

Figure 7.19: Comparison of the measured and predicted normalised concentration of the secondary jet for different values of *z/D*, λ=3.6, *x/D*=2.

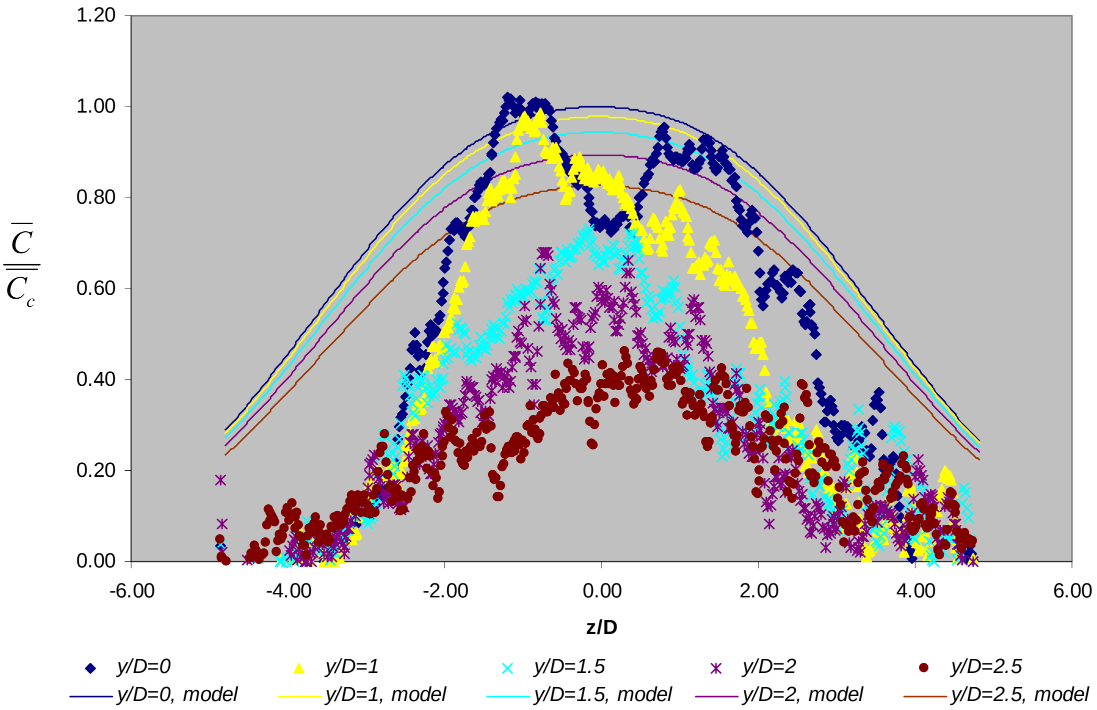

Figure 7.20: Comparison of the measured and predicted normalised concentration of the secondary jet for different values of z/D, λ=0.55, x/D=8.

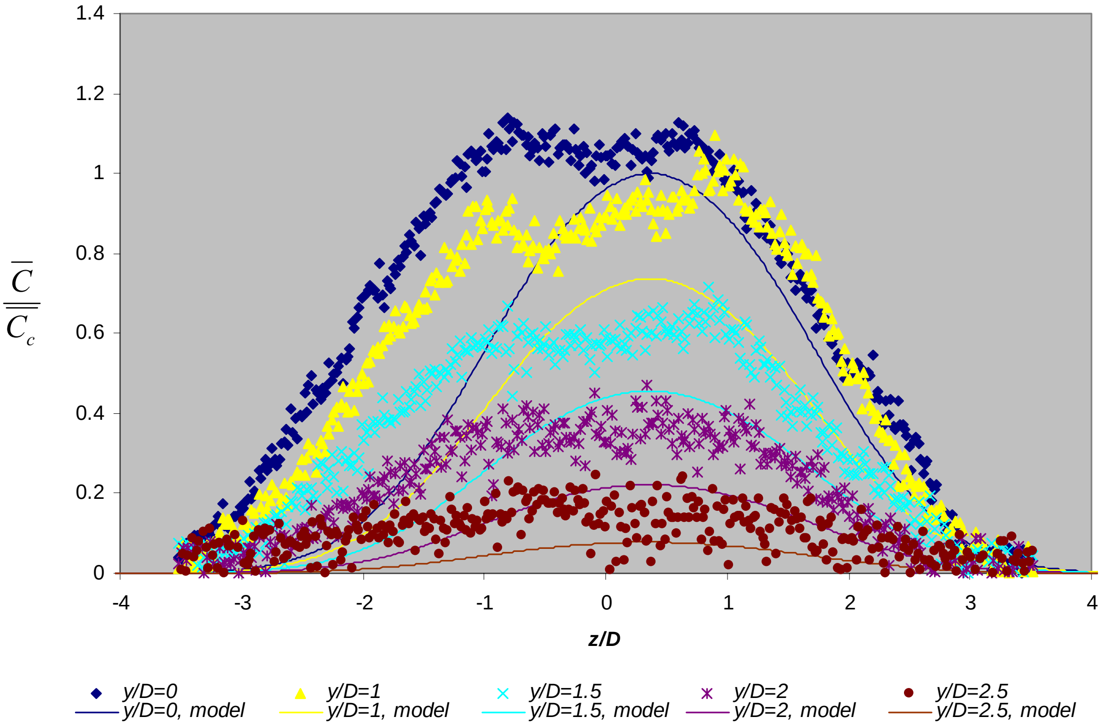

Figure 7.21: Comparison of the measured and predicted normalised concentration of the secondary jet for different values of z/D, λ=3.6, x/D=8.

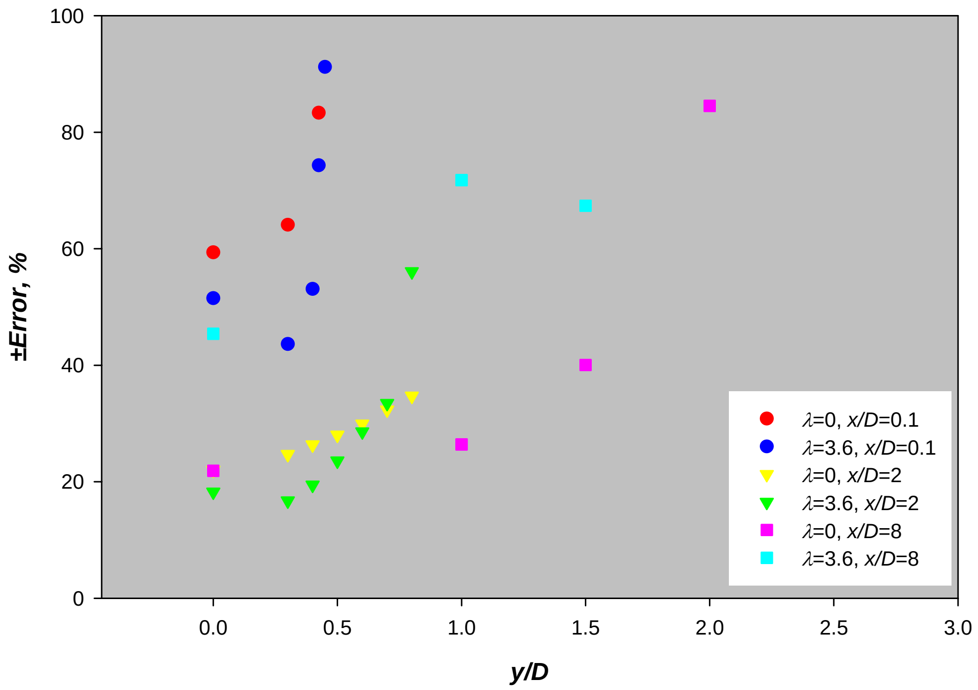

Figure 7.22: Relative Error of model predictions of the primary jet at axial stations of x/D = 0.1, 1, 2 and 8, for λ=0 and 3.6.

7.3.3 Analysis of Variance

Analysis of variance can be used to test the significance and accuracy of the regression model. The analysis of variance compares the regression model to the fitted data by means of a series of statistical tests. The first step when statistically analyzing a regression model is an analysis of the residuals. The raw residuals from any regression model are defined as;

$$e_i = y_i - \hat{y}_i$$ **Equation 7.5**

where y_i is i^{th} the observed variable and $\hat{y}_i$ is the predicted response from the regression model. Other forms such as ‘studentized’ and ‘press residuals’ exist (Montgomery, 1999) and are widely used, however in the current work the standardized residual was used:

$$d_i = \frac{e_i}{\sqrt{MSE}}$$ **Equation 7.6**

where the term *MSE* is the 'mean squared error', and will be defined later. Residuals which fall in of the interval -2 < d_i < +2 are deemed "outliers" (Montgomery, 1999). Figures 7.23 and 7.24 show the standardized residuals for the centerline mixture fraction of the primary and secondary jets respectively. The scatter of the standardized residuals for both jets indicates whether the associated errors are random or systematic.

The error sum of squares, SSE is dependant on the difference between the measured output, y_i and the model's response $\hat{y}_i$, and the number of observations, *N*:

$$SS_E = \sum_{i=1}^{N} \left(y_i - \hat{y}_i \right)^2$$ **Equation 7.7**

The total corrected sum of squares is similarly related to the difference measured or observed variable and the mean measured variable over the data pool, $\bar{y}$.

$$SS_T = \sum_{i=1}^{N} \left(y_i - \bar{y} \right)^2$$ **Equation 7.8**

The regression sum of squares is then defined as;

$$SS_R = \sum_{i=1}^{N} \left(\hat{y}_i - \bar{y} \right)^2$$ **Equation 7.9**

Hence;

$$SST = SSE + SSR$$ **Equation 7.10**

The mean square error, *MSE*, and mean square regression, *MSR*, are defined as;

$$MSE = \frac{SSE}{n-2}$$ **Equation 7.11**

$$MSR = \frac{SSE}{m-1}$$ **Equation 7.12**

where the terms *n* and *m* are the degrees of freedom in the error and regression response respectively. The coefficient of determination, or '*R*-squared' can be calculated from the sum of error squared and total corrected sum of squares;

$$R^2 = 1 - \frac{SS_E}{SS_T}$$ **Equation 7.13**

The maximum obtainable value of R^2 is 1. This indicates a perfect fit between measured and predicted values. Evaluation of the mean square error of a particular data set as well as calculation of R^2 quantifies the 'goodness of fit' of a regression model to data, and the model's ability to re-produce intermediate values.

Hypothesis testing using the *F*-test is another method that can be applied to test model adequacy. For example, when fitting data to an equation such as $y=mx+q$ by linear regression two possible null hypotheses are:

$$H_o : m = 0$$

$$H_1 : m \neq 0$$

If H_o is true, a curve with slope m=0, will fit the data more accurately than a curve with $m=0$. To test this hypothesis the F-test is conducted. The F value is the ratio of the mean square regression and mean square error:

$$F_o = \frac{MSR}{MSE}$$ **Equation 7.14**

The hypothesis H_o would be rejected, and H_1 accepted, if:

$$F_o > f_{\alpha,m-1,n-2}$$ **Equation 7.15**

where $f_{\alpha,m-1,n-2}$ is the tabulated *f*-value (Montgomery, 1999) for a given confidence value α, and degrees of freedom *m* and *n*. Null-hypothesis testing such as this can be applied to a complex regression model such as Equation 7.4, for example, for the term *a*.

$$H_o : a = 0$$

$$H_1 : a \neq 0$$

Other null hypothesis tests exist such as the Mann-Whitney U test (Mann and Whitney, 1947), Wilcoxon signed-rank test (Wilcoxon, 1945) and the student *t*-test. However, these have not been applied here because the *MSE*, R^2 and F-tests are sufficient to determine whether the model is adequate.

An analysis of variance was conducted on some of the data detailed in Section 6.3, specifically the centreline and cross-stream mixture fraction at a range of axial stations. Total mean R^2 and *MSE* values were calculated for each time-averaged data point.
Table 7.2 shows the results for the primary jet. Visual comparisons between the measured and predicted data for the primary jet, illustrated in Figure 7.3, indicated that the regression model can adequately reproduce centreline data. The analysis of variance concurs with the observation for most velocity ratios. All values of MSE are <0.05, and most R^2 values are acceptable. The critical F-value is approximately 2.4 for a confidence interval of α =0.05. Hence the null hypothesis, ie that *a* = 0 may be rejected for most values of λ. The secondary jet model demonstrates acceptable values of *MSE* and R^2 for centreline mixture fraction for λ= 0.55, 3.6 and ∞ (Table 7.3). The null hypothesis is accepted for λ=1.4 and 2.8.

The observed values of R^2 on the primary and secondary jet centreline for λ=0 in Table 7.2 and λ=1.4 in Table 7.3 are negative. A data point which has a negative R^2 quite often represents a poor fit, this does not necessarily mean that the regression model is inadequate just that it is not well represented around the region of that particular data point. In order to gain minimum variance between measured and predicted values splines were used for certain regions of λ, *x/D*, *y/D* and *z/D*. It is sometimes possible that part of or the entire splined region yields a less than perfect fit, which is what is being observed with the current regression model.

Negative values of R^2 and have been cited in the literature by a number of authors. Casella (1983) studied the statistical difference between models passing through the origin and stated that it is possible for R^2 to be negative and will occur when the error sum of squares (*SSE*) is large, indicating a poor fit. Park (1978), who statistically evaluated the value of exposure to television in humans, explicitly came across $R^2 < 0$, and observed that the error sum of squares was greater than the total corrected sum of squares (*SST*). Willems *et al*., (2007) used regression models to study the interaction of electricity firms found circumstances where $R^2 < 0$ and stated that in the case $R^2 < 0$, the average value of the experimental data ($\overline{y}$) may be regarded as a more suitable predictor. Nielsen (1999) who studied the parametric and non-parametric methods of regression also encountered $R^2 < 0$ and came to the same conclusion based on theories developed by Kvalseth (1985) who states that R^2 can very well be negative however it's occurrence is attributed to either a poor fit or the presence of outliers in an otherwise robust regression model. According to Neter and Wasserman (1996), $R^2<0$ can occur when a regression model with data through the origin is incorporated. As an extension to the statement made by Neter and Wasserman (1996), Becker and Kennedy (1992) verify that $R^2 <0$ can also arise when poor fits are obtained with regression models which were developed without incorporating any data through the intercept (i.e. not using any data when x=0). This is the case for the current regression model since no measurements were taken at x/D =0, y/D =0 or z/D =0 because it is impossible to shine the laser at these coordinates, as significant reflection would occur as a result.

Figure 7.25 shows the R^2 values in the primary jet as a function of cross-stream position. The data shows that the best model predictions are made near the centreline, and that worse predictions occur in the shear layer. At x/D =8, a greater amount of scatter is encountered. This is due to the reduced signal to noise ratio as jet fluid is being diluted. Tables 7.4 to 7.6 present calculated F_o values in the primary jet. The associated values of $F_{critical}$ are given in the table captions. The F_o values substantiates the validity of the model in the majority of the flow field. For the region outside the shear layer the regression model generates a zero mixture fraction; this incurs errors when compared to the non-zero values of the experimental background images due to the presence of noise. Figure 7.26 shows that localised R^2 values in the secondary jets reduce with increasing y/D. The F_o values in the secondary jet (Tables 7.7-7.9) correspond to the rejection of the null hypothesis in the bulk fluid flow region. A complete set of the data obtained from the localised analysis of variance can be found in Appendix F.

An analysis is required over a larger range of data points so that the overall regression model performance can be assessed. Figures 7.27 and 7.28 show the averaged mean square error for the primary and secondary jets, respectively, over a 512*512 pixel array. The MSE were calculated from the measured and predicted normalised concentration and then averaged over 512*512 pixels. Larger mean square errors in the near field for both jets confirm the results from the localised analysis of variance, that the model has difficulty coping with the large concentration gradients in the shear layer. Figures 7.29 and 7.30 show the mean R^2 values for the primary and secondary jets, respectively over a 512*512 array. Values of R^2 between 0.6 and 0.8 are found in the near field for $x/D<1$, except for some lower values very close to the exit plane. The downstream dilution of the jet causes the signal intensity to decrease thus increasing the signal to noise ratio and slightly reducing R^2 values.

In summary, the analysis of variance indicates that the regression model adequately fits the measured data, particularly in the intermediate field.

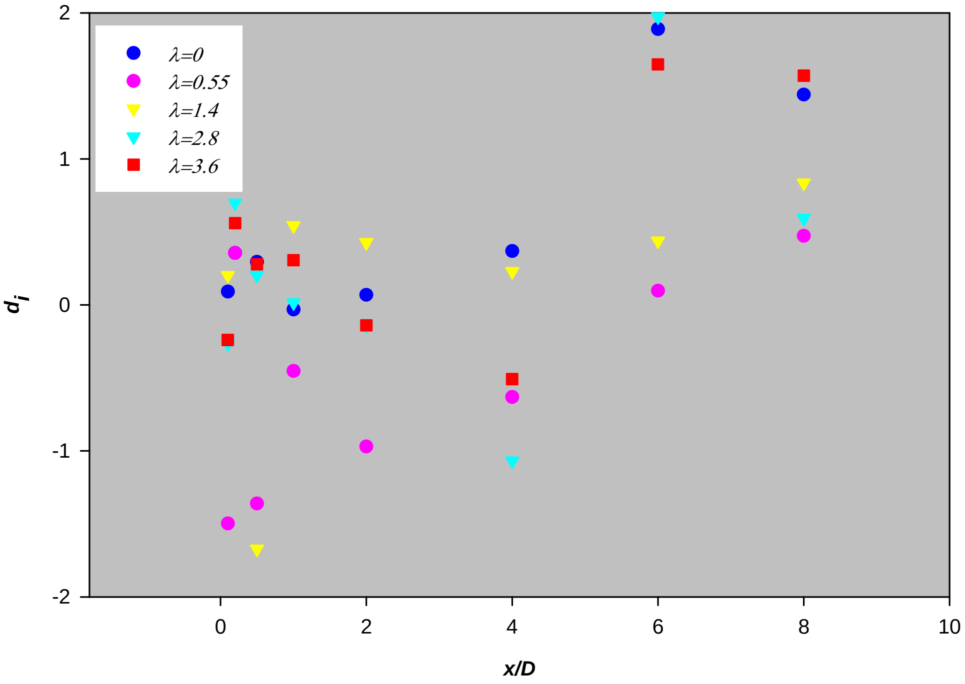

Figure 7.23: Standardised residuals versus normalised axial distance for the primary jet.

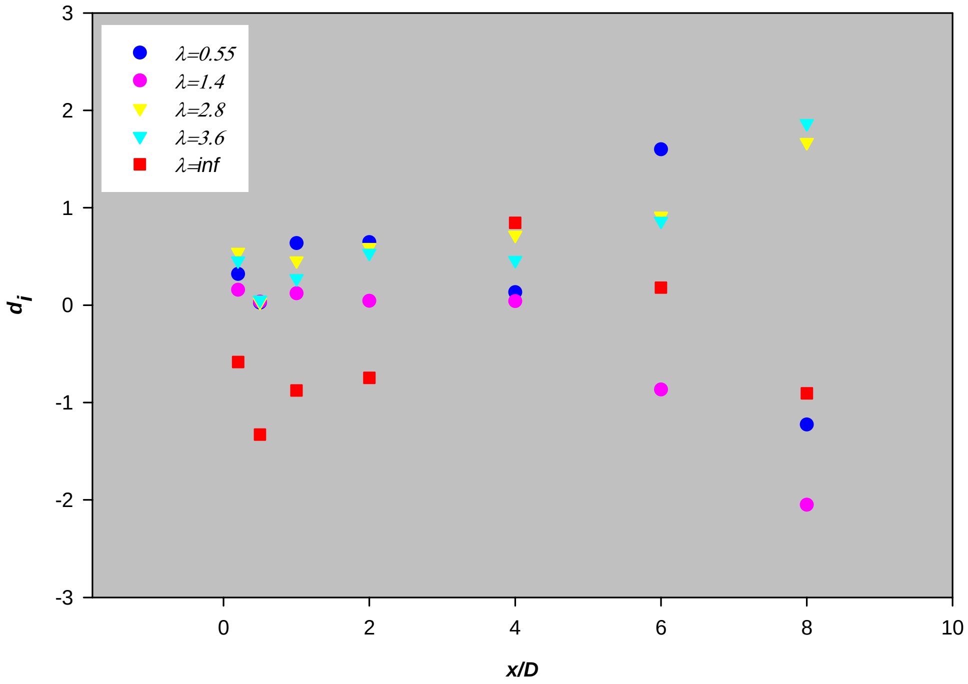

Figure 7.24: Standardised residuals versus normalised axial distance for the secondary jet.

	λ	**Sum of squares**	**Mean Square**	F_o	R^2
	0				
Regression		-0.11	-0.03	-0.92	-1.60
Error		0.18	0.03		
Total		0.07			
	0.55				
Regression		0.45	0.11	17.58	0.92
Error		0.04	0.01		
Total		0.49			
	1.4				
Regression		0.26	0.07	4.49	0.75
Error		0.09	0.01		
Total		0.35			
	2.8				
Regression		2.90	0.73	15.92	0.91
Error		0.27	0.05		
Total		3.17			
	3.6				
Regression		6.73	1.68	49.05	0.97
Error		0.21	0.03		
Total		6.93			

Table 7.2: Analysis of variance results for the measured and predicted centreline mixture fraction of the primary jet**.**

	λ	Sum of squares	Mean Square	F_o	R^2
Regression	0.55	4.06	1.01	12.61	0.91
Error		0.40	0.08		
Total		4.46			
Regression	1.4	-6.02	-1.51	-1.16	-12.70
Error		6.50	1.30		
Total		0.47			
Regression	2.8	0.03	0.01	0.10	0.08
Error		0.36	0.07		
Total		0.39			
Regression	3.6	0.25	0.06	0.48	0.28
Error		0.66	0.13		
Total		0.91			
Regression	∞	1.05	0.26	3.50	0.74
Error		0.38	0.08		
Total		1.43			

Table 7.3: Analysis of variance results for the measured and predicted centreline mixture fraction of the secondary jet**.**

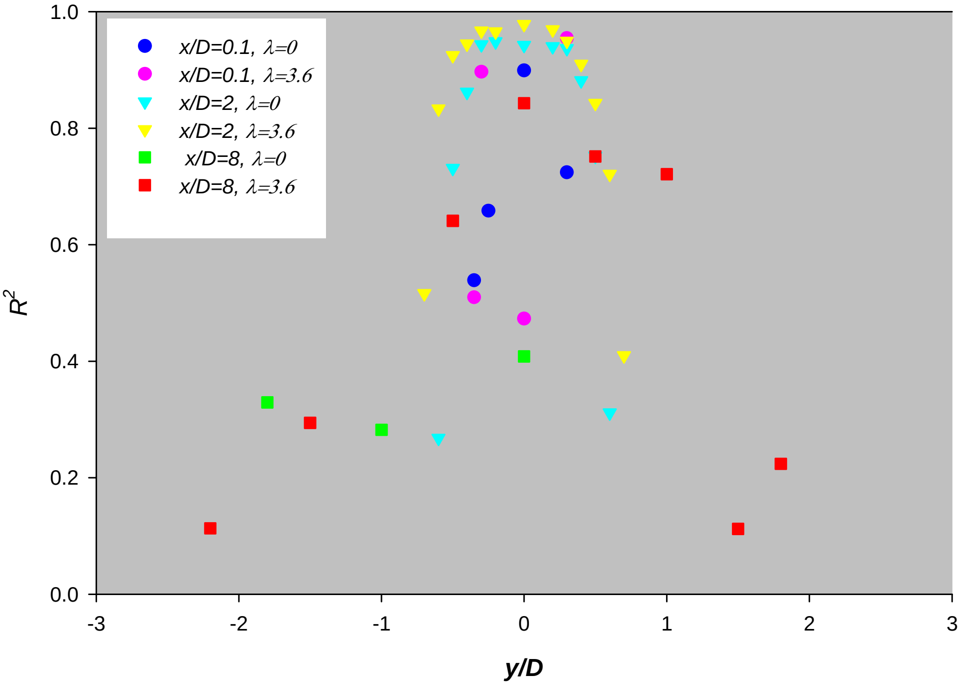

Figure 7.25: Localised R^2 versus y/D for the primary jet at x/D =0.1, 2 and 8 for velocity ratios of λ=0 and λ=3.6.

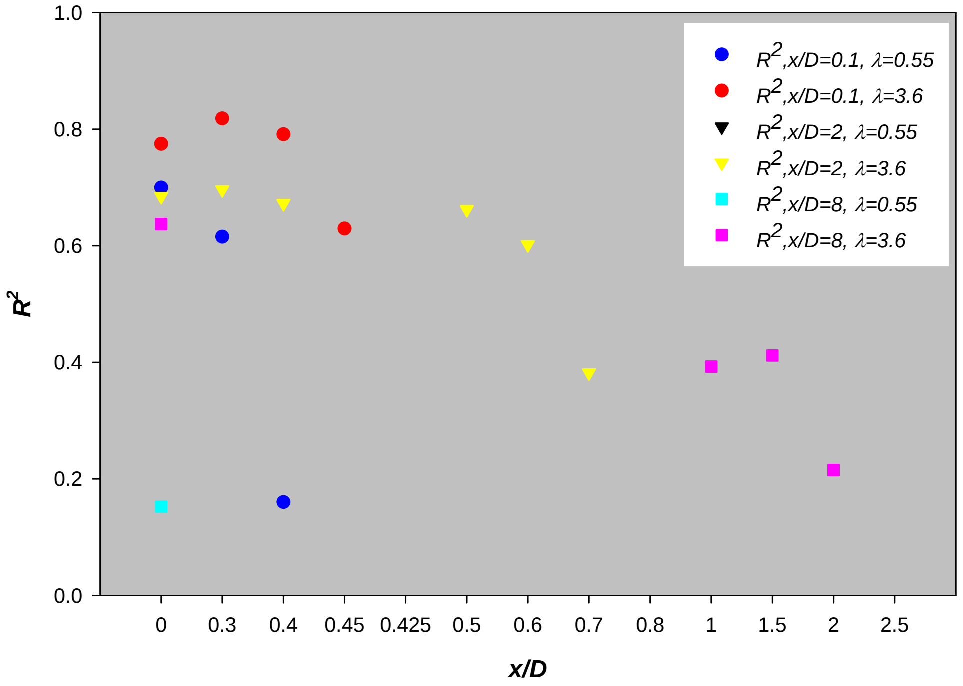

Figure 7.26: Localised R^2 versus *y/D* for the secondary jet at *x/D* =0.1, 2 and 8 for velocity ratios of λ=0 and λ=3.6.

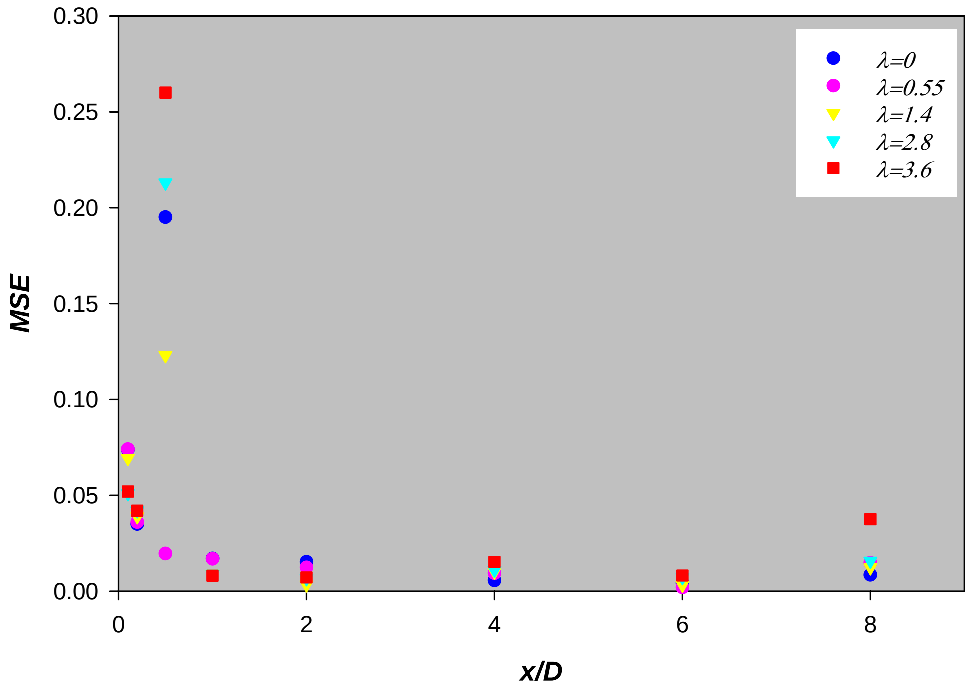

Figure 7.27: Averaged mean square error versus *x/D* for the primary jet at velocity ratios of λ=0, 0.55*,* 1.4*,* 2.8 and 3.6.

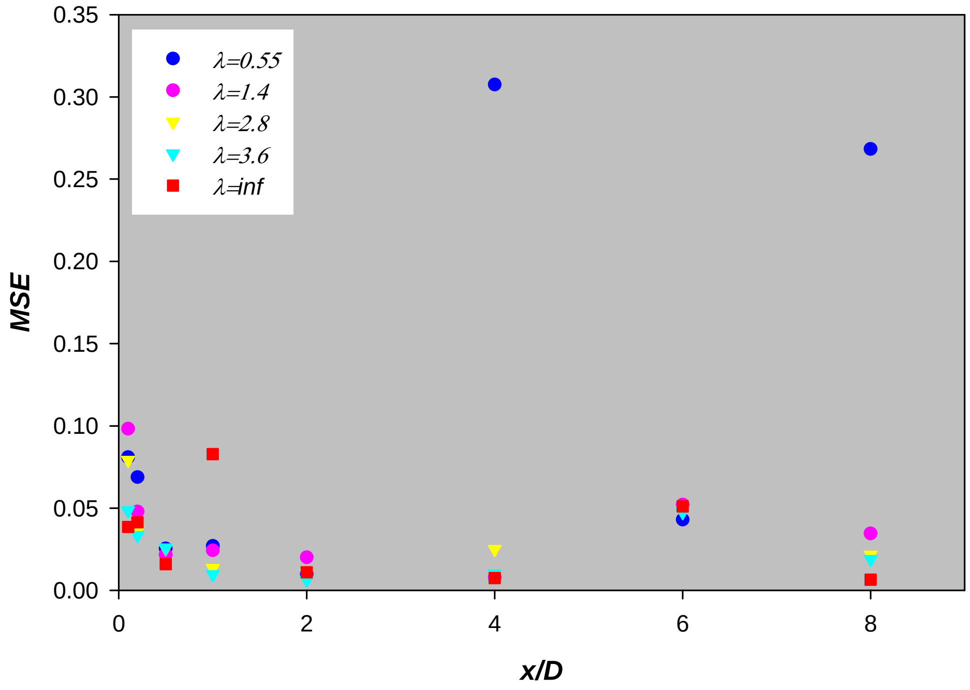

Figure 7.28: Averaged mean square error versus *x/D* for the secondary jet at velocity ratios of *λ*=0.55*,* 1.4*,* 2.8, 3.6 and ∞.

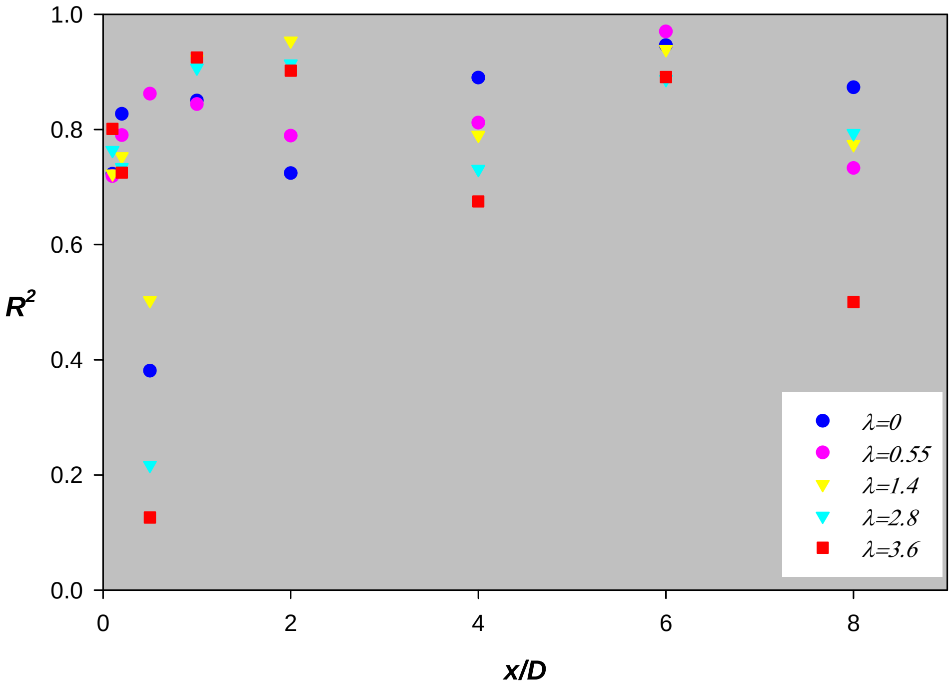

Figure 7.29: Averaged R^2 values versus *x/D* for the primary jet at velocity ratios of *λ*=0, 0.55*,* 1.4*,* 2.8 and 3.6.

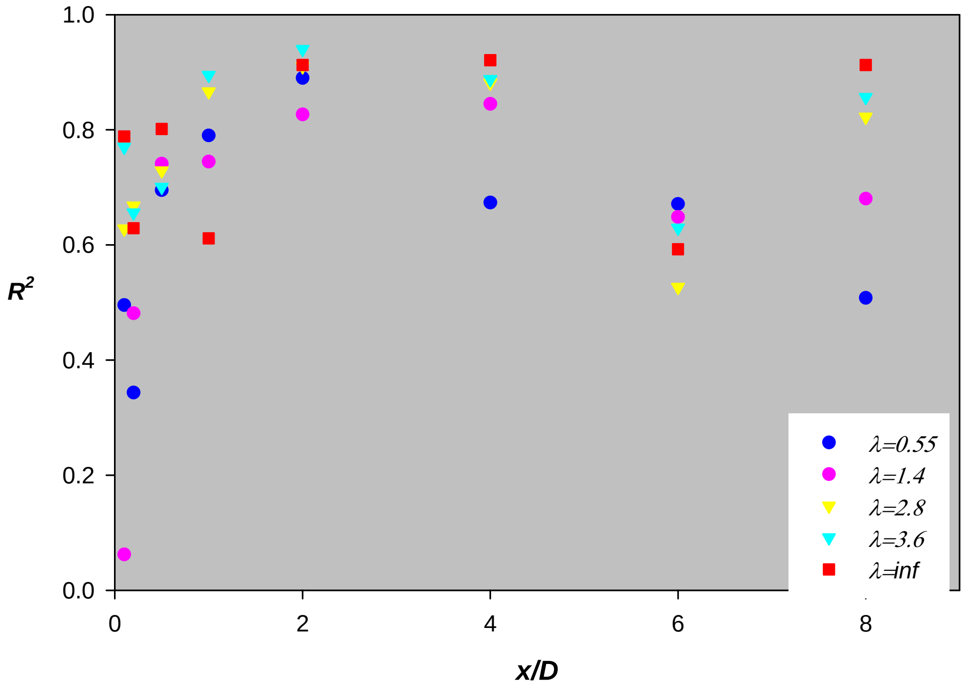

Figure 7.30: Averaged R^2 values versus *x/D* for the secondary jet at velocity ratios of λ=0.55, 1.4, 2.8, 3.6 and ∞.

λ=0		***λ=3.6***	
z/D	***F_o***	***z/D***	***F_o***
-0.25	23.12	0	10.55
0	106.82	0.4	-11.62
0.3	31.52	-0.4	-10.43
0.35	-7.39	-0.3	101.98
-0.35	14.02	0.3	246.42
		-0.35	12.21
		0.35	-8.01
		0.37	-8.11

Table 7.4: Calculated values of F_o for the primary jet x/D =0.1, λ=0 and λ=3.6, with $F_{crit\ (\alpha=0.05)}$ =2.61, $F_{crit\ (\alpha=0.1)}$=2.

	λ=0	***λ=3.6***
z/D	***F_o***	***F_o***
-0.7	-17.86	22.40
-0.6	11.26	105.02
-0.5	83.75	258.39
-0.4	191.88	359.93
-0.3	514.11	615.69
-0.2	566.73	587.16
0	504.58	947.43
0.2	482.65	658.04
0.3	457.09	394.50
0.4	229.35	212.30
0.5	93.25	112.67
0.6	13.91	54.36
0.7		14.57

Table 7.5: Calculated values of F_o for the primary jet, x/D =2, λ=0 and λ=3.6, with $F_{crit\ (\alpha=0.05)}$ =2.45, $F_{crit\ (\alpha=0.1)}$=2.0.

	λ=0	***λ=3.6***
z/D	***F_o***	***F_o***
-2.2	-13.97	5.83
-1.8	10.68	-3.74
-1.5	-1.12	19.09
-1	8.56	81.66
-0.5	-0.02	245.57
0	15.01	138.32
0.5	-6.44	118.21
1	-8.33	5.78
1.5	-8.46	13.21
1.8	-8.46	-16.98
2.2	-12.58	

Table 7.6: Calculated values of F_o for the primary jet x/D =8, λ=0 and λ=3.6, with $F_{crit\ (\alpha=0.05)}$ =2.45, $F_{crit\ (\alpha=0.1)}$=2.0.

	λ=0	***λ=3.6***
y/D	***F_o***	***F_o***
0	131.68	194.08
0.3	90.41	254.22
0.4	10.77	213.95
0.425	-6.08	95.92
0.45	-0.02	-50.29

Table 7.7: Calculated values of F_o for the secondary jet, for x/D =0.1, λ=0 and λ=3.6, with $F_{crit\ (\alpha=0.05)}$ =2.37, $F_{crit\ (\alpha=0.1)}$=1.85.

	λ=0	***λ=3.6***
y/D	***F_o***	***F_o***
0	19.17	194.24
0.3	4.52	204.99
0.4	13.78	183.73
0.5	25.11	175.27
0.6	42.11	135.34
0.7	-60.67	55.27
0.8	-69.60	-27.81

Table 7.8: Calculated values of F_o for the secondary jet, for x/D =2, λ=0 and λ=3.6, with $F_{crit\ (\alpha=0.05)}$ =2.37, $F_{crit\ (\alpha=0.1)}$=1.85.

	λ=0	***λ=3.6***
y/D	***F_o***	***F_o***
0	19.15	186.96
1	25.86	68.84
1.5	75.95	74.51
2	84.44	29.19
2.5	-93.98	-31.43

Table 7.9: Calculated values of F_o for the secondary jet, for x/D =8, λ=0.55 and λ=3.6, with $F_{crit\ (\alpha=0.05)}$ =2.37, $F_{crit\ (\alpha=0.1)}$=1.85.

7.4 Applicability of the Mixing Model to an Overall Combustion Model for Coal Fired Boilers

The current mixing model, developed in cold flow, can be used in a non-isothermal mathematical boiler model provided a number of scaling factors are accounted for. Firstly it is important to conserve geometric ratios. The current model does not precisely preserve the secondary to primary geometric ratios that are present in full-scale Latrobe Valley boilers, but is representative of them. Important considerations are required in the use of data retrieved from isothermal geometrically similar jets whilst predicting the characteristics of jets in full scale furnaces. According to Spalding (1963) complete combustion modelling using all parameters is in most cases, impossible. It is however important to understand what sort of implications occur when applying isothermal data to a non isothermal system, scale up from experimental nozzle to full size nozzles and the possible implications of density and confinement.

Jets can be considered free (unconfined) if the jet diameter is one twentieth or less of the furnace diameter. For unconfined jets, mixing models can be applied without the need for a diameter correction, such as the Thring – Newby parameter. The Thring- Newby parameter (Thring and Newby, 1953) accounts for the expansion and density changes that occur in flames, and for the influence of the confining furnace. It has been widely used when applying cold modelling results to reactive environments (Sunavala *et. al.*, 1959, Chesters, 1959 and Thurlow, 1959). It requires that the scaled diameter, D be replaced by a corrected diameter D', and is dependent on the density of entrained furnace gas, ρ_e, and nozzle exit fluid, ρ_o.

$$D' = D\sqrt{\frac{\rho_o}{\rho_e}} \qquad \textbf{Equation 7.16}$$

Parham *et al.*, (2005) developed a modified form of the Thring-Newby correction diameter which accounts for the effects of confinement for a precessing jet. Equations 7.17-7.20 are the values of K_1, $x_{O,1}$, K_2 and $x_{O,2}$. developed by Parham *et al.*, (2005) as a function of the Duct diameter (D_{duct}), co-flow velocity (U_a) and precessing jet velocity ($U_{e\text{-}PJ}$).

$$K_1 = 0.00774\left(\frac{D_{duct}}{D_{PJ}}\right) + 0.0948$$ **Equation 7.17**

$$\frac{x_{o,1}}{D_{duct}} = -3.386\left(\frac{U_a}{U_{e-PJ}}\right) - 0.3903$$ **Equation 7.18**

$$\frac{1}{K_2} = 0.1138\left(\frac{\dot{m}_a}{\dot{m}_0}\right) + 4.8311$$ **Equation 7.19**

$$\frac{x_{o,2}}{D_{PJ}} = -0.2240\left(\frac{\dot{m}_a}{\dot{m}_0}\right) - 5.75$$ **Equation 7.20**

where $\dot{m}_a$ and $\dot{m}_o$ are the mass-flow rates of confined and precessing jet fluid and D_{PJ} is the diameter of the precessing jet. Although these relationships do not provide any information on the effect of confinement of the rectangular jets, the effect of confinement can be experimentally studied and relationships developed between the confinement geometry and the constants in Equation 7.4.

7.5 Sensitivity Analysis

A sensitivity analysis investigates the effect of a change in input parameter on the output of mathematical, chemical and physical models. Sensitivity methods have been widely used in chemical reaction kinetics (Saltelli *et al.*, 1999; 2000; 2005, Turanyi, 1990, Rabitz *et al.*, 1983). The response of a model's output factor, Y_i, with respect to a given input, X_i, is given as (Saltelli *et al.*, 1999);

$$R_i = \frac{\partial Y_i}{\partial X_i}$$ **Equation 7.21**

To compare different types of input the response R_i is normalised with the average of the output and input, hence the sensitivity is;

$$S_i = \frac{\overline{X_i}}{\overline{Y_i}} \frac{\partial Y_i}{\partial X_i}$$ **Equation 7.22**

This term is more commonly known as the localised sensitivity. An analytical solution for S_i is possible for simple models. However for the one illustrated in Equation 7.4 numerical methods must be applied. Several methods exist, which solve for S_i, such as the method of Miller and Frenklach (Miller and Frenklach, 1983 Frenklach and Miller, 1985 and Frenklach, 1984) the direct method (Buhman, 1969), the Green function method (Dougherty *et al.*, 1979) and the polynomial approximation method (Hwang, 1983). The method applied here however is a finite difference extension of Equation 7.21;

$$R_i = \frac{Y_{i+1} - Y_i}{\Delta X_i}$$ **Equation 7.23**

Sensitivity of the mean mixture fraction (Equation 7.4) to changes in velocity ratio has been studied. The sensitivity analysis was performed on the bulk mixture fraction of the primary jet.

The velocity ratio was varied in increments of 0.5. Figure 7.31 presents the dimensionless sensitivity of the model response as a function of *x/D* for various perturbations in λ. For example, for a change in λ from 1 to 1.5, the sensitivity at any given *x/D*, is:

$$\left(\frac{1.25}{\overline{\xi_{bulk}}}\right) x \left(\frac{\overline{\Delta\xi_{bulk}}}{0.5}\right)$$

where $\overline{\xi_{bulk}}$ is the bulk mixture fraction at that *x/D*, and $\overline{\Delta\xi_{bulk}}$ is the change in bulk mixture fraction due to the change in λ.

In the near nozzle region, the mean mixture fraction is very sensitive to a perturbation in velocity ratio particularly near to *x/D* =1.5 and for a velocity ratio interval of *1-1.5*. This finding concurs with qualitative results from Chapters 4 and 6, which indicated that around *x/D*=2 the primary jet significantly changes in structure with an increase in velocity ratio. In conclusion the model's response to perturbation in velocity ratio is at it's most sensitive in the velocity ratio region $1<\lambda<1.8$ at $1.8<x/D<2$. This suggests that there is a fundamental change in the mixing characteristics of the primary jet when there is a change in velocity ratio in this critical region. The mixing in this area may be momentum controlled hence a specific velocity ratio exists between $1<\lambda<1.8$ at which the higher momentum flux of the secondary jets may start to dominate the flow. The outcome of the sensitivity analysis shows, as the flow is highly sensitive under these conditions, the model accounts for this response adequately.

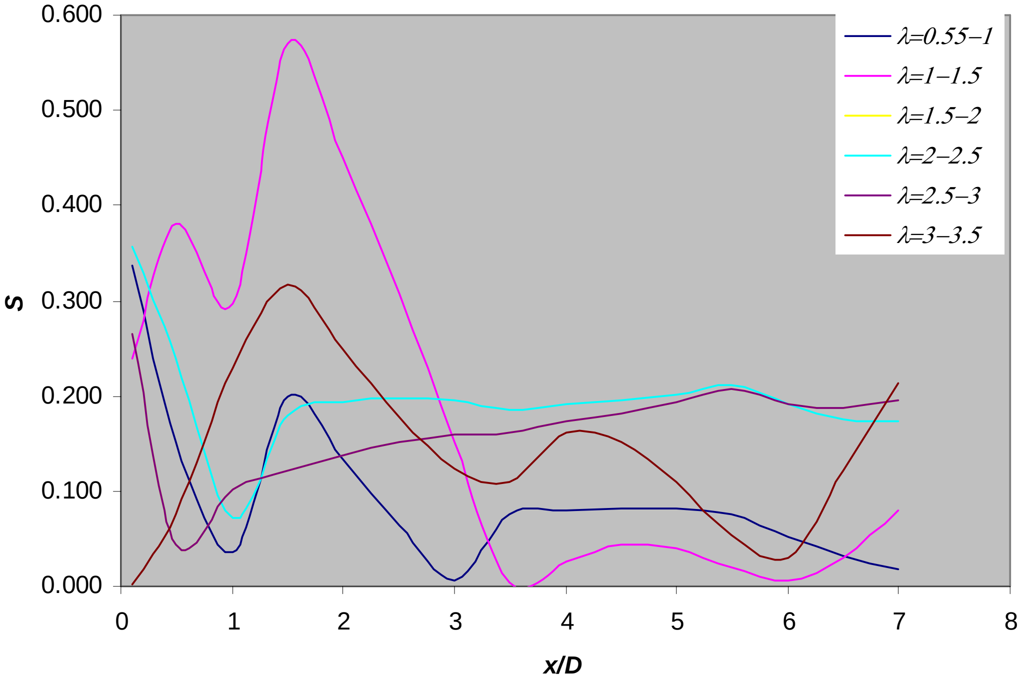

Figure 7.31: Dimensionless sensitivity of the response of bulk mixture fraction change with a change in secondary to primary velocity ratio versus downstream distance *x/D* of the primary jet.

7.6 Conclusion

A model has been developed that interpolates the scalar mixing field of similar primary and secondary jets geometrically similar to those in the Yallourn W1 furnaces. The model interpolates mean scalar quantities for $\lambda=0$ and $\lambda=0.55$ to 3.6 for the primary jet and $\lambda=0.55$ to 3.6 and ∞ for the secondary jet. The model is capable of predicting primary and secondary bulk fluid concentrations within 30 and 40 %, respectively, of the measured values. Higher errors are encountered in the far shear layer due to the regression model's default zero value, where the observed measurements have a weak signal to noise ratio.

The analysis of variance shows that the model is highly representative of the localised and bulk-mean concentrations. Sensitivity analyses reveal that the model is highly sensitive for velocity ratios between $1 < \lambda < 1.8$ and $1.5 < x/D < 2$. The conclusions from Chapter 6 reveal that mixing changes from being controlled by the primary jet to being controlled by the secondary jet in this region. The sensitivity analysis indicates that the regression model is fully capable of handling this change in physical flow characteristics.

Chapter 8

8 Conclusions and Further Work

8.1 Overview

Non-reacting isothermal conditions have been used to study the physical mixing mechanisms of co-flowing rectangular jets. Mixing characteristics such as jet spread, centreline decay and dilution of jet fluid in the cross-stream directions are all affected by velocity ratio. A three dimensional regression model of the primary and secondary jets has been developed. The regression model has been used in conjunction with data from a 1:30 cold flow geometrical model of the Yallourn stage 2 boiler to model reaction rates and heat transfer characteristics. Together they are a part of a boiler heat transfer model that will allow computation of heat release rates, local and total heat transfer to the tube walls together with other boiler characteristics to be assessed in a matter of minutes without resorting to the long computational times of computational fluid dynamics. Together with an understanding of the reactivity of the dewatered lignite and an understanding of the mixing and combustion characteristics, the amount of greenhouse gas formation can be assessed. This is extremely important as it is one of the most talked about topics of the new 21^{st} century.

8.1.1 Mixing Characteristics of Rectangular Jets under different Co-flowing Conditions

8.1.1.1 Qualitative Description of mixing Characteristics

The mixing characteristics of rectangular jets present in brown coal fired boilers were investigated by conducting isothermal experiments in water. A single colour Planar Laser Induced Fluorescence flow visualisation technique was used to investigate the effect of varying secondary to primary velocity ratio. It was applied in planes bisecting the primary and secondary jet axes (longitudinal) and planes perpendicular to the direction of flow (transverse).

A quantitative Planar Laser Induced Fluorescence technique was used to measure the concentration of jet fluid and quantify the effects of varying secondary to primary velocity ratio.

The flow visualisation experiments show that velocity ratio has strong effects on the primary and secondary jet mixing characteristics. For either $\lambda>1$ or $\lambda<1$ it seems that one jet has a "dominating" effect over the nature of the other. The cycle of the vortex ring and braid development is explained in Chapter 4 for the rectangular jet, however is may be possible that the nature of these structures and their frequency are coherently affected by the co-flowing conditions. It has been identified using the coherent structure analysis of Dahm and Dimotakis (1987) and sinuous motion analysis of Yoda *et al*., (1994) that different co-flowing conditions change the nature of the main coherent structures of the primary and secondary jets through planes A, B and C. Many experimentalists (Gutmark and Grinstien, 1999, Grinstein, 1993; 1995; 2001 etc.) have identified the main structure of the rectangular jet as the "vortex ring" which is responsible for momentum transport (Gutmark and Grinstein, 1999). Through the conclusion in Chapter 4, it is reasonable to suggest that, at a certain downstream distance, the primary and secondary rectangular jet flows become momentum controlled. However, further investigations are required to confirm this, for instance, manipulation of the momentum ratio independently to the velocity ratio.

8.1.1.2 Quantitative Description of the Control of Mixing Characteristics

According to Gutmark and Grinstien, (1999), Grinstein, (1993; 1995; 2001) and Hart *et al*., (2004) the vortex ring in rectangular jets with AR <5 does not form until x/D ~ 1-1.5. The quantitative transverse images showed that, at axial stations very close to the nozzle, the shape of the primary jet changes for $\lambda>1$ and the secondary jet for $\lambda<1$. It would seem reasonable to suggest that the pairs of "braids" or vortices are responsible for the witnessed jet deformation. The different co-flowing conditions inherently alter the velocity gradients and hence the vorticity. A change in local vorticity may imply that a vortex may change in size and strength. In the case of the current rectangular jets it appears that on specific corners of the primary and secondary jets one vortex will dominate over it's adjacent structure thus distorting the whole jet.

Unlike the vortex rings, the corner vortices have a minor role in momentum transport and are more likely to be velocity controlled. This contradicts the suggestions made in Section 8.1.1.1 where the mixing of the primary and secondary jets is momentum controlled. Without any certainty it is very well possible that the mixing in the near region is velocity controlled and further downstream momentum controlled. This concept has been demonstrated for turbulent co-annular jets (Beer and Chigier, 1972). An independent evaluation of the momentum ratio to velocity ratio would confirm whether mixing is velocity controlled, momentum controlled or both and if the latter, where the transition point occurs and whether or not it is influenced by velocity ratio.

8.1.2 Three Dimensional Modelling of Rectangular Jets under Different Co-flowing Conditions

The planar transverse quantitative data of the primary and secondary jets was used with the method of weighted squares to develop a 3-D regression model of the scalar-mixing field. The regression model reproduces scalar quantities for λ=0 and λ=0.55 to 3.6 for the primary jet and λ=0.55 to 3.6 and ∞ for the secondary jet. The model is capable of predicting primary and secondary bulk fluid concentrations within 30 and 40 % of the measured values, respectively. Higher errors are encountered in the far shear layer due to the regression model's default zero value, where the observed measurements have a minor background signal.

An analysis of variance was conducted on the regression model. It demonstrated that the model is highly representative of the localised and bulk-mean concentrations. A sensitivity analysis was also conducted on the primary jet revealing that the regression model is highly sensitive for velocity ratios between $1 < \lambda < 1.8$ and $1.5 < x/D < 2$. Conclusions from Chapter 6 reveal that mixing is highly sensitive to changes in λ in this region. The sensitivity analysis concluded that the regression model is fully capable of handling this change in physical flow characteristics.

8.2 Recommendations for Further Work

8.2.1 Variation of the Momentum Ratio Independently of Velocity Ratio

In order to determine whether the flow of the primary and secondary jets is momentum controlled or velocity controlled or both, it would be opportune to investigate the effect of the variation of momentum ratio on jet mixing independently from velocity ratio. The momentum ratio is a function of velocity ratio, cross sectional area of the primary and secondary jets as well as jet density;

$$\kappa = \frac{\rho_2 A_2}{\rho_1 A_1}\lambda^2$$

Equation 8.1

It would not be possible to alter the secondary to primary jet cross sectional ratio (A_2 / A_1) as geometric similarity would no longer be maintained. However, concentration studies on co-flowing jets using different density ratios has been done in the past by a number of experimentalists such as Forstall and Alpinieri (1950) who studied the concentration of turbulent co-annular jets using helium as the working fluid of the central jet and air in the annular section or Chigier and Beer (1964) who used methane as central jet fluid. By using the same velocity ratios as displayed in Table 3.3 the momentum ratio can then be changed by altering the density ratio, so that flow visualisation and concentration studies may be conducted and then compared to the iso-density results in Chapters 4 and 6.

8.2.2 Velocity Measurements

The present work offers insight into the mixing between rectangular jets like those present in brown coal fired boilers. A more in depth analysis of the large and small scale flow structures could be obtained from velocity data. One useful technique is Particle Imaging Velocimetry (PIV) a planar technique that is able to diagnose the instantaneous and time averaged 2-D components of turbulent velocity. Although PIV is a very powerful technique it is only two-dimensional and therefore incapable of providing out of plane Data, which can be used for quantification of vorticity. Determination of vorticity is required to isolate individual dominant flow structures and observe the interaction between the flow structures. Computational fluid dynamics can be used to simulate three dimensional data. Large eddy simulation has been used for the rectangular jets by Hart (2001). He simulated one full secondary jet and an adjacent bisected primary jet. The use of a similar technique to the whole tri-jet formation would yield invaluable information. In conclusion, further work should consider the use of both 2-D velocity measurements as a means of validity of a CFD model and a CFD model of the tri-jet formation.

8.2.3 Quantification of Fluctuating Scalar Statistics

Fluctuating statistics in turbulent jet flows are important in identifying the movement of turbulent structures. For the current rectangular jets, knowledge of the random mean square concentration or the time-dependent fluctuating concentration would be a valuable addition to the mean concentration mixing model, allowing for greater accuracy when performing combustion computations.

The current Planar Laser Induced Fluorescence technique employed a continuous wave laser together with a non-triggered response and no-gain controlled camera. This technique did not have the temporal resolution to quantitatively resolve the flow field for statistical quantification of fluctuating concentration. In order to achieve higher temporal resolution a pulsed laser with a triggered amplified photomultiplier imaging system is required.

8.2.4 Variations in Geometry

In Appendix D the qualitative Planar Laser induced Fluorescence procedure was extended to investigating rectangular jets with base plates fitted at 90 degrees to the direction of flow and with a 60 degree inclination.

The 90 degree base plate only caused distinct differences in the primary jet at velocity ratios of λ=1.4 at x/D>6. The most plausible physical mechanism behind this is that the higher secondary velocities cause the jets to increase their appetite for entrainment. The fluid entrained from the surroundings enters the secondary jets further downstream and at a different angle, causing the jets to move away from their geometric axes, in turn causing the primary jet to expand.

The inclination of the base plate only affects the primary and secondary jets through planes C and B respectively. The change in entrainment patterns causes the jets to move from their geometric axes towards the side of the plate with the acute angle to the burners.

Changes in geometry can be investigated to extend the current investigation. For example, nozzle aspect ratio could be varied since not all the rectangular jets in brown coal fired boilers have the same aspect ratios as the main burners of the Yallourn W' boilers. Other geometrical characteristics that could also be quantified include the addition of recess around the jets, the angle with the boiler wall, and change in upstream geometry. The influence of upstream geometry has barely been mentioned in any of the studies on rectangular jets for lignite boilers. Velocity measurements of some of these variations in geometry have been taken by hot wire anemometry (Perry and Pleaseance, 1983a; 1983b), and modelled by large eddy simulation (Hart *et al*., 2004 and Ahmed *et al*., 2003). However, no one to date has quantified the passive scalar statistics of such jets.

9 Publications Arising From This Thesis

Scarsella A. A. (2003). Physical modelling of the Mixing and Combustion Characteristics of Adjacent rectangular jets. Proceedings, 11th annual conference, Cooperative Research Centre for Clean Power From Lignite, Melbourne, Swinburne University of Technology

Scarsella, A. A. (2003). Research Proposal for the Degree of Doctor of Philosophy, Physical Modelling of Mixing Characteristics of Burner Nozzles used in Tangentially Fired Pulversied Coal Boilers. Adelaide, South Australia, University of Adelaide**:** 35.

Scarsella, A. A., Mullinger P.J, Smith N.L. (2003). Physical Modelling of the Mixing Characteristics of Nozzles used in Tangentially Fired Pulverised Coal Boilers. Australian Symposium on Combustion, Monash University, Melbourne, Australia.

Scarsella, A. A., Mullinger, P.J., Nathan, G.J. (2004). Physical Modelling of the Mixing and Combustion Characteristics of Adjacent Rectangular Jets. 12th annual conference of the Cooperative Research Centre for Clean Power from Lignite, Monash University, Victoria

Scarsella, A. A., Mullinger P.J, Nathan, G.J. (2005). Flow visualisation of the passive scalar of rectangular jets present in pulverised brown coal fired boilers. Proceedings of the 13th annual conference, CRC for Clean Power from Lignite, Monash University.

Mullinger, P. J., Smith, N. L., **Scarsella, A. A.**, Ballantyne T. (2006). Development of a Combustion Zone Model to Predict Heat Transfer and Tube-wall Temperatures. Proceedings, 14th annual conference, Cooperative Research Centre for Clean Power From Lignite, Monash University, Melbourne

10 References

(1987). The Australian Concise Oxford Dictionary of Current English.

Abramovich, G. N. (1963). The Theory of Turbulent Jets. Cambridge, Massachusetts, MIT Press.

Abramovich, G. N. (1982). "On The Deformation of The Rectangular Turbulent Jet Cross Section." International Journal of Heat and Mass Transfer **25**(12): 1885-1894.

Abramovich, G. N. (1983). "Deformation of the Transverse Section of a Turbulent Rectangular Jet." Fluid Dynamics **18**(1): 40-48.

Ahmed, S., Hart, J., Naser (2003). The Effect of Jet Velocity Ratio on Aerodynamics of Rectangular Slot Burners in Tangentially-Fired Furnaces. Third international Conference on CFD in the Minerals and Process Industries, CSIRO, Melbourne Australia.

Albertson, M. L. (1950). "Diffusion of Submerged Jets." American Society of Civil Engineers Transactions **115**: 639-697.

Alpinieri, L. J. (1964). "Turbulent mixing of coaxial jets." AIAA Journal **2**(9): 1560-1567.

Antonia, R. A., Bilger R.W. (1976). "The Heated Round Jet in a co-flowing stream." AIAA Journal **14**(11): 1541-1547.

Antonia, R. A., Satyaprakash, B.R. and Hussain, A.K.M.F. (1980). "Measurements of Dissipation rate and some other Characteristics of Turbulent Plane and Circular Jets." Physics of Fluids **23**(4): 695-700.

Arcoumanis, C., McGuirk, J.J., Palma, J.M.L.M. (1990). "On the use of fluorescent dyes for concentration measurements in water flows." Experiments in Fluids **10**: 177-180.

Ashman, P. J., Mullinger, P. J. (2005). "Research issues in Combustion and Gasification of Lignite." Fuel **84**: 1195-1205.

Balachandar, S., Mittal, R., Najjar, F.M. (1997). "Properties of the Mean Recirculation Region in the Wakes of Two Dimensional Bluff Bodies." Journal of Fluid Mechanics **351**: 167-199.

Banks, P. J., Burton, D.R. (1985). Properties of Brown Coal in Press De-watering. Proceedings of The International Conference on Coal Science, Sydney.

Banks, P. J., Burton, D. R. (1989). "Press De-watering of Brown Coal: Part 1 - Exploratory Studies." Drying Technology **7**(3): 443-375.

Becker, H. A. (1977). Mixing, Concentration fluctuations and Marker Nephelometry. Studies in Convection. B. E. Launder, Academic Press. **2:** 45-139.

Becker, H. A., Hottel, H.C. and Williams, G.C. (1967). "The Nozzle-Fluid Concentration Field of the Round Turbulent Free Jet." Journal of Fluid Mechanics **30**: 285-303.

Becker, H. A., Yamazaki, S. (1978). "Entrainment, momentum flux and temperature in vertical free turbulent diffusion flames." Combustion and Flame **33**: 123-149.

Becker, W., Kennedy, P. (1992). "A Lesson Learned in Least Squares and R Squared." The American Statistician **46**(4): 282-283.

Beer, J. M. (1966). "The Significance of Modelling." Journal of The Institute of Fuel: 466-473.

Beer, J. M., Chigier, N.A. (1972). Combustion Aerodynamics, Applied Science Publishers.

Birch, A. D., Brown, D.R., Dodson, M.G., Thomas, J.R. (1978). "The Turbulent Concentration Field of a Methane Jet." Journal of Fluid Mechanics **88**: 431-449.

Bird, B. R., Stewart, W.E, Lightfoot, E.N. (1960). Transport Phenomena, Second Edition, John Wiley and Sons.

Boguslawski, L., Popiel, Cz. O. (1979). "Flow Structure of the Free Round Turbulent jet in the Initial Region." Journal of Fluid Mechanics **90**: 531-539.

Bray, T. P., Garry.K.P (2000). "On the Velocity Profile of Inclined Jets in a Boundary Layer for Vorticity Production." Proceedings of the Institution of Mechanical Engineers **214**: 55-64.

Broadwell, J. E., Mungal, M.G. (1991). "Large Scale Structures and Molecular Mixing." Physics of Fluids **3**(5): 1193-1206.

Brungart, T. A., Petrie, H.L., Harbison, W.L., Merkle, C.L. (1991). "A Fluorescence Technique for Measurement of Slot Injected Fluid Concentration Profiles in a Turbulent Boundary Layer." Experiments in Fluids **11**: 9-16.

Buhman, F. A., Melamed, V.G., Polak, L.S., Haut, Yu. L., Chervochkin, E.N. (1969). Vychisletl'noi Matematiki v Himicheskoi i Fizicheskoi Kinetike**:** 12.

Bunderson, N. E., Smith, B.L. (2005). "Passive Mixing Control of Plane Parallel Jets." Experiments in Fluids **39**: 66-74.

Buresti, G., Petagna, P., Talamelli A. (1998). "Experimental Investigation on the Turbulent Near-Field of Co-axial Jets." Experimental, Thermal and Fluid Science **17**: 18-36.

Casella, G. (1983). "Leverage and Regression Through the Origin." The American Statistician **37**(2): 147-152.

Champagne, F. H., Wygnanski, I.J. (1971). "An Experimental Investigation of Co-axial Turbulent Jets." International Journal of Heat and Mass Transfer **14**: 1445-1464.

Chen, R. H., Driscoll, J.F. (1990). Nitric Oxide Levels of Jet Diffusion Flames: Effects of Co-axial Air and Other Mixing Parameters. International Symposium on Combustion.

Chesters, J. H. (1959). "Aerodynamic approach to furnace design." American Society of Mechanical Engineers -- Transactions -- Journal of Engineering for Power **91**(4): 361-369.

Chigier, N. A., Beer, J.M. (1964). "The Flow Region near the Nozzle in Double Concentric Jets." Transaction of the American Society of Mechanical Engineers, Journal of Basic Engineering **4**: 797-804.

Chu, P. C. K., Lee, J. H., Chu, V. H. (1986). "Spreading of a Round Turbulent Jet in a Co-flow." Journal of Hydraulic Engineering **125**(2): 193-204.

Chua, L. P., Antonia, R.A. (1986). "The turbulent Interaction Region of a Circular Jet." International Communications in Heat and Mass Transfer **13**: 545-558.

Churchill, S. W., Usagi, R. (1974). "A Standardized Procedure for the Production of Correlations in the form of a Common Empirical Equation." Industrial Engineering Chemistry Fundamentals **13**(1): 39-44.

Clayton, S., Hoadley, A., Tiu, C., Huynh, S., McIntosh, M. (2003). Development of a Laboratory Scale Continuous MTE process. Tenth Annual Conference, Cooperative Research Centre for Clean Power From Lignite, Swinburne University of Technology.

Corrisin, S., Kistler, A.L. (1955). NACA Rept # 1244.

Corrsin, S., Uberoi, M. S. (1949). Further Experiments and on Flow and Heat Trasnfer in a Heated Turbulent Air Jet. NACA Rept # 1865.

Crimaldi, J. P. (1997). "The Effect of Photobleaching and Velocity Fluctuations on Single-Point LIF Measurements." Experiments in Fluids **1997**: 325-330.

Dahm, W. J. A., Dimotakis, P.E. (1987). "Measurement of Entrainment and Mixing in Round Turbulent Jets." AIAA Journal **25**(9): 1216-1223.

Dahm, W. J. A., Dimotakis, P.E. (1990). "Mixing at large Schmidt number in the self similar far field of turbulent jets." Journal of Fluid Mechanics **217**: 229-330.

Dahm, W. J. A., Frieler, C. E., Tryggvason G. (1992). "Vortex Structure and Dynamics in the Near Field of a Co-axial Jet." Journal of Fluid Mechanics **241**: 371-402.

Deo, R. (2005). Experimental Investigations of the Influence of Reynolds Number and Boundary Conditions on a Plane Air Jet. School of Mechanical Engineering, University of Adelaide.

Dimotakis, P. E., Broadwell, J. E., Howard, R. D. (1978). "Chemically Reacting Turbulent Jets." AIAA Paper 83-0474.

Dougherty, E. P., Rabitz, H. (1979). International Journal of Chemical Kinetics **11**: 1237.

Dowling, D., Dimotakis, P.E. (1990). "Similarity of the Concentration field of Gas-Phase Turbulent Jets." Journal of fluid Mechanics **218**: 109-141.

Durao, D., Whitelaw, J.H. (1973). "Turbulent Mixing in the Developing Region of Co-axial Jets." Journal of Fluids Engineering **95**: 467.

Durie, R. A. (1991). The Science of Victorian Brown Coal, Butterworth Heinemann.

Dyer, T. M. (1979). "Rayleigh Scattering measurement of time-resolved concentration in a Turbulent Propane Jet." AIAA Journal **17**(8): 912-914.

Eaton, J. K., Fessler, J.R. (1994). "Preferential Concentration of Particles by Turbulence." International Journal of Multiphase Flow **20**: 169-204.

Ebrahimi, I., Kleine, R. (1977). "Konzentrationsfelder in Isothermen Luft-Freistrahlen." Forsch. Ing.(43): 25-30.

Eckbreth, A. C. (1988). Laser Diagnostics for Combustion Temperature and Species, Abacus Press.

Elbanna, H., Gahin. S., Rasheed, M.I.I. (1983). "Investigation of Two Plane Parallel Jets." AIAA Journal **21**(7): 986-991.

Elrod, H. G. (1954). "Computation charts and Theory for Rectangular and Circular Jets." The American Society of Heating and Ventilating Engineers(march): 149-155.

Ferdman, E., Otugen, M.V., Kim, S. (2000). "Effect of Initial Velocity Profile on the Development of Round Jets." Journal of Propulsion and Power **16**(4): 676-686.

Forstall, W., Shapiro, A.H., (1950). "Momentum and Mass Transfer in Coaxial Gas Jets." Journal of Applied Mechanics **December 1950**: 399-408.

Frenklach, M. (1984). Combustion and Flame **58**: 69.

Frenklach, M., Miller, D.L. (1985). American Institute of Chemical Engineering **31**: 498.

Grandmaison, E. W., Becker, H.A., Zettler, N.L. (1996). "Scalar Mixing in turbulent Concentric Round Jets." The Canadian Journal of Chemical Engineering **74**(August): 433-447.

Grandmaison, E. W., Pollard, A. (1991). "Scalar Mixing in a Free, Turbulent Rectangular Jet." International Journal of Heat and Mass Transfer **34**(10): 2653-2662.

Grandmaison, E. W., Rathgeber, D.E. and Becker, H.A. (1982). "Some Characteristics of Concentration Fluctuations in Free Turbulent Jets." The Canadian Journal of Chemical Engineering **60**(April, 1982): 212-219.

Grandmaison, E. W., Zettler, N.L. (1989). "Turbulent Mixing in Co-flowing Plane Jets." The Canadian Journal of Chemical Engineering **67**(12): 889-897.

Grinstein, F. F. (1993). Vorticity Dynamics in Spatially Developing Square Jets, AIAA Paper 93-3441. Shear Flow Conference.

Grinstein, F. F. (1995). "Self-Induced Vortex Ring Dynamics in Subsonic Rectangular Jets." Physics of Fluids **7**: 2519.

Grinstein, F. F. (2001). "Vortex dynamics and entrainment in rectangular free jets." Journal of Fluid Mechanics **437**: 69-101.

Guo, J., Tiu C., Hodges, S. (1999). "Hydrothermal Mechanical Upgrading of Brown Coal." Coal Preparation **21**: 35-52.

Gutmark, E., Grinstein, F.F. (1999). "Flow Control with non-circular Jets." Annual Review in Fluid Mechanics **31**: 239-272.

Han, D., Mungal, M.G. (2001). "Direct measurement of Entrainment in reacting/Non-reacting Turbulent Jets." Combustion and Flame **124**: 370-386.

Hanson, R. K. (1986). Combustion Diagnostics: Planar Imaging Techniques. International Symposium on Combustion, Munich, Germany.

Hart, J., Naser. J., Witt, P. (2004). Coherent Structure Dynamics from Irregular Shaped Nozzles. 15th Australasian Fluid Mechanics Conference, University of Sydney.

Hart, J. T. (2001). A Numerical Investigation of Isothermal Burner Jet Aerodynamics. School of Engineering and Science. Melbourne, Victoria, Swinburne University of Technology.

Hill, B. J. (1972). "Measurement of local Entrainment rate in the initial region of axisymmetric turbulent air jets." Journal of fluid Mechanics **51**(4): 773-779.

Holland, F. A., Bragg, R. (1995). Fluid Flow For Chemical Engineers, Second Edition, Edward Arnold.

Huang, R. F., Lin C.L. (2000). "Velocity Field of a Bluff Body Wake." Journal of Wind Engineering **85**: 31-45.

Husain, H. S., Bridges, J. E., Hussain, F. (1988). Turbulence Management in Free Shear Flows by Control of Coherent Structures. International Symposia on Transport Phenomena, Hemisphere Publishing Corporation.

Hwang, J. T. (1983). International Journal of Chemical Kinetics **15**: 959.

Jackson, P. (2003). Review of Research Progress 2002/2003. Tenth Annual Conference, Cooperative Research Centre for Clean Power From Lignite, Swinburne University of Technology.

Jenkins, B. G. (1998). Modelling it's Plastic, Mathematic, stochastic, Elastic and Fantastic. Thermal Energy Engineering and The Environment, Proceedings of the Adelaide International Workshop, University of Adelaide.

Jenkins, B. G., Moles, F.D. (1981). "Modelling Heat Transfer from a Large Enclosed Flame in a Rotary Kiln." Transaction of the Institute of Chemical Engineers **59**: 17-25.

Jenkins, B. G., Moles, F.D. (1988). Design of Burners for Kiln Applications Using Modelling Techniques. Fifth International Rotary Kiln Conference, London.

Juniper, J. (1973). Flame Measurements in a Brown Coal Fired Furnace. European Symposium on Combustion, University of Sheffield, England.

Karasso, P. S. (1994). Experiments on Mixing and Reaction in Plane and Curved Shear Layers. Department of Mechanical Engineering, Stanford University.

Karasso, P. S., Mungal, M.G. (1997a). "PLIF Measurements in aqueous flows Using the Nd:Yag Laser." Experiments in Fluids **23**: 382-387.

Karasso, P. S., Mungal, M.G. (1997b). "PLIF Measurements in Aqueous Flows Using the Nd:Yag Laser." Experiments in Fluids **23**(382-387).

Ko, N. W. M., Kwan, S.H. (1976). "The Initial Region of Subsonic Co-axial Jets." Journal of Fluid Mechanics **73**: 305-322.

Kolomogrov, A. N. (1942). "Equations of Turbulent motion of a Incompressible Fluid." Physics **6**(1): 56-58.

Koochesfahani, M. M., Dimotakis, P. E. (1985). "Laser Induced Fluorescence of Mixed Fluid Concentration in a Liquid Plane Shear Layer." AIAA Journal **23**(11): 1700-1707.

Kristmanson, D., Danckwerts, P.V. (1964). "Studies in Turbulent Mixing- I: Dilution of a Jet." Chemical Engineering Science **16**: 267-277.

Krothpalli, A., Baganoff, D., Karamcheti, K. (1980). "Development and Structure of a Rectangular Jet in a Multiple Jet Configuration." AIAA Journal **18**(8): 945-950.

Krothpalli, A., Baganoff, D., Karamcheti, K. (1981). "On the Mixing of a Rectangular Jet." Journal of Fluid Mechanics **107**: 201-220.

Kvalseth, T. O. (1985). "Cautionary Note about R^2." The American Statistician **39**(4): 279-285.

Lai, J. C. S., Lu, D. (1996). "Effect of Wall Inclination on the Mean Flow and Turbulence Characteristics in a Two-Dimensional Wall Jet." International Journal of Heat and Fluid Flow **17**(4): 377-385.

Launder, B. E., Rodi, W. (1983). "The Turbulent Wall Jet-Measurements and Modeling." Annual Review in Fluid Mechanics **15**: 429-459.

Law, A. W. K., Wang ,H. (2000). "Measurement of Mixing Processes with Combined Digital Particle Imaging Velocimetry." Experimental, Thermal and Fluid Science **22**: 213-229.

Li, X., Tankin, R.S. (1987). "A Study of Cold and Combusting Flow Around Bluff-Body Combustors." Combustion Science and Technology **52**: 173-206.

Lin, K.-C., Faeth, G.M. (1999). "Shapes of Non-buoyant Round Luminous Laminar-Jet Diffusion Flames in Co-flowing Air." AIAA Journal **37**(6).

Lin, Y. F., Sheu, M.J. (1991). "Interaction of Parallel Turbulent Plane Jets." AIAA Journal **29**(9): 1372-1373.

Lubbers, C. L., Brethouwer, G., Boersma, B.J. (2001). "Simulation of the Mixing of a Passive Scalar in a Round Turbulent Jet." Fluid Dynamics Research **28**: 189-208.

Mann, H. B., Whitney, D.R. (1947). "On a test of Whether one of two Random Variables is Stochioastically Larger than the other." Annals of Mathematical Statistics **18**: 50-60.

Marsters, G. F. (1977). "Interaction of Two, Plane Parallel Jets." AIAA Journal **15**(12): 1756-1762.

Marsters, G. F., Fotheringham, J. (1980). "The Influence of Aspect Ratio on Incompressible, Turbulent Rectangular Slots." Aeronautical Quarterly **31**: 285-305.

Mathworks (2004). Matlab.

Mi, J., Deo, R., Nathan, G.J. (2005). "Characterization of Turbulent Jets from High Aspect Ratio Rectangular Nozzles." Physics of Fluids **17**: 068102.

Mi, J., Nobes, D. S., Nathan, G.J. (2001a). "Influence of Jet exit Conditions on the Passive Scalar field of an Axisymmetric free Jet." Journal of Fluid Mechanics **432**: 91-125.

Mi, J., Nobes, D. S., Nathan, G. J. (2001b). "Influence of Exit Conditions on the Passive Scalar Field of an Axisymmetric Free Jet." Journal of Fluid Mechanics **432**: 91-125.

Mi, J. N., G .J. (2003). "The influence of Probe Resolution on the Measurement of a Passive Scalar and It's Derivatives." Experiments in Fluids **34**: 687-696.

Mi, J. N., G. J., Nobes, D.S. (2001b). "Mixing Characteristics of Axisymmetric Free Jets From a Contoured Nozzle, an Orifice Plate and a Pipe." Transactions of the ASME, Journal of Fluids Engineering **123**: 878-883.

Mi, J. N., G. J., Wong, C. Y. (2006). "The Influence of Inlet Flow Condition on the Frequency of Self-Excited Jet Precession." Journal of Fluids and Structures **22**: 129-133.

Miller, D., Comings, E. W. (1960). "Force-Momentum Fields in Dual Jet Flow." Journal of Fluid Mechanics **7**(2): 237-256.

Miller, D., Frenklach, M. (1983). International Journal of Chemical Kinetics **15**: 677.

Miller, R. S., Madina, C. K., Givi, P. (1995). "Numerical Simulation of Non-Circular Jets." Computers and Fluids **24**: 1-25.

Moles, F. D., Watson, D., Lain, P.B. (1972). The Aerodynamics of the Rotary Cement Kiln. Fourth Symposium on Flames and Industry, London, Imperial College.

Montgomery, D. C., Runner, G.C. (1999). Applied Statistics and Probability for Engineers, Second Ed., Wiley.

Mostafa, A. A., Khalifa, M. M., Shabana, E. A. (2000). "Experimental and Numerical Investigation of Multiple Rectangular Jets." Experimental, Thermal and Fluid Science **21**: 171-178.

Moustafa, G. H., Ranthakrishman, E. (1993). "Studies on the Flow Field of Multi-jet with Square Configuration." AIAA Journal **31**(7): 1189-1190.

Mullinger, P. J., Smith, N., England, G., Goodhand, D., Nathan, G. (2002). Similarities in the Mixing Characteristics of Multiple Rectangular Jets and Cylindrical Jets. Asian pacific confederation of chemical engineering conference, 2002, Christchurch , New Zealand.

Mungal, M. G., Hollingsworth, D.K. (1989). "Organized Motion in a very High Reynolds number Jet." Physics of Fluids **1**(10): 1615-1624.

Nakamura, S. Y., Miyata, M. (1982). "A Study on the fluctuating Field in a Turbulent Jet." Memoirs of the Faculty of Engineering, Nagoya University **34**(1): 113-124.

Namazian, M., Kelly, J. (1992). "Concentration Imaging Measurements in Turbulent Concentric-Jet Flows." AIAA Journal **30**(2): 384-394.

Nathan, G. J., Mullinger, P.J., Bridger, D., Martin, B. (2006). "Investigation of a Combustion Driven Oscillation in a Refinery Flare. Part A: Full Scale Assessment." Experimental, Thermal and Fluid Science **30**: 285-295.

Neter, J., Kutner, M. H., Wasserman, W., Nachtsheim, C.J. (1996). Applied Linear Statistical Models, McGraw-Hill/Irwin; 4th edition.

Newbold, G. J. R., Nobes, D.S., Nathan, G.J., Luxton, R.E., Alwahabi, Z.T., King, K.D. (1996). Visualisation and Mixing in the Precessing Jet Flow. First Australian Conference on Laser Diagnostics in Fluid Mechanics and Combustion, The University of Sydney, Australia.

NG, S., Grandmaison, E. W. (1989). "Mixing Indices in Co-flowing Plane Jets: High Momentum Conditions." The Canadian Journal of Chemical Engineering **67**(12): 898-905.

Nielsen, H. A. (1999). Parametric and Non-Parametric System Modelling. Department of Mathematical Modelling, University of Denmark.

Nobes, D. S. (1997). The generation of large scale strcutures by jet precession. Department of Mechanical Engineering. Adelaide, University of Adelaide.

Papanicolaou, P. N., List, E.J. (1987). "Statistical and spectral properties of tracer concentration in round buoyant jets." International Journal of Heat and Mass Transfer **30**(10): 2059-2071.

Papanicolaou, P. N., List, E. J. (1988). "Investigations of Round Turbulent Buoyant Jets." Journal of Fluid Mechanics **195**: 341-391.

Parham, J. J. (2000). Control and Optimisation of Mixing and Combustion from a Precessing Jet Nozzle. Department of Mechanical Engineering. Adelaide, University of Adelaide**:** 250.

Parham, J. J., Nathan, G. J., Luxton, R. E. (1998). "The Interaction between an Axial Jet and Precessing Jet." The Album of Visualisation, The Visualisation Society of Japan **15**.

Park, R. E. (1978). "The Value of Television Time: Some Problems and Attempted Solutions: Comment." Southern Economic Journal **44**(4): 1006-1015.

Pascheriet, G. O., Oster, D., Long, T. A., Fiedler, H.E. and Wygnaski, I. (1992). "Flow Visualisation and Interactions among Large Coherent Structures in an Axissymmetric jet." Experiments in Fluids **12**: 189-199.

Perry, J. H. (1986). Aerodynamics of Burner Jets Designed for Brown Coal Fired Boilers. Melbourne, Swinburne University of Technology**:** 124.

Perry, J. H., Hausler, T. (1982). Aerodynamics of Burner Jets Designed for Brown Coal Fired Boilers. Melbourne, Victoria, Swinburne University of Technology, State Electricity Commission of Victoria**:** 29.

Perry, J. H., Hausler, T. (1984). Aerodynamics of Burner Jets Designed for Brown Coal Fired Boilers.

Perry, J. H., Pleasance G.E. (1983a). The Influence of Nozzle Geometry on the Development of a Three-jet Isothermal Flow Field. Eighth Australasian Fluid Mechanics Conference, University of Newcastle.

Perry, J. H., Pleasance G. E. (1983b). The Isothermal Aerodynamics of Slot Burners in Tangentially Fired Furnaces. International VGB Conference on Research in power plant Technology, Essen, Germany.

Perry, M. J., Mcintosh, J.H. (1985). Investigation into the Behavior of Burner Jets for Brown-Coal Fired Boilers. Proc. Aust. Inst. Energy Nat. Conf., Melbourne, State Electricity Commission of Victoria, Swinburne University of Technology.

Perry, R. H., Green. D.W (1997). "Perry's Chemical Engineer's Handbook, 7th Ed."

Pitts, W. M. (1991). "Effects of Global Density Ratio on the Centreline Mixing Behavior of Axisymmetric Turbulent Jets." Experiments in Fluids **11**: 125-134.

Pitts, W. M., Takashi, K. (1984). "The Application of Laser Induced Rayleigh Light Scattering to the Study of Turbulent Mixing." Journal of Fluid Mechanics **141**: 391-429.

Quinn, W. R. (1991). "Passive Near-Field Mixing Enhancement in Rectangular Jet Flows." AIAA Journal **29**(4): 515-519.

Quinn, W. R. (1992). "Turbulent Free Jet Flows issuing from Sharp-edged Rectangular Slots: The Influence of Slot Aspect Ratio." Experimental, Thermal and Fluid Science **5**: 203-15.

Quinn, W. R. (1994). "Development of A Large Aspect Ratio Rectangular Turbulent Free Jet." AIAA Journal **32**(3): 547-554.

Rabitz, H., Kramer, M., Dacol, D. (1983). "Sensitivity Analysis in Chemical Kinetics." Annual Review in Physical Chemistry **34**: 419-461.

Rajaratnam, N. (1976). Turbulent Jets, Elsevier Scientific Publishing Company.

Reichardt (1941). "Ueber eine neue theorie der freinen turbulenz." Angwandte Mathematik **21**: 257-264.

Rhine, J. M., Tucker R. J. (1991). Modelling of Gas Fired Furnaces and Boilers, and other Industrial Heating Processes, Mcgraw-Hill.

Ribeiro, M. M., Whitelaw, J.H. (1976). "Turbulent Mixing of Coaxial Jets with Particular Reference to the Near Exit Region." Journal of Fluids Engineering **98**: 284-291.

Richards, C. D. a. P., W.M. (1993). "Global Density Effects on the Self-Preservation Behavior of Turbulent Free Jets." Journal of Fluid Mechanics **254**: 417-435.

Ricka, J. (1987). "Photobleaching Velocimetry." Experiments in Fluids **5**: 381-384.

Ricou, F. P., Spalding, D.B. (1961). "Measurements of Entrainment by Axisymmetrical Turbulent Jets." Journal of Fluid Mechanics **11**: 21-32.

Saltelli, A., Ratto, M., Tarantola, S., Campolongo, F. (2005). "Sensitivity Analysis for Chemical Models." Chemical Reviews **105**: 2811-2827.

Saltelli, A., Tarantola, S., Campolongo, F. (2000). "Sensitivity Analysis as an Ingredient of Modelling." **15**(4): 377-395.

Saltelli, A., Tarantola, S., Chan, K. P.-S. (1999). "A quantitative Model-Independent Method for Global Sensitivity Analysis of Model Output." Technometrics **41**(1): 39-56.

Salter, S., Nguyen, D. (2001). Yallourn W Power Station CRC/CSIRO Ultrasonic Flow Device Trials in 2-PFM-8 UMBD, Test Report No: HPE/2001/022, HRL Technology**:** 1-6.

Sau, A. (1999). "Three Dimensional Simulation of flows through a Rectangular Sudden Expansion." Physics of fluids **11**(10): 3003-3016.

Sautet, J., Salentey, L, Labegorre, B. (2003). "Mixing in the Interaction region of three separated round jets." to be published.

Saylor, J. R. (1995). "Photobleaching of Disodium Flourescien in Water." Experiments in Fluids **18**: 445-447.

Schadow, K. C., Gutmark, E.J., Parr, D.M., Wilson, K.J. (1988). "Selective Control of Flow Coherence in Triangular Jets." Experiments in Fluids **6**: 129-135.

Selby, G. V., Lin, J.C., Howard, F.G. (1992). "Control of Low-Speed Turbulent Separated Flow using Jet Vortex Generators." Experiments in Fluids **12**: 394-400.

Sfeir, A. A. (1976). "The Velocity and Temperature Field of Rectangular Jets." International Journal of Heat and Mass Transfer **19**: 1289-1297.

Sfeir, A. A. (1979). "Investigation of Three-Dimensional Turbulent Rectangular Jets." AIAA Journal **17**(9): 1055-1060.

Sforza, P. M., Stasi, W. (1979). "Heat Three Dimensional Turbulent jets." Journal of Heat Transfer **101**: 353-358.

Sforza, P. M., Steiger, H., Trentacoste, N. (1966). "Studies on Three Dimensional Turbulent Viscous Jets." AIAA Journal **4**(5): 800-806.

Simpson, M., McIntosh, M. (1998). Coal drying study for Yallourn 'W' power station, Cooperative Research Centre for New Technologies for Power Generation from low rank coal.

Simpson. M, M., M. (1998). Coal drying study for Yallourn 'W' power station, Cooperative Research Centre for New Technologies for Power Generation from low rank coal.

Skoog, D. A., West, D.M., Holler, F.J. (1996). Fundamentals of Analytical Chemistry, 7th Ed., Saunders College Publishing.

Smart, J. P., Morgan, D.J. (1994). "Exploring the Effects of Employing Different Scaling Criteria on Swirl Stabilised Pulverised Coal Burner Performance." Combustion Science and Technology **100**: 331-343.

Smart, J. P., Morgan, D.J., Roberts, P.A. (1992). The Effect of Scale on the Performance of Swirl Stabilised Pulverised Coal Burners. Twenty Fourth International Symposium on Combustion, Sydney.

Smart, J. P., Van de Kamp, W. L., Morgan, M. E. (1990). "The Effect of Burner Scale on NOx Emissions from a Swirl Stabilised Pulverised Coal Burner." Fuel **69**: 1350-1355.

Spalding, D. B. (1963). The Art of Partial Modelling. International Symposium on Combustion.

Spall, R. E., Anderson, E. A., Allen, J. (2004). "Momentum Flux in Plane Parallel Jets." Transactions of the ASME, Journal of Fluids Engineering **126**: 665-670.

Sunavala, P. D., Hulse, C., Thring, M.W. (1959). "Mixing and combustion in free and enclosed turbulent jet diffusion flames." Combustion and Flame **1**(2): 179-193.

Tanaka, E. (1970). "The Interference of Two-Dimensional Parallel Jets, 1st Report, Experiments on Dual Jets." Bulletin of the Japanese Society of Mechanical Engineers **13**(56): 272-280.

Tanaka, E. (1974). "The Interference of Two-Dimensional Parallel Jets, 2nd Report, Experiments on the Combined Flow of Dual Jet." Bulletin of the Japanese Society of Mechanical Engineers **17**(109): 920-927.

Tanaka, E., Nakata, S. (1975). "The Interference of Two-Dimensional Parallel Jets, 3rd Report, The Region near the Nozzles in Triple Jets." Bulletin of the Japanese Society of Mechanical Engineers **18**(124): 1134-1141.

Tennekes, H., Lumley, J.L.A (1972). A First Course in Turbulence.

Thring, M. W., Newby, M. P. (1953). Combustion Length of Enclosed Turbulent Jet Flames. International Symposium on Combustion.

Thurlow, G. G. (1959). "Similarity criteria for study of furnace flames by means of cold models." Combustion and Flame **3**(3): 373-388.

Toyoda, K., Hussain, A.K.M.F. (1989). Vortical Structures of Non-Circular Jets. Proceedings of the Asian Congress of Fluid Mechanics, Hong Kong.

Trentacoste, N., Sforza, P. (1967). "Further Experimental Results for Three-Dimensional Free Jets." AIAA Journal **5**(5): 885-891.

Tsuchyia, Y., Horikoshi, C., Sato, T. (1986). "On the Spread of Rectangular jets." Experiments in Fluids **4**: 197-204.

Turanyi, T. (1990). "Sensitivity Analysis of Complex Kinetic Systems Tools and Applications." Journal of Mathematical Chemistry **5**: 203-248.

Turns, S. R. (1996). An introduction to Combustion, Concepts and Applications, Second Edition, Mcgraw Hill.

Walker, D. A. (1987). "A Fluorescence Technique for Measurement of Concentration in Mixing Liquids." Journal of Physics, E: Scientific Instruments **20**: 217-224.

Wall, T. F., Nguyen, H., Subramanian, V., Mai-Viet, T., Howley, P. (1980). "Direct Measurement of the Entrainment by Single and Double concentric Jets in The Regions of Transition and Flow Establishment." Transaction of the Institute of Chemical Engineers **58**(4): 237-241.

Warnatz, J., Maas, U., Dibble, R.W. (1999). Combustion, Physical and Chemical Fundamentals, Modelling and Simulation, Experiments, Pollutant Formation, Springer.

Water, S. (2006). Drinking Water Quality Report 04/05. Adelaide, SA Water.

Wilcoxon, F. (1945). "Individual Comparisons by Ranking Methods." Biometrics **1**: 80-83.

Willems, B., Rumiantseva, I., Weight, H. (2007). Cournot Versus Supply Functions: What Does the Data Tell Us? Electricity Markets Working Papers, WP-EM-21.

Wygnanski, I., Fielder, H. (1969). "Some Measurements in the Self- Preserving Jet." Journal of Fluid Mechanics **38**: 577-612.

Xu, G., Antonia, R.A. (2002). "Effect of Initial Conditions on The Temperature Field of a Turbulent Round Free Jet." International Communications in Heat and Mass Transfer **29**(8): 1057-1068.

Yallourn Power Pty. Ltd. Operating data for the Yallourn 'W' Stage 3 Boiler, obtained between 25-1-01 to 30-4-2004.

Yoda, M., Fielder, H.E. (1996). "The Round Jet in a Uniform Counter-flow: Flow Visualisation and Mean Concentration Measurements." Experiments in Fluids **21**(427-436).

Yoda, M., Hesselink, L., Mungal, M.G. (1994). "Instantaneous Three-dimensional Concentration Measurement in the Self-Similar region of a round high Schmidt number jet." Journal of Fluid Mechanics **279**: 313-350.

Yuu, S., Shimoda, F., Jotaki, T. (1979). "Hot Wire measurement in the Interacting Two-Plane Parallel Jets." AICHE **25**(4): 676-685.

Zhang, X. (2000). "An Inclined Rectangular Jet in a Turbulent Boundary Layer-Vortex Flow." Experiments in Fluids **28**: 344-354.

Zhang, X. (2003). "The evolution of Co-rotating Vortices in a Canonical Boundary Layer with Inclined Jets." Physics of Fluids **15**(12): 3693-3702.

Zhang, X., Collins, X. (1997). "Near field Evolution of a Longitudinal Vortex Generated by an Inclined Jet in a Turbulent Boundary Layer." Transactions of the ASME: Journal of Fluids Engineering **119**: 934-939.

Zijnen, V. D. H. (1958). "Measurements of the Distribution of Heat and Matter in a Plane Turbulent Jet of Air." Applied Scientific Research **7**: 276-291.